1988

The Time Variability Of Spectral Line Asymmetries And Equivalent Widths For The G8 Dwarf Xi Boo A: Evidence For A "starpatch"

Clifford George Toner

NOTICE

The quality of this microform is heavily dependent upon the quality of the original thesis submitted for microfilming. Every effort has been made to ensure the highest quality of reproduction possible.

If pages are missing, contact the university which granted the degree.

Some pages may have indistinct print especially if the original pages were typed with a poor typewriter ribbon or if the university sent us an inferior photocopy.

Previously copyrighted materials (journal articles, published tests, etc.) are not filmed.

Reproduction in full or in part of this microform is governed by the Canadian Copyright Act, R.S.C. 1970, c. C-30

AVIS

La qualité de cette microforme dépend grandement de la qualité de la thèse soumise au microfilmage. Nous avons tout fait pour assurer une qualité supérieure de reproduction.

S'il manque des pages, veuillez communiquer avec l'université qui a conféré le grade

La qualité d'impression de certaines pages peut laisser à désirer, surtout si les pages originales ont été dactylographiées à l'aide d'un ruban usé ou si l'université nous a fait parvenir une photocopie de qualité inférieure

Les documents qui font déjà l'objet d'un droit d'auteur (articles de revue, tests publiés, etc.) ne sont pas microfilmés.

La reproduction, même partielle, de cette microforme est soumise à la Loi canadienne sur le droit d'auteur, SRC 1970, c. C-30

THE TIME VARIABILITY OF SPECTRAL LINE ASYMMETRIES AND EQUIVALENT WIDTHS FOR THE G8 DWARF ξ BOO A: EVIDENCE FOR A "STARPATCH"

by

Clifford G. Toner

Department of Astronomy

Submitted in partial fulfilment
of the requirements for the degree of
Doctor of Philosophy

Faculty of Graduate Studies
The University of Western Ontario
London, Ontario
March 1988

ISBN 0-315-40797-2

ABSTRACT

The chromospherically active G8 dwarf ξ Boo A has been monitored spectroscopically for four observing seasons. A total of 121 high resolution, high signal-to-noise Reticon exposures (representing ~ 300 hours of observing) were obtained at the University of Western Ontario's 1.2 m telescope.

The data were analyzed for variations in the mean line asymmetry, line strength, and line broadening, using a combination of line bisector and Fourier techniques. Systematic variations in all quantities were found, which repeat with a period of 6.43 ±0.01 days. The line broadening variations show no evidence of being magnetic in nature, and there is no evidence of a change in period or phase shift over the four seasons.

A self-consistent model is presented, which is found to be very successful at explaining the observations. The model consists of a single surface feature, carried across the stellar disk by rotation. The characteristics of the feature have been determined through extensive use of numerical experiment. The feature's most distinguishing characteristic is a velocity dispersion which is enhanced by a factor of 1.5 - 2.0 relative to the surrounding photosphere. The feature is found to cover 10% ±5% of the visible disk (2.5% of the total surface), and is ~ 3.7% cooler (~ 200 K), and 15% fainter than the rest of the star. The feature lies at a relatively high latitude (55° ±10°), and has remained essentially

unchanged for at least the four years of this investigation.

The deduced characteristics of the feature cannot be reconciled with the classical sunspot or plage. Therefore, it is believed that this is an entirely new type of stellar feature, quite distinct from both the classical sunspot and plage. The name "Starpatch" is suggested in order to distinguish it from its solar cousins.

A note is added in warning for those who are attempting to use single exposures of solar-type stars to obtain information on their granulation properties. The existence of starpatches makes conclusions based on a small amount of data very uncertain, since one cannot determine from such data whether or not a starpatch is in view.

ACKNOWLEDGEMENTS

Foremost, I wish to acknowledge the efforts of my supervisor Dr. David F. Gray. Although this thesis bears only my name, Dr. Gray has made many direct contributions which deserve recognition. Over the years, his knowledge and expertise have been drawn upon often in our many hours of discussion, and this thesis (and the author) has benefited enormously. Dr. Gray also sacrificed many hours of precious observing time to collect some of the data which has been used in this thesis. For all of this I extend a very heartfelt thankyou.

I next wish to express appreciation to my wife Nelsey. Without her patience and understanding, this thesis would never have seen the light of day.

Thanks are also extended to all of the faculty and staff of Western's Astronomy Department. Everyone has helped to make my stay here pleasant and enjoyable.

Finally, I express my gratitude to S. Saar and W. Lockwood for supplying helpful ancillary data, and to the University of Western Ontario, the Government of Ontario, and the Natural Sciences and Engineering Research Council of Canada for financial support.

TABLE OF CONTENTS

TABLE OF CONTENTS

LIST OF TABLES

LIST OF FIGURES

LIST OF FIGURES

LIST OF FIGURES

LIST OF FIGURES

CHAPTER 1

Introduction

Any discussion of solar-type stars necessarily begins with a review of the solar case itself. The properties of the observed solar line asymmetries have been traced back to small-scale inhomogeneities in the solar photosphere (see for example Dravins et al. 1981; Dravins 1982). High spatial resolution photographs of the solar photosphere reveal a pattern of bright granules, surrounded by dark intergranular lanes. Spectroscopy has shown that the bright granules correlate with local blueshifts, and the darker intergranular lanes correlate with local redshifts (e.g. Richardson and Schwarzchild 1950). The generally accepted interpretation of these observations is that we are seeing hot material rising in the granules, and cool material sinking in the intergranular lanes. Therefore, it is believed that we are observing the upper layer of the solar convection zone.

The properties of the solar granulation lead readily to an an explanation of the observed line asymmetry. Consider first, the contribution to the total flux coming from the rising hot granules alone. These produce a profile which is blue-shifted relative to the local rest frame of the star. If we next consider the contribution from the falling cool material in the intergranular lanes, we see that these produce a profile which is red-shifted. When we add the profiles from the hot and cool regions over the entire surface of the star, and weight them by their relative areal coverage and contrast,

we obtain an asymmetric profile, as shown in Figure 1.1. Because the total flux is dominated by the light from the bright granules, the observed profile has a net blueshift. The exact amount of asymmetry and blueshift depends on the detailed spectral line properties, and on the characteristics of the granulation (i.e., the granular/intergranular contrast, the hot and cool stream velocities, and the relative areal coverage of the granules compared to the intergranular lanes). If one were to measure the same spectral lines as a function of time, or location on the solar disk, any differences in the line asymmetry would imply a modification of the granulation.

Livingston (1982, 1983a, 1983b) has reported both spatial and temporal variations of the observed solar line asymmetry and blueshift. (See also Brant and Schröter 1983; Cavallini et al. 1983; Kaisig and Schröter 1983; and Kaisig et al. 1983.) By measuring the bisector of lines formed in magnetic regions, and comparing this to the bisector of lines formed in non-magnetic regions, Livingston found that the magnetic line bisector almost always has a reduced curvature and smaller displacement relative to the non-magnetic bisector (see Figure 1.2). His interpretation of this is that the convective motions are being inhibited in regions of high magnetic flux. Further observations, this time of the disk integrated line bisectors, show that the mean line asymmetry changes with time, and that the changes may be related to the 11 year solar cycle (Figure 1.3). However, the asymmetry changes are found to be out of phase with the sunspot cycle. Based on the sunspot number, solar maximum occurred in late 1979, but the line asymmetries indicate a diminishing convection well past the

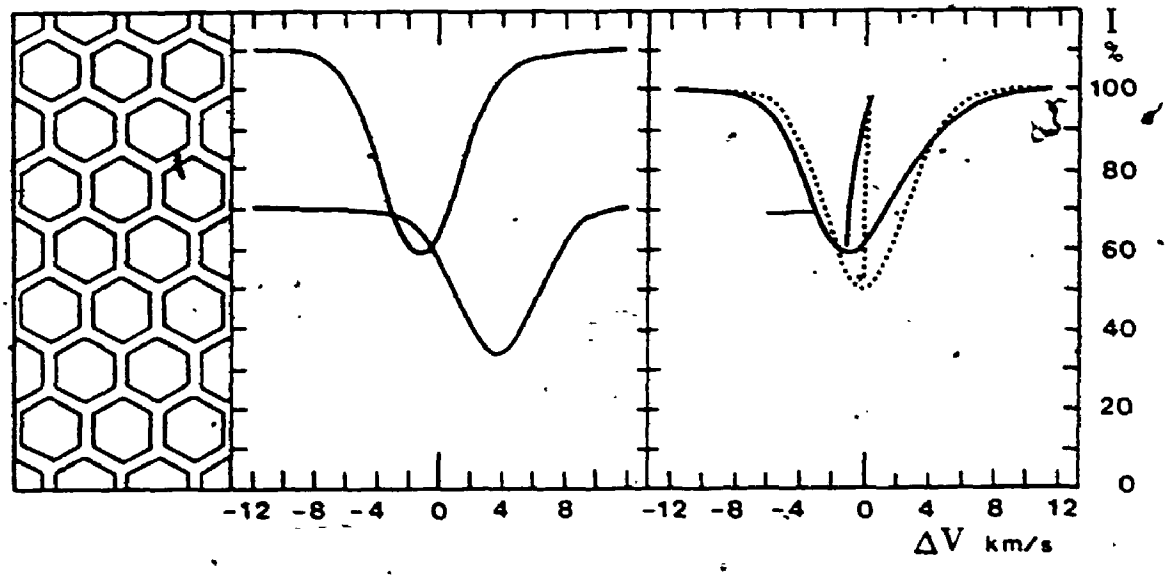

Figure 1.1 Origin of the spectral line asymmetries and wavelength shifts caused by granulation. Left: Idealized white-light image of solar (or stellar) granulation. In this model illustration, 75% of the surface is covered by bright granules with an upflow of 1.2 km s^{-1} that is balanced by a downflow of 3.6 km s^{-1} in the dark intergranular lanes. Center: Spectral line profiles observed under high spatial resolution (resolving individual granules). The top profile is for granular regions and the bottom for intergranular ones. Right: The solid curve gives the resulting profile for observations under low spatial resolution (averaging over many granules). The "C"-shaped line bisector shows the asymmetry and the blueshift of the line. The dashed curve shows an "undisturbed" profile from a static atmosphere or one without organized velocity patterns. From Dravins (1982).

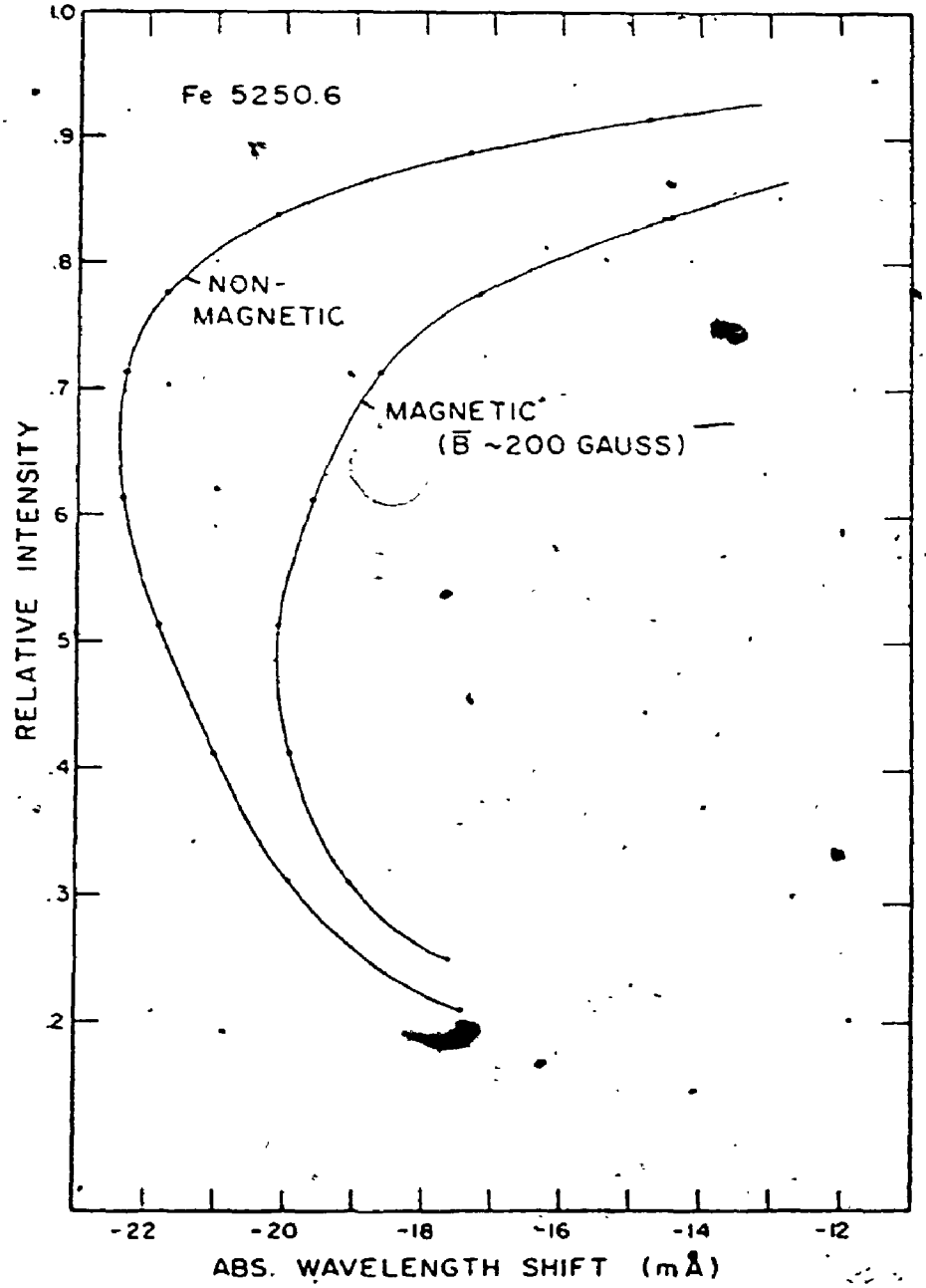

Figure 1.2 Typical line bisectors for adjacent magnetic and non-magnetic regions on the sun, observed at a spatial resolution of 1 x 2 arc-min. (thus averaging over a large number of granules). Note that the magnetic bisector has a reduced line asymmetry and a smaller blueshift relative to the non-magnetic bisector. From Livingston (1983a).

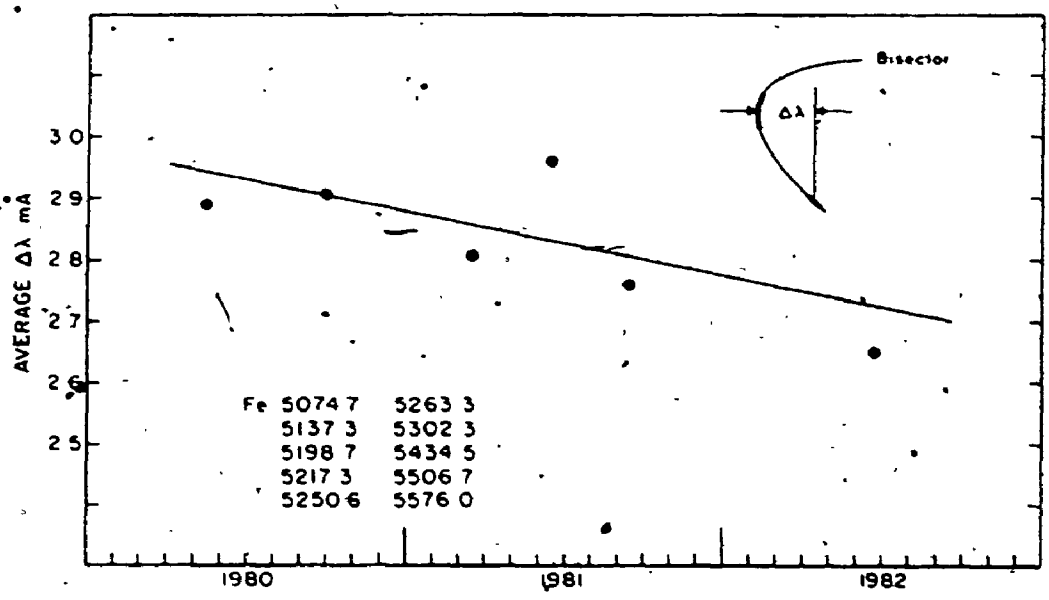

Figure 1.3 .The full disk line bisector curvature, Δλ, showing a decrease with time for the average of 10 similar Fe lines. From Livingston (1983a).

sunspot maximum. Livingston suggests that the magnetic flux which emerged at maximum, and was then confined largely to sunspot umbra, may slowly be getting redistributed over the entire surface. This results in a larger fraction of the surface being covered by magnetic fields, and consequently leads to a reduction in the net granulation signature.

There is other evidence of a coupling between granulation and magnetic fields on the sun. Schröter (1962) finds the diameter of a typical granule to be appreciably smaller near sunspots; and Macris (1979) finds that the granule diameter varies inversely to the magnetic field strength of the spot. Changes in granulation cell size during the solar cycle have been documented by Macris and Rösch (1983) and Macris et al. (1984).

It would appear that, at least for the solar case, changes in the magnetic activity, and/or the redistribution of magnetic fields over the surface, lead to observable changes in the granulation. This suggests the possibility that changes in the line asymmetry of other solar-type stars may occur in response to changes in the star's magnetic characteristics.

Let us now review the some of the evidence in support of the existence and variability of magnetic fields on other cool stars. We know that on the sun regions of magnetic activity correlate well with regions of enhanced emission in the cores of the Ca II H and K resonance lines (e.g. Babcock and Babcock 1955; Frazier 1970; and Skumanich et al. 1975), and that the integrated HK emission varies in phase with the sunspot number (White and Livingston 1981). Thus, the

measurement of the amount of HK emission is often been used as a proxy indicator of magnetic fields. Measurements of the Ca II H and K-line emission indicate that cyclic changes in magnetic activity, similar to the solar cycle, frequently occur in other solar-type stars (Wilson 1978, Vaughan 1980, Vaughan and Preston 1980, Vaughan 1984, Baliunas and Vaughan 1985). Unfortunately, the direct measurement of magnetic fields on late-type stars has proven to be extremely difficult. The traditional method of studying the line displacements in circularly polarized light has yielded essentially null results (e.g. Boesgaard 1974; Vogt 1980; Brown and Landstreet 1981; Borra et al. 1984), most likely because the complex field geometries produce an overall cancellation of the polarization. Techniques utilizing the subtle excess line broadening from the Zeeman effect have been more successful. Magnetic field measurements using this method have been reported for numerous cool dwarfs (Robinson 1980; Robinson et al. 1980; Marcy 1984; Giampapa et al. 1983; Gray 1984a; Gondoin et al. 1985; Saar et al. 1986, 1987; Saar 1987a, 1987b). The typical field strengths are found to be ~ 1-2 kilogauss, with the fields covering anywhere from ~ 10% to ~ 80% of the stellar disk. However, a sufficient time base has yet to be acquired for direct comparison of the measured magnetic parameters with the activity cycles inferred from the H and K-line measurements.

A similar situation exists in the area of line bisector research. Because the accurate measurement of spectral line asymmetries requires both high signal-to-noise ($\sim > 300$) and high spectral resolution ($\lambda/\Delta\lambda \sim 100{,}000$), it has only been with the advent of modern

detectors, such as Reticons and CCDs, that studies of the line asymmetries in solar-type stars have become possible. For this reason, line asymmetries have been measured for only a handful of cool stars (e.g. Gray 1980, 1981, 1982, 1983, 1986a; Gray and Toner 1985, 1986, Dravins 1987a, 1987b), and these investigations have dealt primarily with delineating changes in line bisector shape as a function of position in the HR diagram or with dependence on physical variables such as excitation potential, line strength, or rotation. No investigations of bisector time variability exist, except for Arcturus (Gray 1983), where no detectable changes were found. An interesting result to emerge from these studies is that not all stars of the same spectral type exhibit the same bisector shape (Gray 1983). Could the differences be the result of observing these stars at different phases in their respective activity cycles?

The present study was originally designed to look for the long-term bisector changes expected to occur on stars exhibiting solar-like activity cycles. A handful of bright solar-type stars was selected and monitored spectroscopically using the Coudé spectrograph and Reticon detector attached to the 1.2 m telescope at the University of Western Ontario. About midway through the second observing season, it became apparent that some of the program stars were showing bisector changes above the noise level on a night-to-night basis. Apparently, rotational modulation was making its presence known in the data, thus suggesting the existence of surface inhomogeneities unevenly distributed in longitude around the star. Using the sun as an example, we would expect such features to be magnetic in nature

(like sunspots). The focus of the project was therefore shifted in mid-stream, in order to study these short-term bisector variations, and to see if they could be linked to variations in the magnetic parameters.

The spot phenomenon itself seems to be quite common among late-type stars. Spots have been used to explain the broad-band photometric variations seen for many stars (e.g. Kron 1947, 1950, 1952; Evans 1959, 1971; Torres and Ferraz-Mello 1973; Friedemann and Gurtler 1975; Oskanyan et al. 1977; Eaton and Hall 1979; Vogt 1981a, 1981b; Radick et al. 1982, 1983a,b,; Lockwood et al. 1984; Poe and Eaton 1985; Rodonò et al. 1986 and many others), and the spectroscopic variations (e.g. Vogt 1979, 1981a; Ramsey and Nations 1980; Fekel 1980, 1983; Vogt and Penrod 1983; Gondoin 1986; Vogt et al. 1987 and others). Short-term modulations of the Ca II emission have also been attributed to spots (e.g. Vaughan et al. 1981; Baliunas et al. 1981, 1983). However, little is known about the structure and dynamics of these features. They are believed to be magnetic in nature, because sunspots are magnetic, but no one has yet measured the magnetic field within a starspot. In general they are considerably darker than the surrounding photosphere, being ~ 1000 K cooler on average (a temperature similar to sunspots), but they show other characteristics which are markedly unsunspot-like. For example, the fractional area of the apparent stellar disk covered with spots is often large, ranging between ~ 20% and ~ 40%, compared to the typically < 1% coverage found for spots on the sun. Also, lifetimes of individual starspots are inordinately long compared to their solar counterparts,

often lasting for several hundreds of rotation cycles. One is left wondering if starspots are indeed just extreme examples of the sunspot phenomenon, or whether they are in fact something entirely different. Since line bisectors provide a sensitive diagnostic of the conditions in a star's photosphere, it was hoped that their study would provide clues to answering this question.

Of the program stars monitored, the G8 dwarf ξ Boo A (HR 5544, HD 131156A) shows the largest bisector variations. These were later found to be accompanied by changes in the line strength and line broadening. For these reasons ξ Boo A was selected as the topic of this thesis.

The chromospheric activity of ξ Boo A is known to be above average, and the strong H and K emission has been monitored for many years. The rotational modulation of the H and K emission shows a period of about 6.2 days (Noyes et al. 1984; Baliunas et al. 1985), meaning useful information can be obtained in a single observing season. The surface magnetic field may also be variable (Robinson 1980; Gray 1984a; Marcy 1984; Saar 1987b; Saar et al. 1987).

The secondary component of this binary system is a K4 dwarf, and it is widely separated from ξ Boo A in both physical dimension (a = 31.5 a.u.) and apparent position on the sky (7" during our epoch of observation). Orbital solutions have been given by Strand (1938) and Wielen (1962). The inclination of the orbital plane is 140°, therefore, if the rotation axis of ξ Boo A is aligned with the orbital pole, its angle to our line of sight is 40°.

CHAPTER 2

Equipment and Observations

2.1 The Spectrograph

A schematic of the coudé spectrograph is shown in Figure 2.1. It is operated in a near Lithrow configuration, and is fed by the f/31 beam from the U.W.O. observatory 1.2 m telescope. This beam is brought to a focus at the entrance slot of a Richardson image slicer [1] (Richardson 1968, 1972) located just outside the coudé room. The projected dimensions of the entrance slot are ~ 7" x 4", thus allowing for typical seeing conditions found at the observatory. The spectrograph slit is set to a width of 200 μm. Beyond the image slicer, the beam passes through an order sorting filter [2] and is then collimated by a 6.96 m focal length mirror [3] and dispersed by a 154 x 306 mm grating ruled at 316 lines per mm. The grating is mounted on a motorized table, which permits its rotation via controls in the observer's room. A 559 mm focal length camera [6], which is equipped with a corrector lens [5] to remove spherical aberration, then focuses the beam back along the optical axis. Before the converging beam can come to a focus it is deflected upwards by a small, flat pick-off mirror [7]. Above the pick-off mirror, the beam is finally focused on the face of the Reticon detector [8] (see next section). The pick-off mirror is mounted on a rotatable axle which permits translation of the image perpendicular to the Reticon

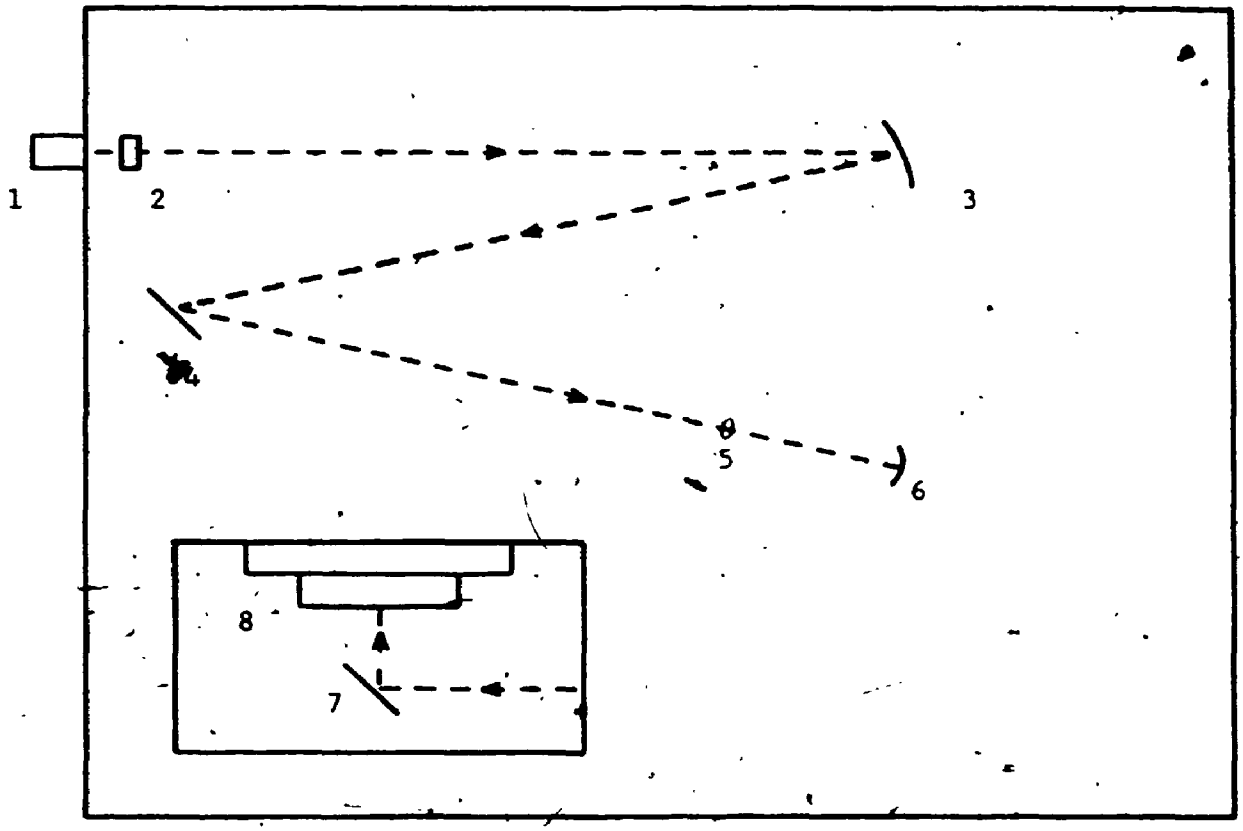

Figure 2.1. A schematic of the Coudé spectrograph.

This is a top view showing:

1) the image slicer; 2) the filter;

3) the collimator; 4) the grating;

5) the corrector lens; 6) the camera mirror.

The inset is a side view of the area between the lens and the camera. It shows:

7) the pick-off mirror; 8) the detector.

detector. The detector and pick-off mirror are, in turn, mounted on a precision screw table which allows the whole assembly to be moved along the optical axis. Rotation of the image relative to the Reticon can be accomplished by rotating the screw table. Stepping motors connected to the screw table and pick-off mirror allow these to be adjusted using controls in the observer's room.

2.2 The Detector System

At the heart of the detector system is an RL-1872/F Reticon chip. This is a linear array of 1872 silicon photodiodes, each diode measuring 15 μm wide by 750 μm long, with effectively no dead space between adjacent diodes. Associated with each diode is a small capacitance. To carry out an integration the diodes are first charged to a voltage of 5 V to erase any residual signal left from the previous exposure. To ensure complete erasure, three charging cycles are performed. Depletion of the charge on the diode circuit occurs through either thermal leakage or the absorption of photons. To minimize thermal leakage the Reticon chip is refrigerated with liquid nitrogen. At the end of an integration the accumulated signal is read out by a shift register scanning circuit built into the Reticon chip. Immediately thereafter, a series of ten second dark exposures are taken, and subtracted from the stellar signal in order to remove the fixed pattern signal (see Vogt, Tull, and Kelton 1978). Four dark exposures are taken in order to reduce the component of the readout noise occurring in them by a factor of two.

The signal passes from the array to the preamplifier and amplifier circuitry along four video lines. Once amplified, it goes through a multiplexer, which converts the four lines to two. It is then integrated and shaped by circuitry on the DISH (DIfferential Sample and Hold) board. The integrated signal continues to an analog-to-digital converter, which reduces it to a digital form acceptable to the controlling computer (a Nova 3/12). The Nova 3/12 runs the program GRARET 1.0 (originally developed by Phillip Kelton of the University of Texas, and later modified by D.F. Gray) which controls integration times, and start pulses, and allows the manipulation, display, and storage of the data. The data are displayed on a Tektronics 602 display.

The dynamic range of the system is approximately 3000 - 3500. Linearity is assumed over this entire range.

2.3 The Flat-field Lamp and the Instrumental Profile

Amplifier gain differences on the four video lines produce a periodic signal in the data. By dividing the "raw", stellar data by a flat-field lamp spectrum, these diode-to-diode gain differences can be removed. The flat-field lamp is measured by taking a short exposure (~ 1 s.) of a ribbon lamp placed on the optical bench in front of the image slicer. A measurement is taken at the beginning of each night and again after any changes to the grating angle and/or filter. Figure 2.2 shows a typical flat-field lamp exposure.

Exposures of the λ5461 line of mercury are made to determine the

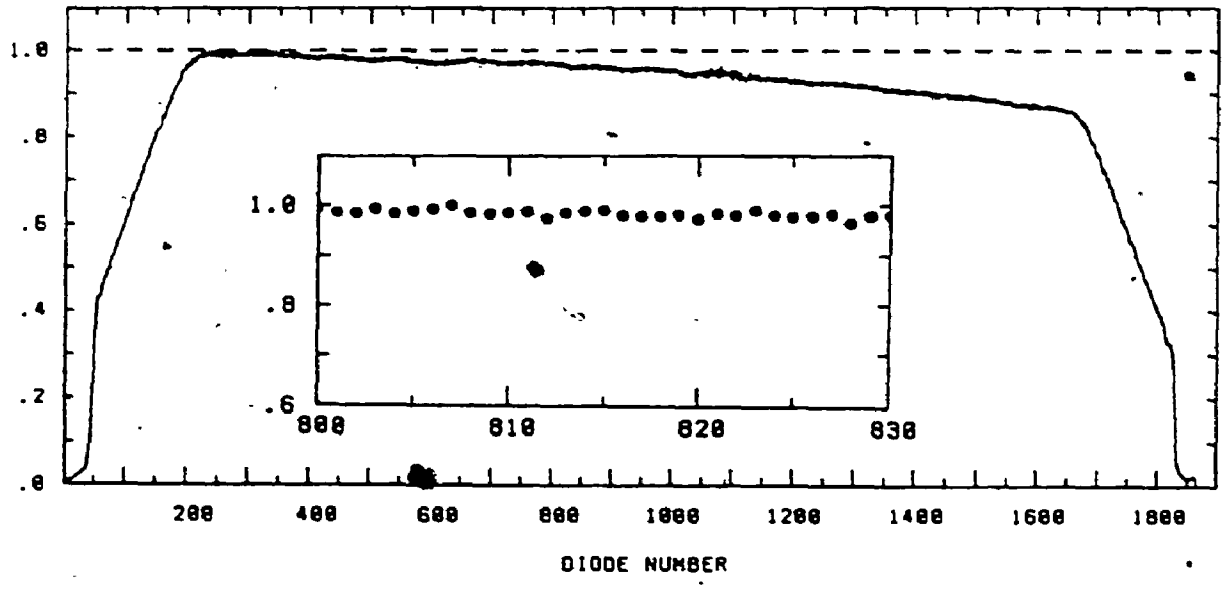

Figure 2.2 A typical flat-field lamp exposure. The ordinate is in discrete units corresponding to individual diodes, and the abscissa is the maximum signal normalized to unit height. The inset is an enlarged view of a small region of the spectrum showing the diode-to-diode variations, caused by amplifier gain differences on the four video lines.

width and shape of the instrumental profile. A microwave-excited, air-cooled, single-isotope mercury lamp is used as the source. At a temperature of ~ 27° C the thermally broadened line has a half-width of ~ 5 mÅ (Gray 1976). Since the spectrograph resolution is much lower than this, the instrumental profile is essentially given by the observed line profile, without correction for the natural line width. A representative measurement is shown in Figure 2.3. The resolution, as measured by the half-width of the mercury line, is ~ 70 mÅ (corresponding to ~ 2 diodes FWHM). The shape of the instrumental profile is found to be highly symmetric.

2.4 Observational Procedure

An observing session begins by filling a 1.8 litre dewar with liquid nitrogen, and turning on the support electronics. Several hours (2 to 4) are then needed for the system to stabilize. Once this time has passed, the readout noise of the system is measured by taking a series (usually 6) of one second dark exposures. The standard deviation of diodes 200 through 1600 (representing the portion of the array over which one finds usable data) is determined for each of these exposures. The mean standard deviation is taken as the readout noise for that session. Typically, this is ~ 1.1 analog-to-digital units (ADU) per readout.

Next, the camera focus is checked by measuring the spectrum produced by an iron hollow cathode tube placed on the optical bench in front of the image slicer. This spectrum consists of a series of

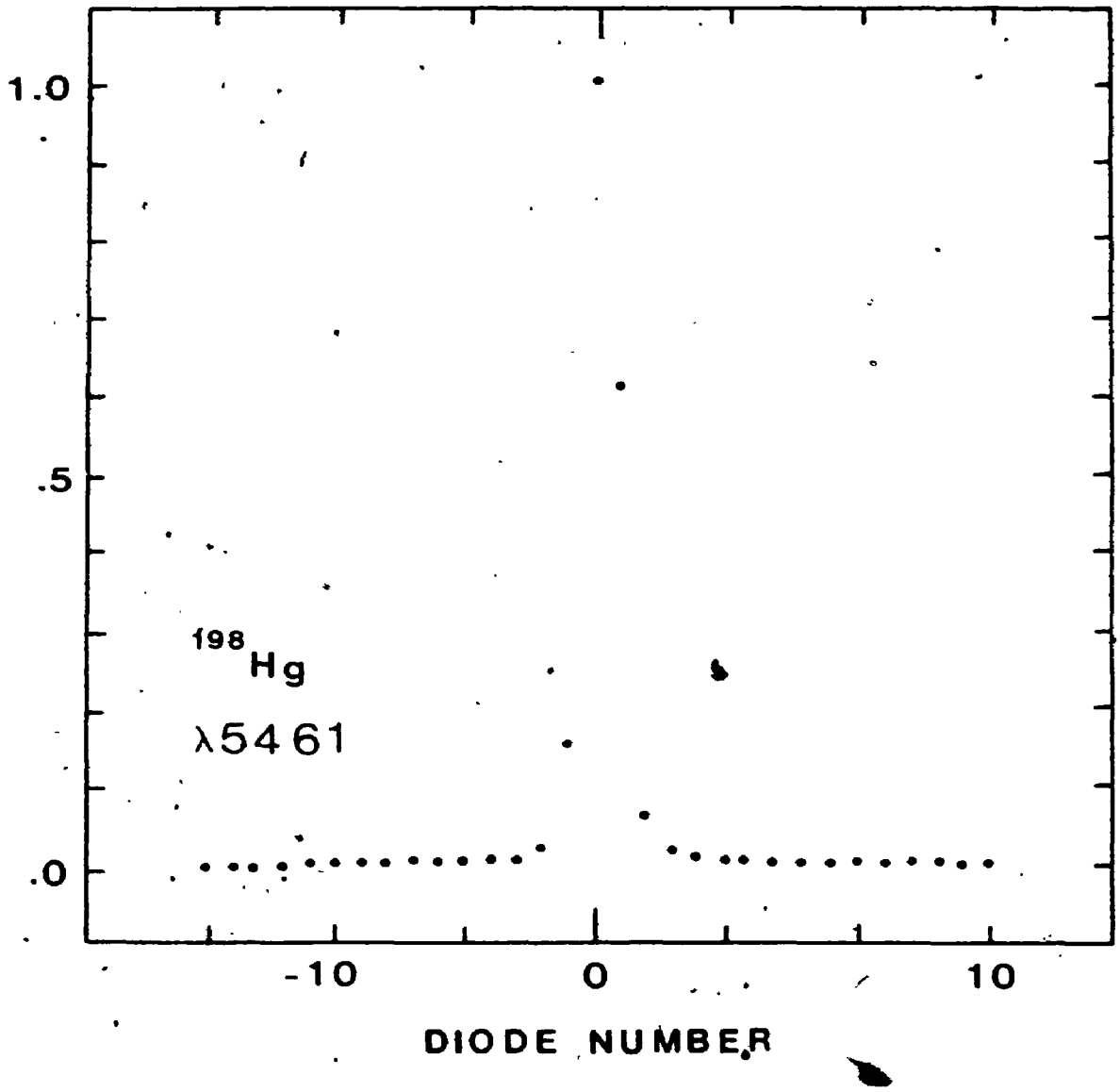

Figure 2.3 A representative instrumental profile measurement. The axes are as in Figure 2.2. The zero of the ordinate has been arbitrarily taken to correspond to the peak of the curve.

emission lines of various strengths. The grating is rotated to position a medium strength line slightly off center of the array. The position of the detector assembly relative to the camera is then adjusted by means of a control box in the observer's room. At each position a 5 second exposure is taken, and the image of the line examined. When the line is in sharpest focus, 2 - 3 diodes FWHM, the procedure is stopped.

Finally, the position of the imaged spectrum across the face of the Reticon is checked by taking a series of exposures of the flat-field ribbon lamp. Between each exposure, the angle of the pick-off mirror is adjusted. Proper centering of the image is indicated when the signal per diode reaches a maximum. A flat-field lamp exposure is recorded prior to the first observation and again after any changes made to the grating angle and/or filter.

A stellar exposure is performed by centering the image of ξ Boo on the entrance slot of the image slicer. Under favourable conditions the entire seeing disk of the primary passes through the slot, while the secondary is clearly visible above the slot. Guiding is performed by viewing the face of the image slicer with an ISIT camera mounted off to the side. The TV monitor and telescope controls are located in the observer's room. A partially silvered mirror, placed directly behind the image slicer, deflects ~ 10% of the light into a standard GaAs photomultiplier. By monitoring the accumulated number of counts recorded by the photomultiplier, the signal being built up on the Reticon can be estimated. Counts in the range of 2 - 3 million are needed.

Exposure times depended on the seeing conditions and the degree of cloud cover. On clear nights, with good seeing, integrations of ~ 2 hours were sufficient to give data having a signal-to-noise of a few hundred. When the seeing was less than ideal, or when there were clouds, integration times would have to be increased, sometimes up to ~ 3.5 hours. There were nights when deteriorating weather conditions forced an exposure to be cut short, and this resulted in data having less than the preferred quality. In June of 1987 the coudé train mirrors were overcoated to increase their reflectivity. This yielded a gain of a factor of ~ 1.5 - 2 in the overall efficiency, and exposure times were correspondingly reduced.

2.5 The Data

All observations were made with the coudé spectrograph and Reticon detector described previously. Working in ninth order allowed some 65 Å of speetrum to be recorded. By far the majority of the observations were made in the spectral region surrounding λ6250. This wavelength interval was chosen because it contains several reasonably unblended, medium strength lines. Six observations in the λ6150 region were recorded in the 1987 season in order to measure the magnetically sensitive line λ6173.34, and to check that the observed asymmetry variations are not an artifact of the original choice of spectral lines. The dispersion was ~ 0.037 Å per diode in the λ6250 region and ~ 0.039 Å in the λ6150 region. The resolution was ~ 3.5 km s^{-1} ($\lambda/\Delta\lambda$ ~ 90,000).

The 121 exposures of ξ Boo A listed in Appendix 1 remained after culling out those having a signal-to-noise (S/N) less than about 100. Data from the four observing seasons of 1984 through 1987 are included in this list. When possible, more than one exposure was made per night. The Julian Date for the midpoint of each exposure is given in column 2, while column 3 lists the S/N (calculated using equation 2-7b, see section 2.6). The S/N ranges from ~ 100 to ~ 600, with the mean for the 1986 and 1987 seasons being somewhat higher than that of the 1984 and 1985 seasons. The remaining columns will be explained in the next chapter. The six λ6150 exposures taken in 1987 are indicated by asterisks next to their entry in the table.

A typical spectrum for ξ Boo A in the λ6250 region is shown in Figure 2.4. The ordinate is in discrete units corresponding to individual diodes. The abscissa is the maximum signal normalized to unit height. A number of spectral lines have been identified in the figure.

2.6 Sources of Noise in the Data and the Derived S/N

There are three principal sources of noise in the data: 1) photon noise arising from the irregular arrival times of the photons; 2) readout noise arising from several sources within the Reticon system and representing the inherent uncertainty with which signals can be extracted from the array; and 3) thermal leakage. The total noise is then a combination of these. If n is the total number of photons collected per diode, r is the readout noise in equivalent

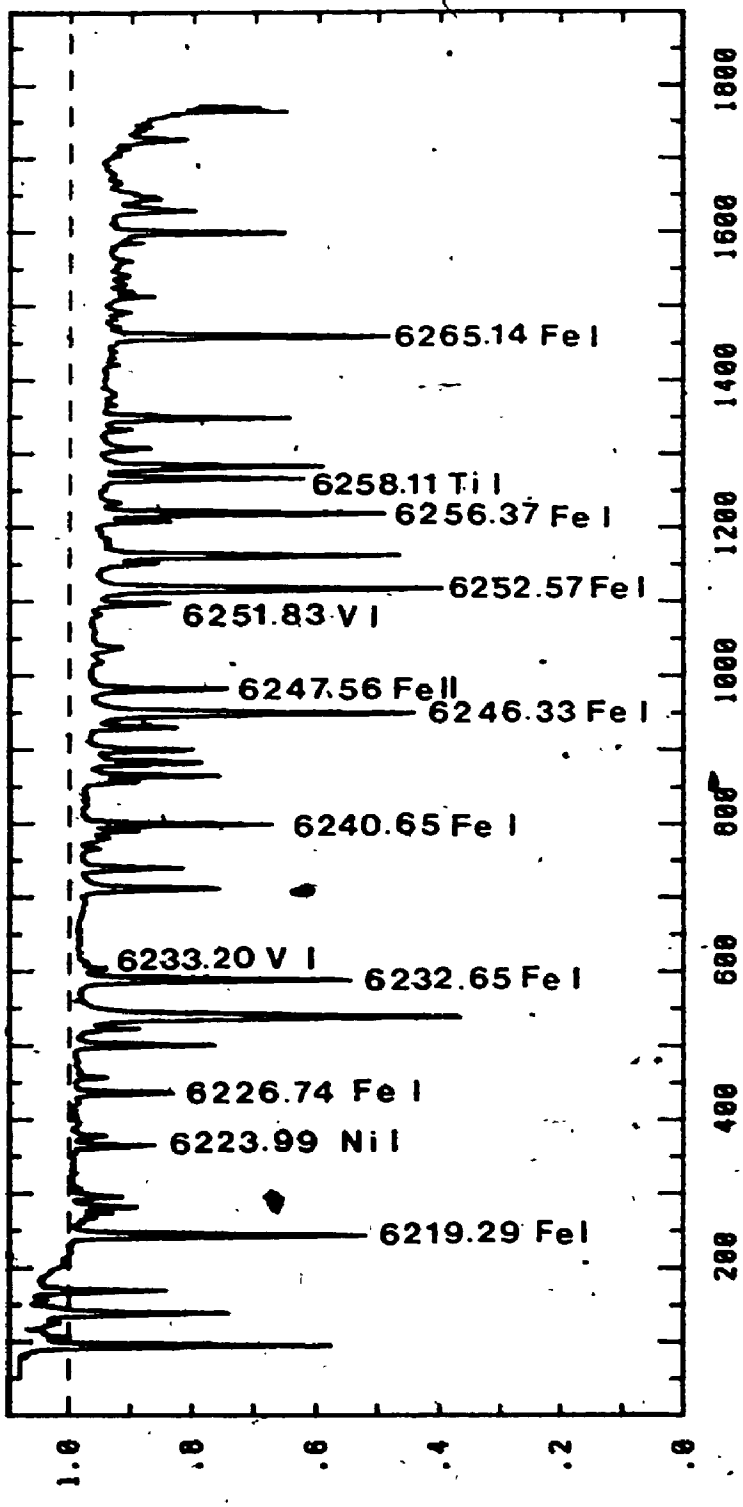

Figure 2.4 A typical exposure of ξ Boo A in the λ6250 region. The spectrum has been divided by the flat-field lamp, and a correction for the 8-point instrumental signal has been applied (see next chapter). A number of spectral lines are identified. The axes are as before.

photons, and n_{th} is the thermal leakage, then the total noise, δn, is given by

$$\delta n \cong \sqrt{r^2 + n + n_{th}} \qquad 2\text{-}1$$

As a means of checking the thermal leakage, ~ 60 diodes at each end of the Reticon array are masked with aluminum foil. This prevents photons from striking these diodes, and so any signal found there is due to thermal leakage, rather than the capture of photons. In general, this signal is found to be < ~ 1% of the maximum, and therefore, thermal leakage is not an important source of noise in these data. Henceforth, the thermal component of the noise will be omitted.

Since the signal returned from the Reticon is given in analog-to-digital units (ADU), as opposed to the number of photons captured, we must determine the conversion factor between ADU and photons. If we define the quantities N, R, and δN as the equivalent quantities given earlier (with thermal leakage omitted), but in ADU, then the conversion factor, u, (in ADU per photon) can be defined such that the following relations hold:

$$\delta N = u\delta n \qquad 2\text{-}2$$

$$N = un \qquad 2\text{-}3$$

$$R = ur \qquad 2\text{-}4$$

The total noise in ADU then becomes,

$$\delta N \cong u\sqrt{r^2 + n} \qquad 2\text{-}5a$$

$$= \sqrt{R^2 + uN} \qquad 2\text{-}5b ,$$

and solving for u we get,

$$u = (\delta N^2 - R^2)/N \qquad 2\text{-}6 .$$

All quantities on the right of equation 2-6 can be determined with a few simple measurements. The readout noise, N, is measured nightly as explained in section 2.4, and is typically ~ 1.1 ADU per readout. δN^2 is found by taking two exposures of the flat-field lamp (both having the same signal per diode), and dividing one into the other — δN^2 is immediately obtained from the variance of the quotient. The mean signal per diode is N, and from equation 2-6, u is found to be in the range 1/600 - 1/700 (D.F. Gray, private communication). A value of 1/700 has been adopted, meaning that the readout noise is equivalent to the absorption of ~ 700 photons.

The signal-to-noise ratio of the data is therefore given by,

$$S/N = N/\sqrt{R^2 + uN} \qquad 2\text{-}7a$$

$$\cong N/\sqrt{R^2 + N/700} \qquad 2\text{-}7b .$$

At low signal levels the readout noise dominates over the photon noise, but for signal levels greater than ~ 700 ADU the photon noise begins to become important. Since the typical signal-to-noise ratios for the data used here are in the range of ~ 100 to ~ 600, photon noise makes up ~ 15% to ~ 40% of the total noise.

CHAPTER 3

Analysis of the Data

3.1 Preliminary Treatment of the Data

A common, and undesirable, trait of Reticon data is the presence of an 8-diode instrumental signal, which is seen in these data as a 4 + 4 diode square wave, superimposed on each spectrum. The signal is found to be most pronounced in the first exposure taken during a night and also in low S/N data which required long exposure times (due to poor seeing and/or weather conditions). In general, the instrumental square wave has an amplitude less than ~ 1% of the maximum signal, and in the worst cases is ~ 2% - 3%. The signal is removed from the data by calculating its mean amplitude across the entire array, and then dividing a square wave of this amplitude from the data. Since spectral lines influence the calculation, these are removed by excluding any diodes with a signal level below 0.95 of the surrounding continuum. In this way, the amplitude of the instrumental square wave is reduced to less than ~ 0.10% of the maximum signal. Figure 3.1 shows a region of a typical spectrum before and after correction for the instrumental square wave.

The linear dispersion across the array is determined by fitting a second order polynomial to the line positions and their wavelengths. The spectral lines are identified with the aid of "The Solar Spectrum 2935 Å to 8770 Å (Moore, Minnaert, and Houtgast 1966), and "A High

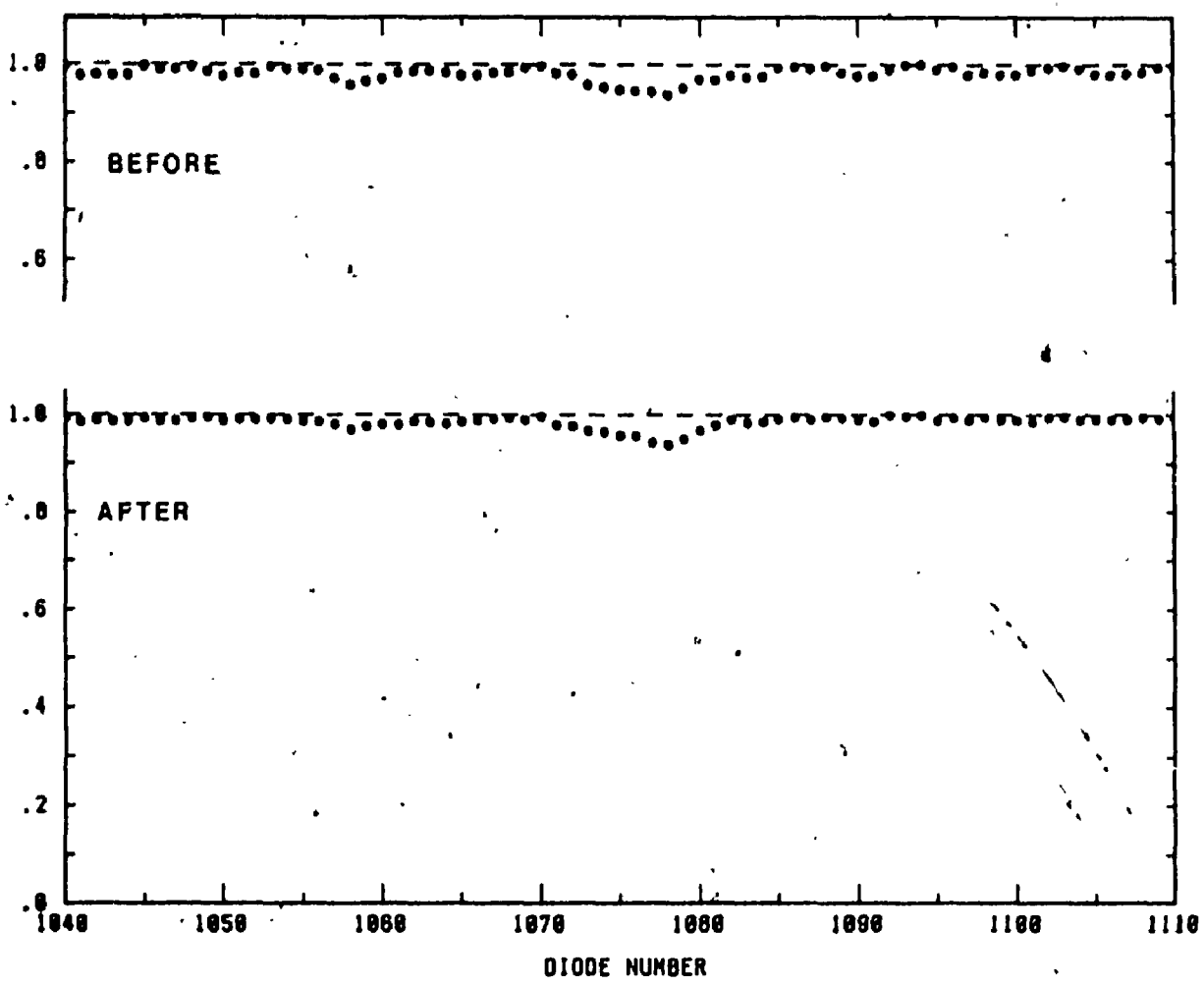

Figure 3.1 A relatively line-free region of a typical spectrum is shown. The upper panel is before correction for the 8-point instrumental signal. The lower panel shows the same spectral interval after dividing out a square wave of ~ 1.0% of the maximum signal.

Resolution Spectral Atlas of the Solar Irradiance From 380 to 700 Nanometers" (Beckers, Bridges, and Gilliam 1976). The diode value of the line center, estimated to about two tenths of a diode, is used as its position.

3.2 The Line Asymmetries

For this study the line asymmetry is defined in terms of the line bisector. The bisector has several characteristics which make it very useful: 1) it provides a simple means of visually presenting the line asymmetry, while being easily understood; 2) it allows averaging over several lines; and 3) it can be edited when the line wings are blended. A line bisector is constructed by computing the midpoints of horizontal line segments bounded by the sides of the line profile. For each point on the left of the profile, the matching point on the right is found using a modification of the cubic-spline interpolation routine by Hill (1982). To improve the definition of the bisector, the number of points on the left side of the profile is increased by a factor of two, using the same interpolation. The velocity error for each point on the bisector is determined from the photometric error and profile slope following Gray (1983). (A discussion of bisector errors can also be found in section 3.2.4.)

Line blends are, and will probably remain, a significant source of uncertainty when calculating the intrinsic line asymmetry. However, in this study, it is the variation of the bisector shape which is of primary interest; and so consistency in the treatment of

blends is the most important concern. This is not to say that any line can be used in the analysis. Strong lines are preferred because they contain a relatively large number of points (which is needed when calculating the bisector), and because their steeper slopes mean smaller bisector errors. Additionally, the lines should be as blend-free as possible, since the intrinsic bisector shape provides important information about stellar granulation. This also necessitates averaging over several lines in order to reduce the effects of unkown blends (and, of course, to reduce the noise). With these considerations in mind, the eight lines marked with an asterisk in Table 3.1 were selected as the most suitable in the λ6250 region.

Bisectors are calculated for each of the eight lines, and used to construct a composite plot. Since there is no information on the center of mass motion of the star, and hence no absolute wavelength reference, the individual bisectors in the composite are shifted horizontally so they overlap. The bisectors which are affected by known blends are edited at this point by removing the upper portion of the bisector. The amount removed depends on the severity of the blend. Occasionally, spurious noise causes a normally well behaved bisector to disagree with the composite, and in such cases the affected bisector is omitted. The remaining bisectors and bisector portions are then used to calculate a weighted mean line bisector for the exposure. Figure 3.2 shows an example of a composite plot and its mean.

Figure 3.3 shows the effect of removing the instrumental profile, and the effect of applying a low-pass Fourier filter (Brault and White

Table 3.1

The Spectral Lines
(λ6250 region)

λ (Å)	Ion	χ (eV)	RMT[a]	g_{eff}[b]
6219.29	Fe I	2.20	62	1.67*†
6223.99	Ni I	4.10	228	1.00†
6226.74	Fe I	3.88	981	1.38†
6232.65	Fe I	3.65	816	2.00*†
6233.20	V I	0.28	20	1.49†
6240.65	Fe I	2.22	64	1.00*
6246.33	Fe I	3.60	816	1.58*
6247.56	Fe II	3.89	74	1.10†
6251.83	V I	0.29	19	1.59†
6252.57	Fe I	2.40	169	1.08*
6256.37	Fe I	2.45	169	0.92*†
6258.11	Ti I	1.43	104	1.00*
6265.14	Fe I	2.18	62	1.58*†

[a] from Moore et al. 1966

[b] from Beckers 1969

* lines used for bisector analysis (section 3.2)

† lines used for line broadening analysis (section 3.4)

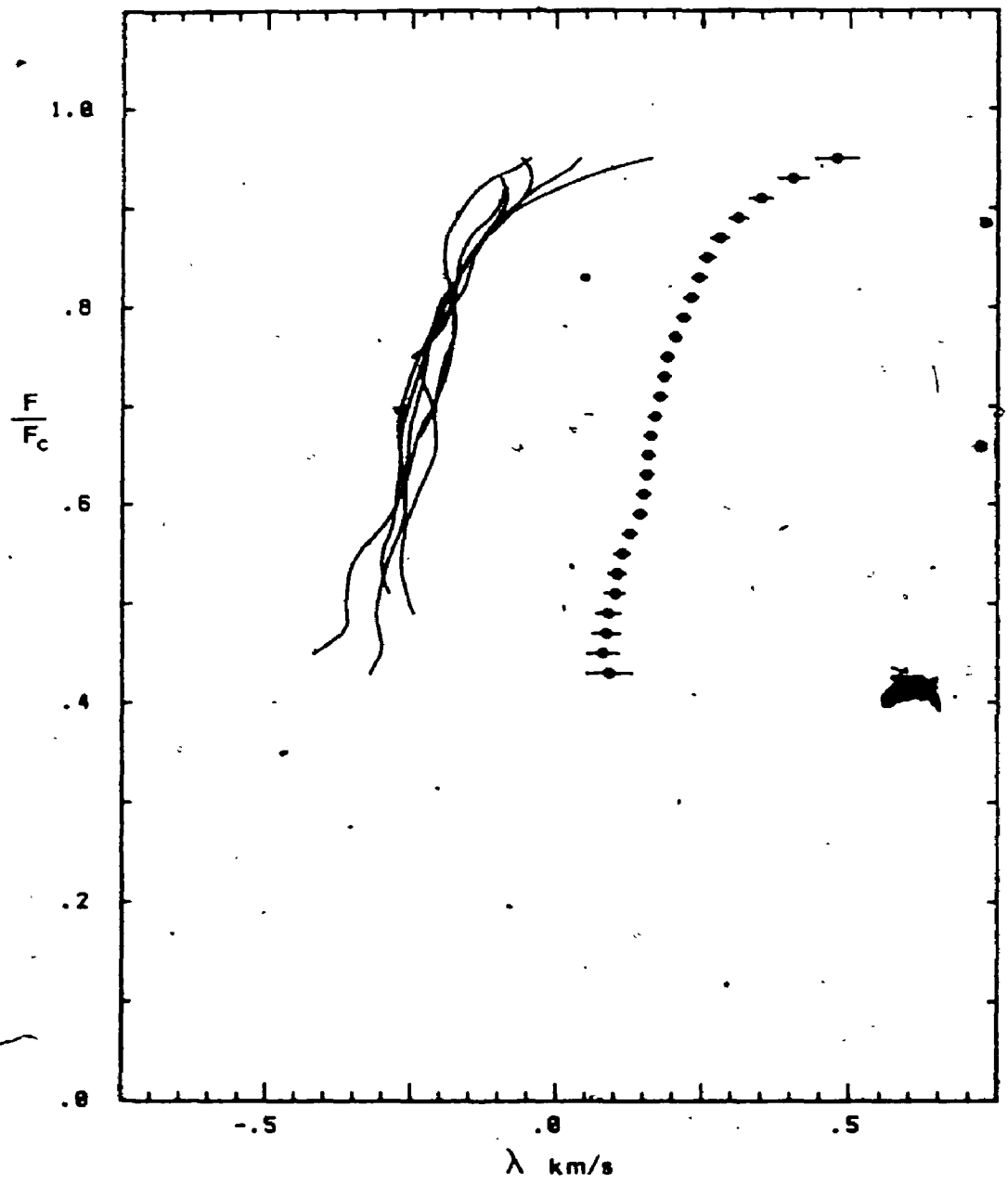

Figure 3.2 The line bisectors are shown for a single exposure of ξ Boo A. F/F_c is the flux expressed as a fraction of the continuum flux. On the left is a composite of the individual bisectors, while on the right is the mean bisector.

1971; Gray 1976). Composite plots are shown for three cases: case a) instrumental profile not removed; case b) instrumental profile removed and a low-pass Fourier filter applied; and case c) only a low-pass filter applied. The same line asymmetry is reproduced in all cases (within errors), but the scatter between the individual bisectors is smallest for case c. This improvement is due to the fact that the line bisectors have no physically real high frequency components in them, so that filtering away the high frequency noise improves the overall noise figure. For this reason a low-pass Fourier filter was applied to the data, without removing the instrumental broadening.

3.2.1 The Line Bisector Variations

A time series of mean line bisectors was generated by calculating a mean bisector for every exposure. Because each bisector is a multi-valued function, such a time series is not easily analyzed for periodicities. Several classifications schemes were tried to reduce the line bisector variations to a form more amenable to periodogram analysis. The method finally adopted was to classify each bisector in terms of its "velocity span".

The velocity span is calculated by taking the difference in velocity between a point near the top of the bisector and a point near the bottom. The points are optimized for this data set in the following manner. A first approximation for the upper point is selected, and held fixed while a series of points near the bottom of the bisector are tried. For each pair of points the velocity span and

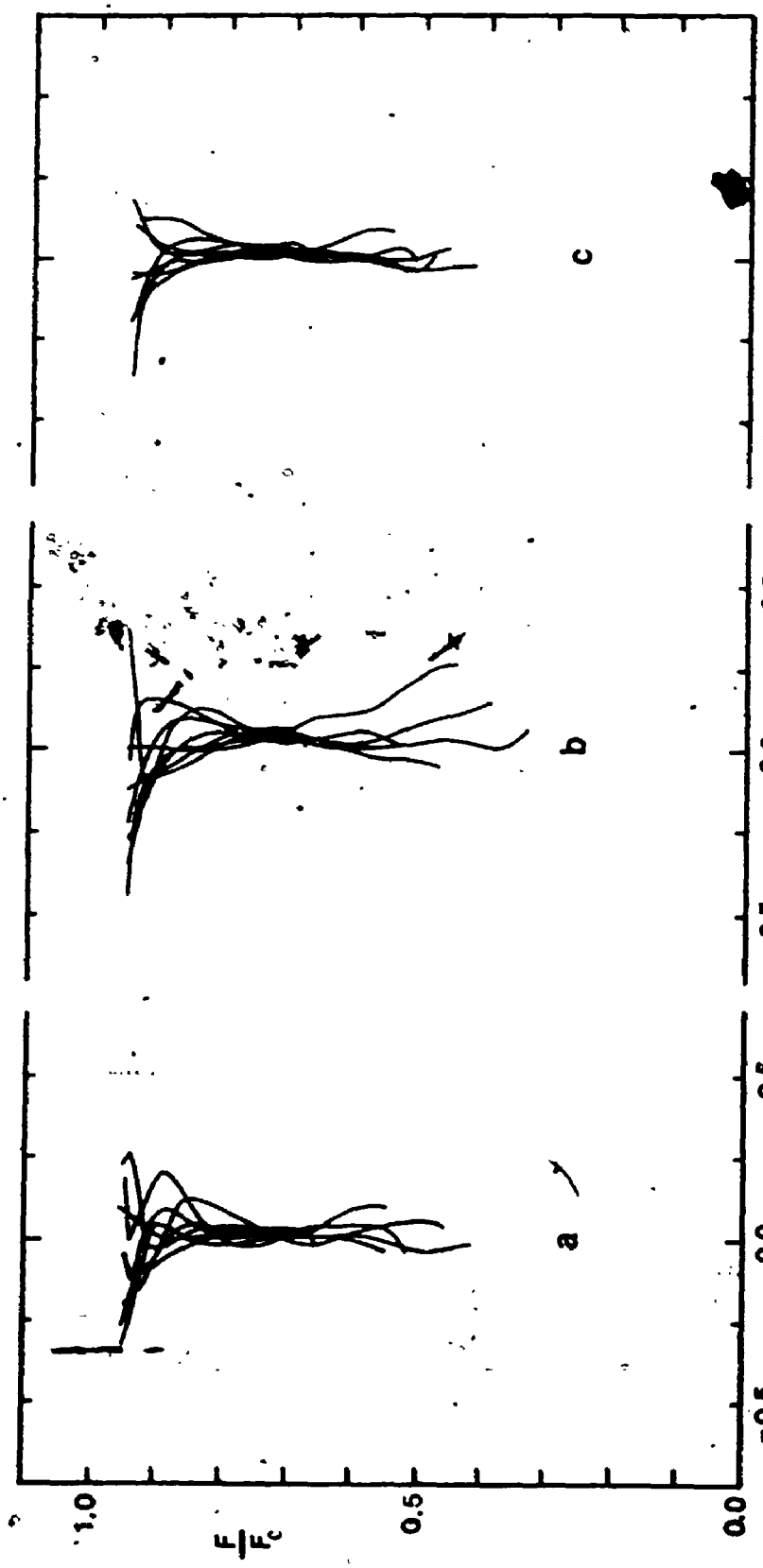

Figure 3.3 The effect of removing the instrumental profile, and the effect of applying a low-pass Fourier filter. Composite plots are shown for three cases: case a) instrumental profile not removed; case b) instrumental profile removed and a low-pass Fourier filter applied; and case c) only a low-pass filter applied. The scatter between individual bisectors is minimum for case (c).

its error are calculated for all of the mean bisectors. Summing the individual velocity-span errors over the entire data set and dividing the sum by the length of the lever arm (i.e. the difference between the upper and lower points) yields a "goodness of choice" parameter (GOCP), i.e.,

$$GOCP = \frac{\sum_i \delta VS}{\left[(F/F_c)_{upper} - (F/F_c)_{lower} \right]} \qquad 3\text{-}1.$$

In Figure 3.4a we see how the GOCP behaves when the upper point is held fixed at $F/F_c = 0.90$, and the lower point is varied. We see that the GOCP decreases rapidly as the lower point is moved down the bisector. This is due to the increasing length of the lever arm. At $(F/F_c)_{lower} \cong 0.55$ a minimum is reached and the GOCP begins to increase due to the increasing velocity errors found in this part of the bisectors. The value $F/F_c = 0.55$ is taken as the optimum for the lower point. The upper point is determined in a similar fashion except that the lower point is held fixed at $F/F_c = 0.55$ while the upper point is varied. The minimum in this case occurs at $F/F_c \cong 0.87$ (Figure 3.4b). The velocity spans, and their errors[1], are given in the fourth column of Table A-1 (see Appendix A).

The velocity spans were then Fourier analyzed using the method

[1] *See section 3.2.4 for a explanation of how the velocity span errors are calculated. The mean error is found to be:* 30 ± 15 m s^{-1}.

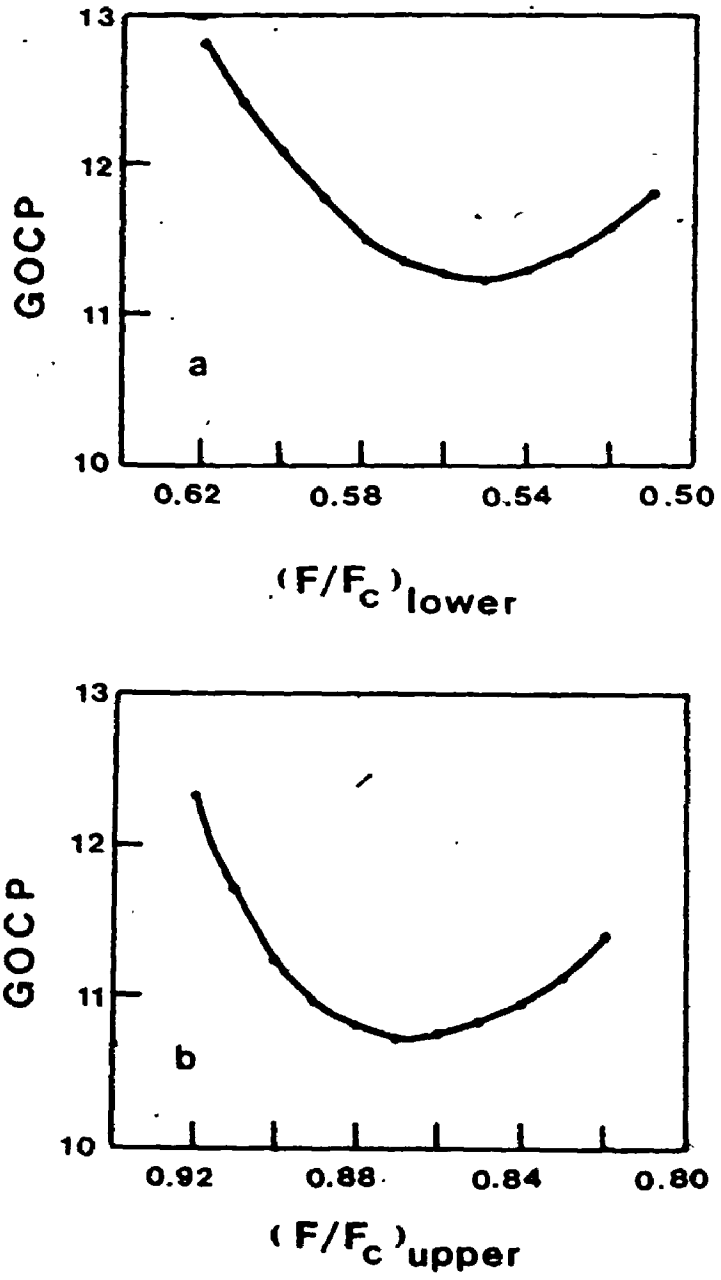

Figure 3.4 Optimizing the points used to calculate the velocity span. (a) shows the behavior of GOCP when the upper point is held fixed at $F/F_c = 0.90$, while the lower point is varied. (b) shows the behavior of GOCP when the lower point is held fixed at $F/F_c = 0.55$, and the upper point is varied. (GOCP is defined in the text.)

described by Matthews and Wehlau (1985). As with the often used Scargle method (Scargle 1982), this method treats unequally spaced data without bias, but it is computationally faster. Individual seasons and the entire data set were examined. Of the individual seasons, only 1986 has a complete enough data set for an accurate period determination. The amplitude spectrum for 1986 is shown in the upper panel of Figure 3.5. The most significant peak gives a period of 6.40 days, with an amplitude of 64 m s^{-1} (meaning a peak-to-peak change of 128 m s^{-1}). The lower panel of Figure 3.5 shows the amplitude spectrum for the entire data set. The most significant peak here gives a period of 6.43 days, with an amplitude of 45 m s^{-1}. The difference in amplitude and period between these two cases might easily arise from incomplete phase coverage in the 1984, 1985, and 1987 seasons.

Undoubtedly, the period measured here is the same one detected in the rotational modulation studies of the H and K-line emission (Noyes et al. 1984; Baliunas et al. 1985), where the published values range from 6.2 to 6.7 days. One infers from this that the underlying cause of the bisector variations must also be some type of surface feature, carried around the star by rotation.

There are other apparently significant peaks in both spectra, but they can be explained as harmonics produced by the nonsinusoidal shape of the velocity-span curve (see Chapter 5). The r.m.s. noise level is estimated from figure 3.5 to be ~ 20 to 25 m s^{-1}, which is in excellent agreement with the calculated mean error of 30 ± 15 m s^{-1}. The Fourier spectra of the sampling windows are shown in Figure 3.6.

Figure 3.5 The Fourier amplitude spectra of the velocity spans for a) the 1986 season, and b) the entire data set. The amplitude is in m s^{-1}. The most significant peak in (a) gives a period of 6.40 days, with an amplitude of 64 m s^{-1} (128 m s^{-1}, peak-to-peak). The most significant peak for the entire data set gives a period of 6.43 days, with an amplitude of 45 m s^{-1}.

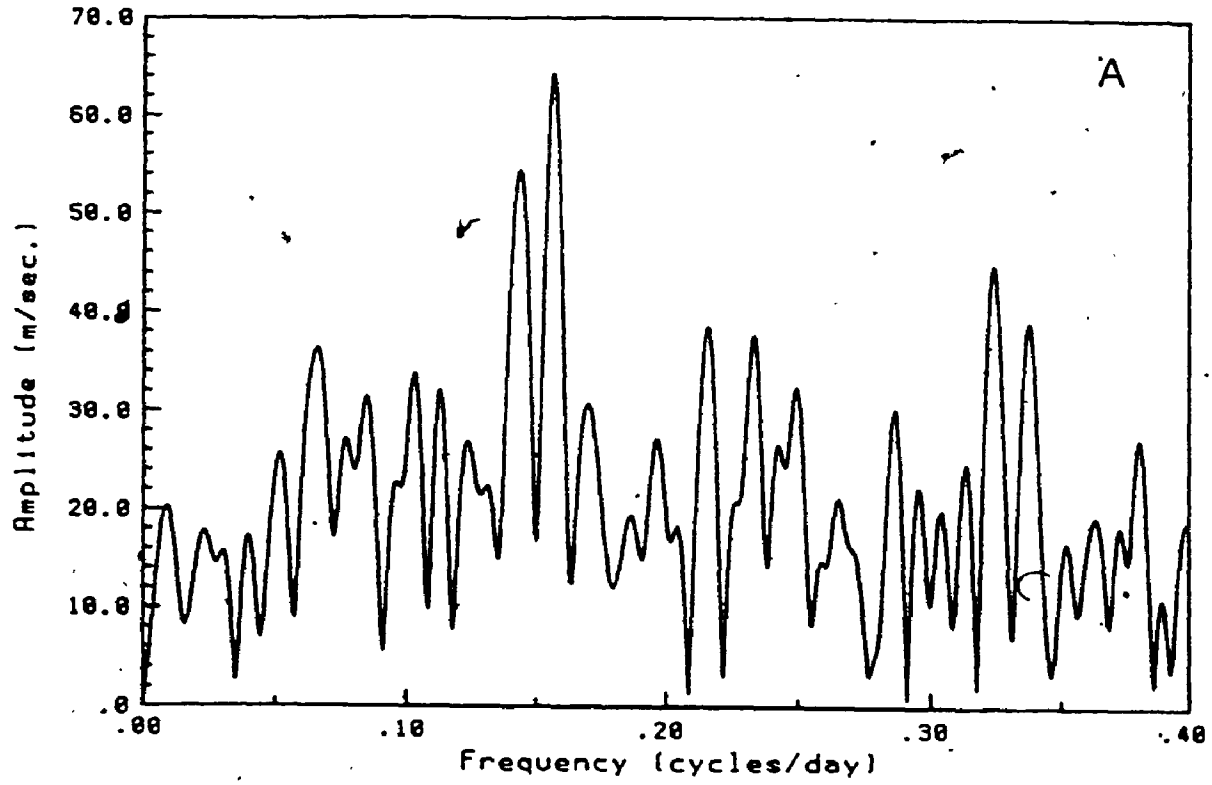
A
70.0
60.0
50.0
40.0
30.0
20.0
10.0
.0
Amplitude (m/sec.)
.00
.10
.20
.30
.40
Frequency (cycles/day)

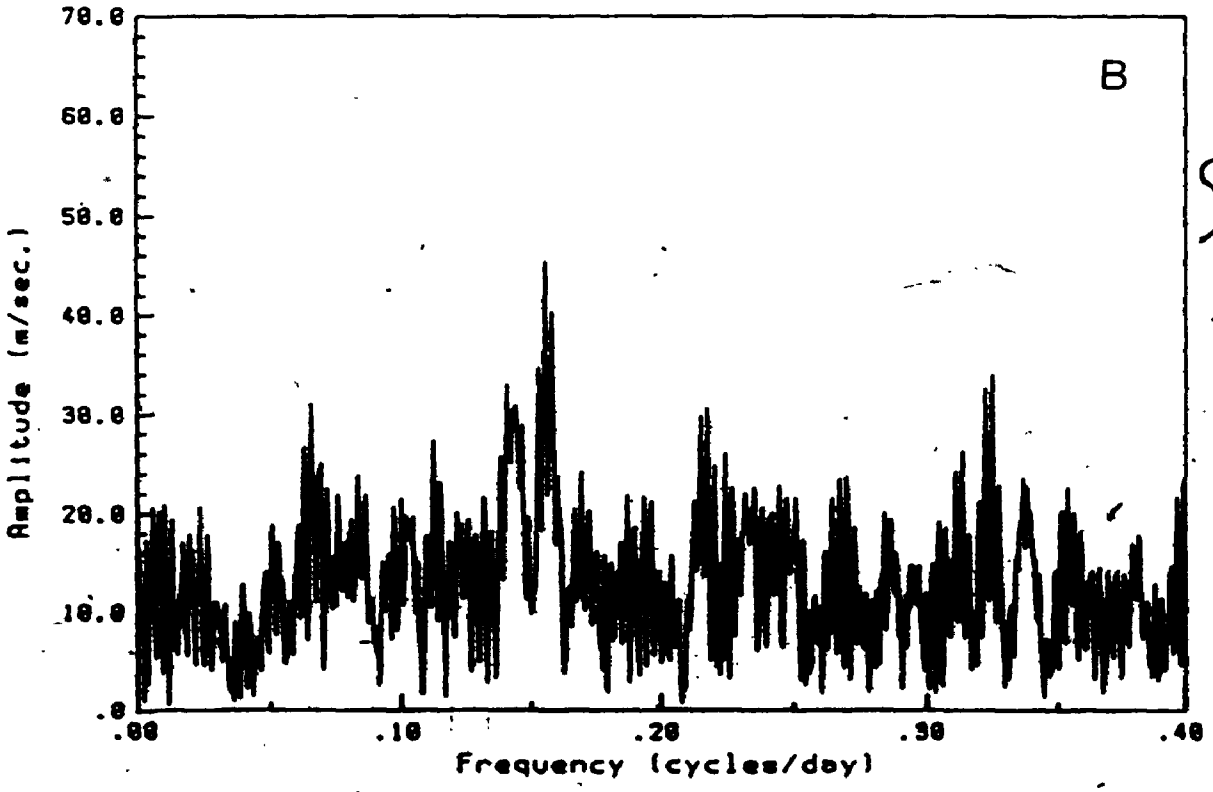
B
70.0
60.0
50.0
40.0
30.0
20.0
10.0
.0
Amplitude (m/sec.)
.00
.10
.20
.30
.40
Frequency (cycles/day)

Figure 3.6 The Fourier spectra of the sampling windows for: a) the 1986 season, and b) the entire data set. They have been shifted to the periods found from Figure 3.5, in order better compare their shape. The triplet nature of the peaks in Figure 3.5 is seen to be due to the window function.

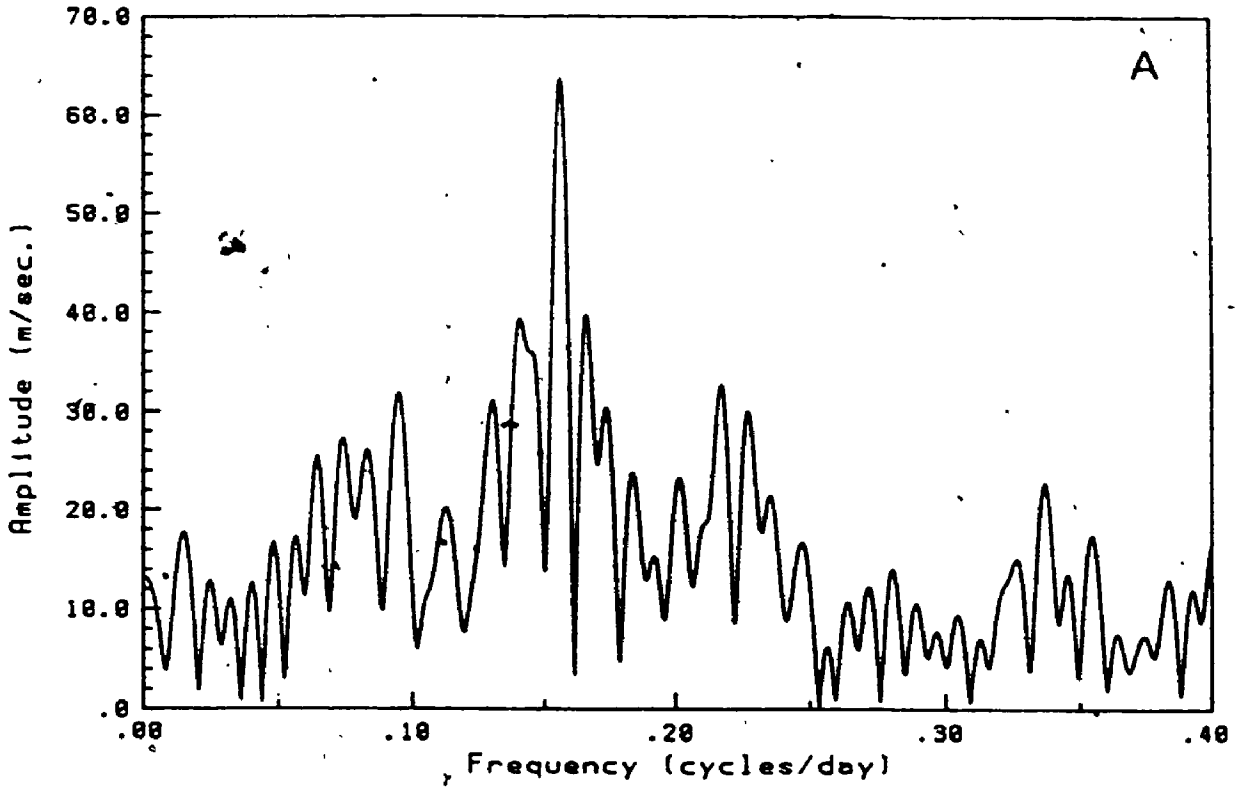
A
70.0
60.0
50.0
40.0
30.0
20.0
10.0
.0
Amplitude (m/sec.)
.00
.10
.20
.30
.40
Frequency (cycles/day)

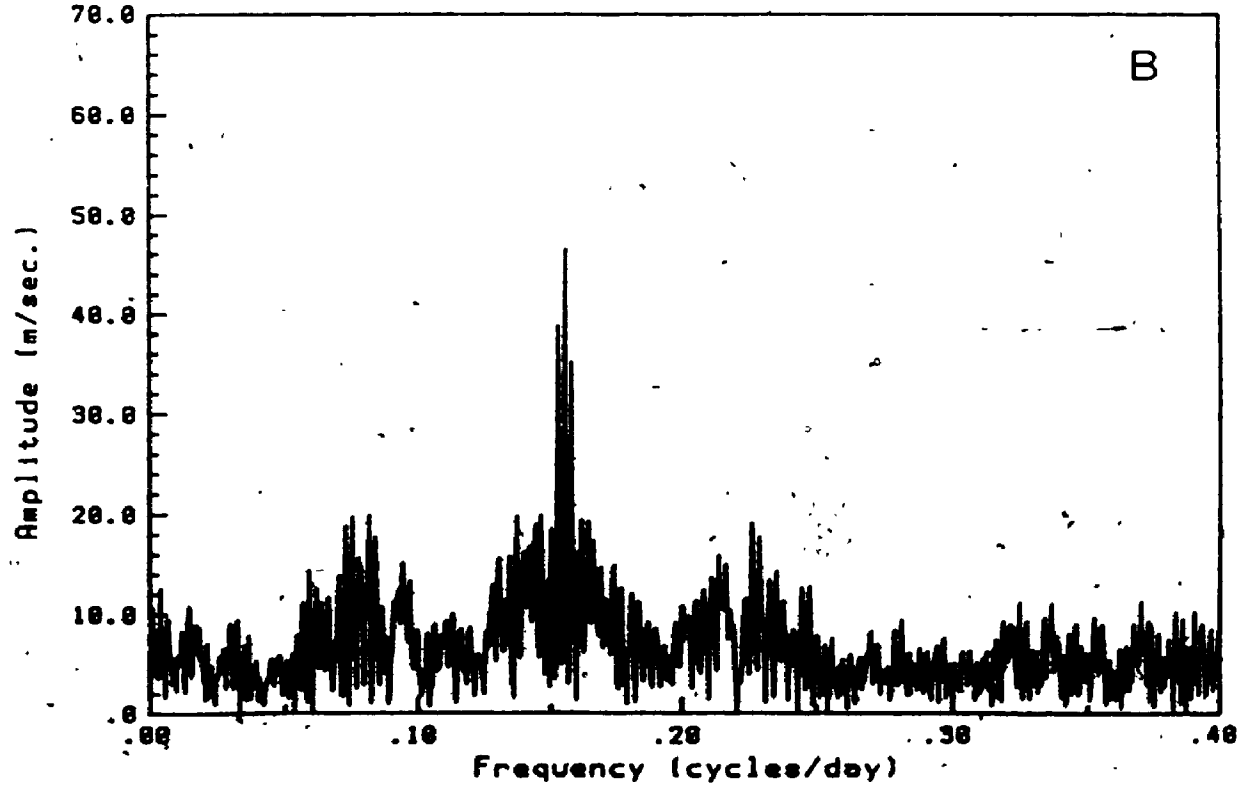
B
70.0
60.0
50.0
40.0
30.0
20.0
10.0
.0
Amplitude (m/sec.)
.00
.10
.20
.30
.40
Frequency (cycles/day)

The triplet nature of the peaks is seen to be due to the window function.

The periods found above were used to generate phase diagrams of the mean line bisectors. These are presented in Figure 3.7. At the top are the mean bisectors for the 1986 season alone, and directly below this are the means for the entire data set. Zero phase has arbitrarily been taken at the time of the first 1986 observation (JD 2446523.684). In order to make the diagram as uncluttered as possible only the phase averaged bisectors are shown. The phase means were calculated using the following procedure. First, the bisectors are phased together using the period determined previously. These are then grouped by phase into bins of width 0.1 in phase, and finally the bisectors within each bin are averaged. Since the noise increases rapidly as the continuum is approached, and again near the cores of the lines, the upper and the lower ~ 6% of each bisector has been removed. Going from left to right across the diagram there is a continuous and systematic change in bisector shape. At phase ~ 0.0 the bisector is curved slightly to the right. Moving to phase ~ 0.25 the bisector becomes nearly vertical, then the curvature increases again, reaching a maximum near phase 0.55. The bisector returns almost to its original shape by phase ~ 0.8. The remaining two tenths of the cycle show very little change, with the bisector remaining curved slightly rightward.

The six observations of the λ6150 region obtained in 1987 were also examined for asymmetry changes. The lines used for this spectral region are listed in Table 3.2. They were picked using the same

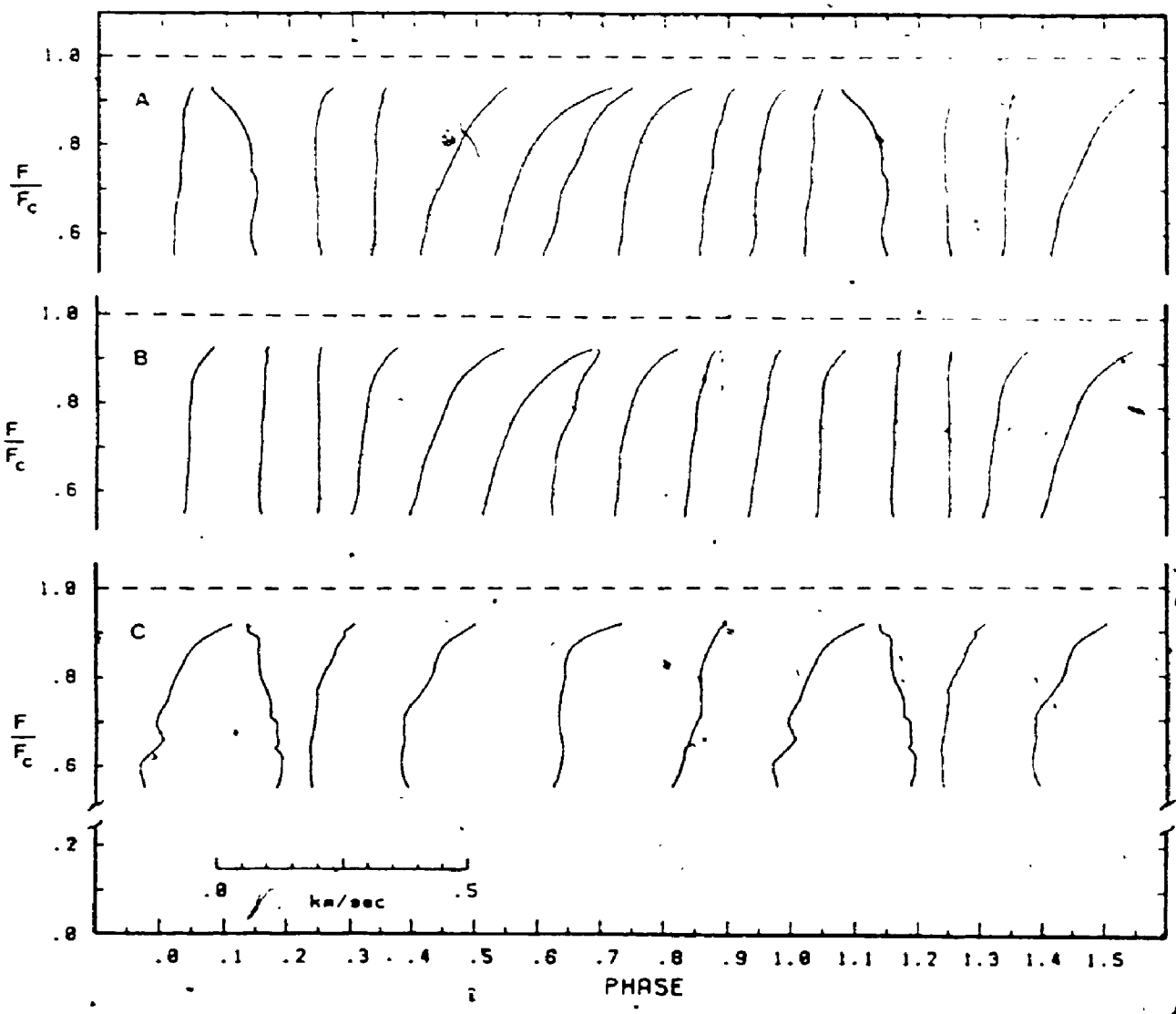

Figure 3.7 The phase diagram for the bisectors over one and a half cycles. The top two panels show the mean bisectors for the λ6250 region lines: (a) is for the 1986 season alone, and (b) is for the entire data set. At the bottom are the mean bisectors for the λ6150 region lines.

Table 3.2

The Spectral Lines

(λ6150 region)

λ (Å)	Ion	χ_l (eV)	RMT[a]	g^b_{eff}
6122.23	Ca I	1.89	3	1.75
6141.73	Ba II	0.70	2	1.10
6151.62	Fe I	2.18	62	1.83
6162.18	Ca I	1.90	3	1.25
6165.36	Fe I	4.14	1018	1.00
6166.44	Ca I	2.52	20	0.50
6173.34	Fe I	2.22	62	2.50
6175.37	Ni I	4.09	217	1.25

[a] from Moore et al. 1966

[b] from Beckers 1969

criteria as for the λ6250 region set, and their mean bisectors were calculated following the same procedure as before. For comparison with the λ6250 region bisectors, the mean bisectors from the λ6150 region lines are plotted along the bottom of Figure 3.7. The progression of bisector shapes seen here is consistent with those of the λ6250 region, even though the data are far fewer.

3.2.2 The Precision and Constancy of the Derived Periods

The precision of the period values was estimated by computing a series of velocity-span phase diagrams using different periods. The range in period which produces a noticeable deterioration in the phase diagram is taken as the error on the period. Figure 3.8 illustrates the process for the 1986 data alone. A period near ~ 6.40 days gives the best phase diagram and a significant deterioration is observed for periods deviating by more than ~ 0.08 days from this. The full data set, on the other hand, shows a 6.43 day period, with a range of only ~ 0.01 days. Figure 3.9 shows the phase diagram for the entire data set using a 6.43 day period.

Now, if we assume the period has remained constant, its precision, as determined from the full data set, compared to that determined from only one season, should approximately match the ratio of the time span used in each case. Here, this time ratio is ~ 8, so the full data set should yield a period ~ 8 times more precise than the 1986 season alone, and this is exactly what was found above. The period has therefore remained constant to within ~ 0.2% over the four

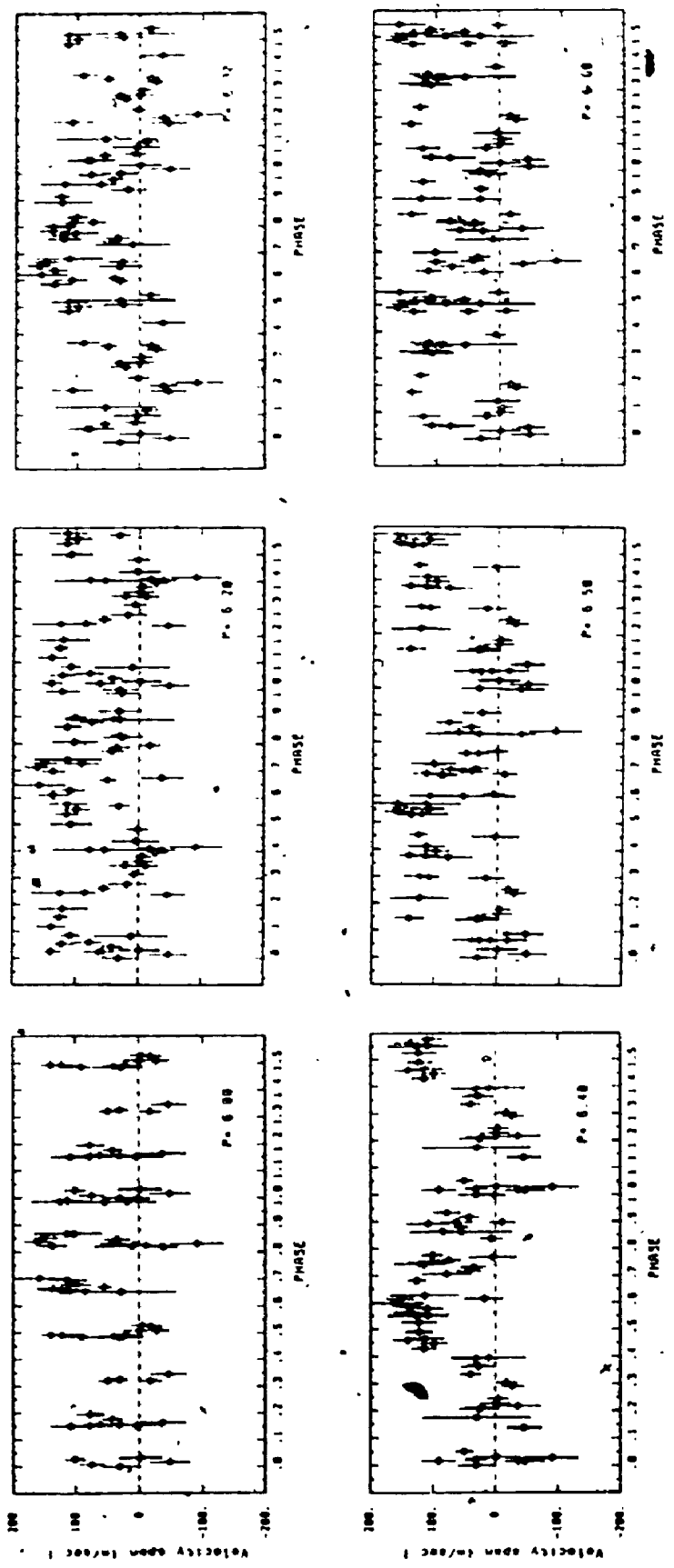

Figure 3.8 A series of phase diagrams for the 1986 velocity spans. The period used to generate each diagram is shown in the lower right corner. A period near ~ 6.40 days gives the best diagram. Noticeable deterioration of the phase diagram is seen for periods devlating by more than ~ 0.08 days from this.

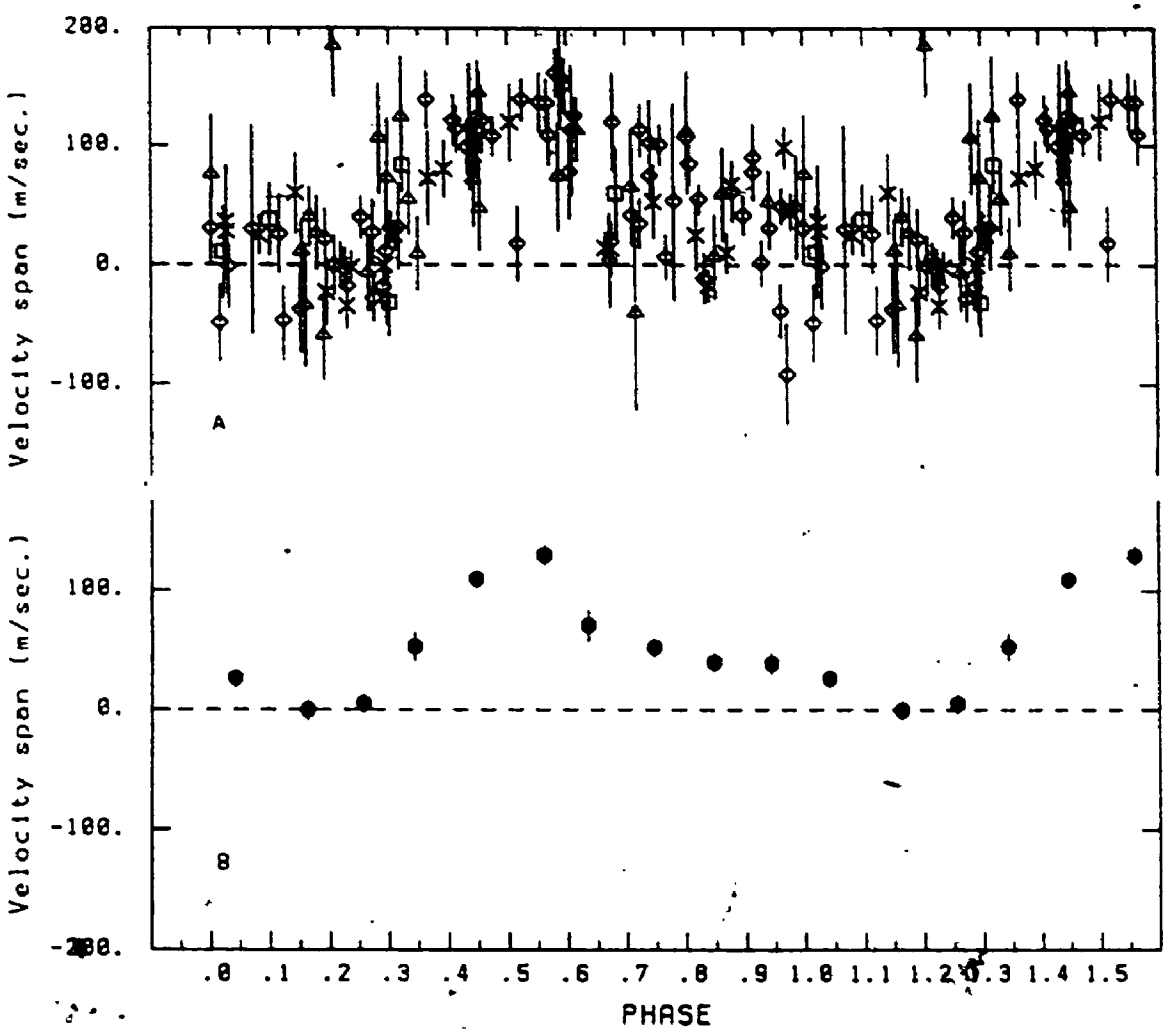

Figure 3.9 A phase diagram for the velocity spans of the entire data set over one and a half cycles. At the top are the individual measurements. Squares are for 1984, triangles for 1985, diamonds for 1986, and X's for 1987. The phase means are shown along the bottom.

seasons, and the variations have remained phase coherent. The stability of the period and phase rule out differential rotation and evolution of the proposed surface feature in longitude.

3.2.3 The Constancy of the Velocity-span Curve

Now the constancy of the amplitude, and shape, of the velocity-span curve is investigated. Because of incomplete phase coverage in all but the 1986 season, the data were divided into two groups. The 1984 and 1985 data were included in one group, and the 1986 and 1987 data in the other. Phase means were calculated for each group following the same procedure used earlier for the bisectors. The results are shown in Figure 3.10. The amplitude during 1984 and 1985 is marginally less than that seen in 1986 and 1987, but the difference is small, and well within the calculated errors. Similarly, any difference in shape is lost in the noise.

It would appear that the surface feature has remained nearly unchanged for the duration of this investigation.

3.2.4 Discussion of Errors on the Measured Velocity Spans

Gray (1983) has argued that the observed random bisector errors can be completely accounted for by considering only the photometric errors. His expression for the bisector error, $\delta\lambda_b$, arising from photometric noise is

$$\delta\lambda_b = \frac{1}{\sqrt{2}}\,\delta F/(dF/d\lambda) \qquad 3\text{-}2$$

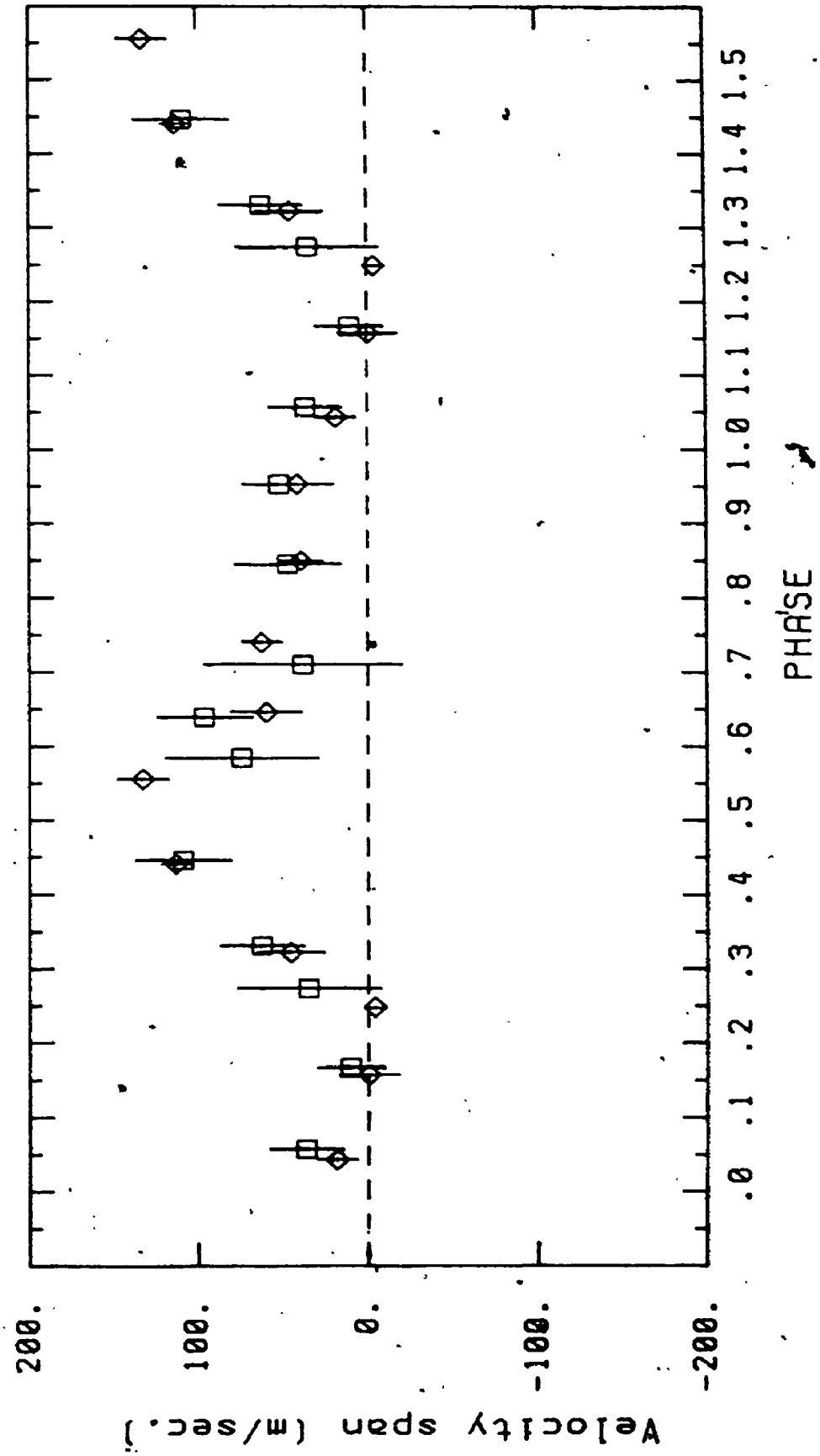

Figure 3.10 A phase diagram for the velocity spans. The data have been divided into two groups: the 1984 and 1985 data are included in one group (squares), and the 1986 and 1987 data in the other (diamonds). Within errors, both curves have the same amplitude and shape.

where, δF is the photometric error, and $dF/d\lambda$ is the slope of the profile in units of fraction of the continuum per km s^{-1}. We see that the bisector error is a function of depth along the bisector, with $\delta\lambda_b$ becoming large in the wings and in the core, as $dF/d\lambda$ becomes small. By averaging the bisectors from several lines, this error can be reduced. The error on the velocity span, δVS, is then given by

$$\delta VS = \sqrt{(\delta\lambda_b)_u^2 + (\delta\lambda_b)_l^2} \qquad 3\text{-}3 \ ,$$

where $(\delta\lambda_b)_u$ and $(\delta\lambda_b)_l$ are the velocity errors on the upper and lower bisector points used to calculate the velocity span. Since the bisectors entering the mean have a range of depths, $(\delta\lambda_b)_u$ and $(\delta\lambda_b)_l$ must be calculated explicitly.

The behavior of the velocity-span errors, as a function of signal-to-noise, has been investigated by generating a series of synthetic bisectors using the two-stream granulation model outlined in Gray and Toner (1985). (See also Chapter 4 and Toner 1984.) For the experiment being considered here the parameters listed in Table 3.3 are used:

Table 3.3

Parameters used to generate asymmetric profiles[2]

$v \sin i$	ζ	v_b	v_c	F_c/F_h
3.0 km s^{-1}	5.0 km s^{-1}	-1.4 km s^{-1}	4.0 km s^{-1}	0.15

[2]*See Chapter 4 for a definition of the parameters.*

The exact choice is not critical for the present situation as long as the observed profile shape is approximately reproduced. The disk integration was convolved with a variety of thermal profiles having equivalent widths ranging from 0.06 Å to 0.14 Å (to simulate the observed range). Bisectors, and their error functions, were calculated assuming different signal-to-noise ratios. The velocity span between 0.87 and 0.55 of the continuum, and its attendant error was determined for each line bisector, and also for means of four and eight bisectors. The bisectors entering the 8-line mean were calculated from profiles having approximately the same distribution of line strengths as in the observations. Figure 3.11 shows the results. We see that the predicted errors, for a mean S/N of ~ 300 to 400, and four to eight lines, fall in the range of ~ 18 to 30 m s^{-1}, in excellent agreement with the observed r.m.s. noise level estimated from the Fourier spectra (~ 20 - 25 m s^{-1}), and the calculated mean velocity error (30 ± 15 m s^{-1}). Therefore, the observed errors can be completely explained by photometric noise.

3.3 The Equivalent-width Variations

The relative temperature of the proposed feature was determined from small changes in the equivalent widths of some of the spectral lines (see Chapter 4). The most temperature sensitive lines in the λ6250 field are the V I lines, with an excitation potential of a few tenths of an electron volt. The strongest and least blended of these lines is λ6251.83. The equivalent width of λ6251.83 was divided into

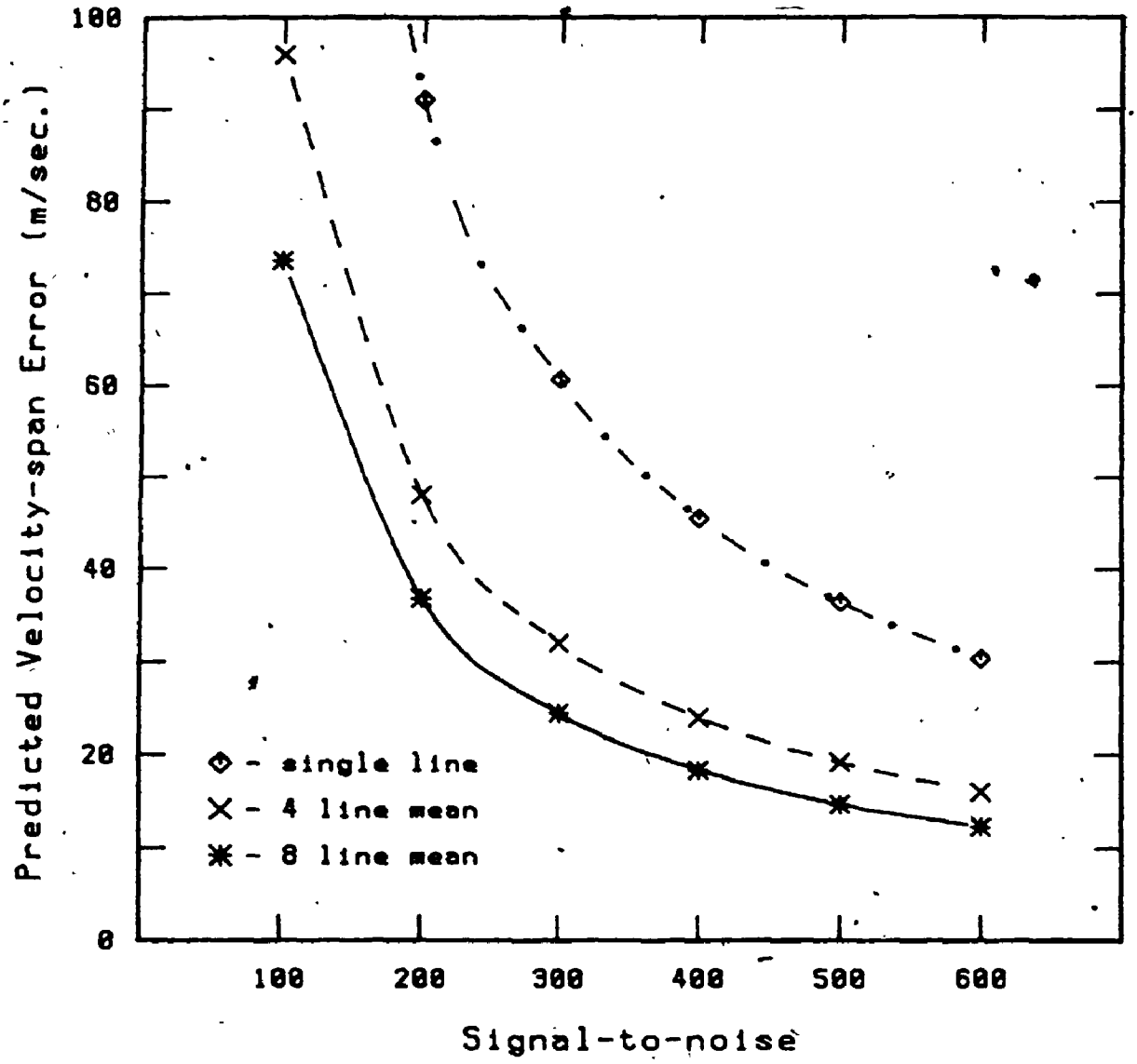

Figure 3.11 The predicted velocity-span errors as a function of signal-to-noise for three cases: a single line (diamonds), a mean of four lines (X's), and a mean of eight lines (asterisks). The errors were calculated as explained in the text.

that of the nearby Fe II line λ6247.56, which has a lower temperature sensitivity, but in the opposite sense. Minor blends were corrected for by using the opposite side of the profile as a guide. Consistency in the treatment of and discrimination against known blends ensures that the time variations should not be systematically affected.

Fourier analysis of the V I/Fe II equivalent-width ratios revealed a period of 6.47 days for the 1986 and 1987 seasons. No periodic variations above the noise were apparent for the other seasons. The precision on this period was determined following the same procedure described in section 3.2.2. Because these data have a somewhat lower S/N compared to the velocity spans, the precision of the period is also somewhat less. The error on the period is found to be ~ 0.10 days, making it effectively the same as the 6.43 day period found from the velocity span. The fact that the equivalent widths vary with the same period as the bisectors is completely consistent with the hypothesis of a surface feature carried across the disk by rotation.

A phase diagram of the V I/Fe II equivalent-width ratio for the 1986 season, expressed as a percentage of the mean, is given in the top panel of Figure 3.12. Below this is the mean curve, which was obtained as follows. The data were binned, as done previously for the bisectors and velocity spans, but because of the lower S/N in this case, the resulting curve was rather ragged and ill-defined. To smooth out the raggedness, and improve definition, a series of binned phase curves, using slightly different periods (ΔP = 0.02 days) was

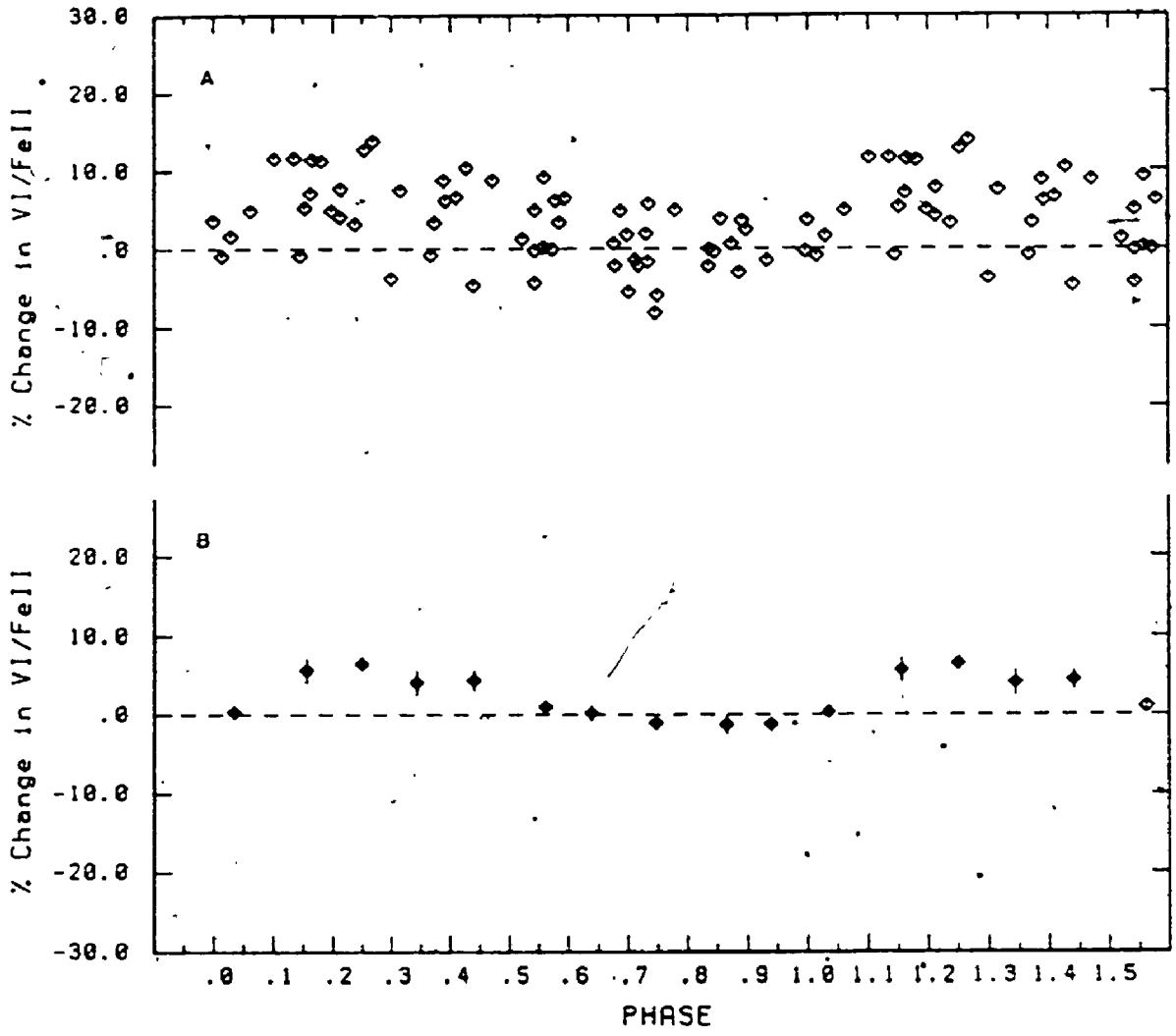

Figure 3.12 These phase diagrams show the V I/Fe II equivalent-width ratio for 1986, expressed as a percentage of the mean. The upper panel shows the individual measurements. The lower panel shows the mean curve, which was obtained as explained in the text.

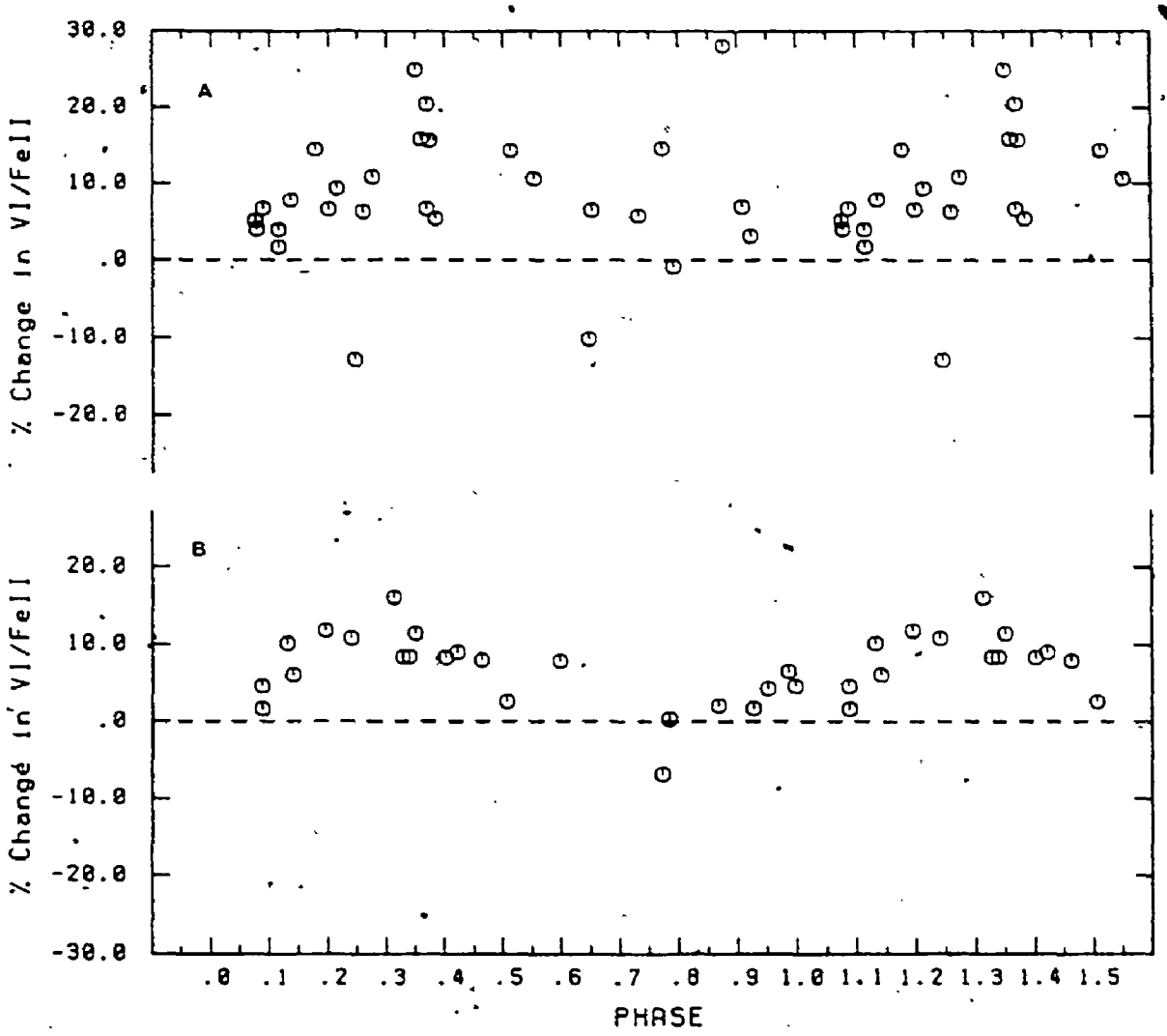

Figure 3.13 The V I/Fe II equivalent-width ratio variations for (a) 1985, and (b) 1987.

calculated, and then these were averaged together.[3] The important features to note are 1) the comparatively narrow peak and 2) the wide, flat minimum. The peak-to-peak amplitude of the variation is 7% ±1.5%.

The 1985 V I/Fe II equivalent-width ratios are presented in a phase diagram in Figure 3.13a. No variation is apparent above the noise, which is not surprising since these data are of poorer quality than the 1986 and 1987 data. The 1987 results (see Figure 3.13b) show a clear variation, which is in full agreement with those of 1986.

3.4 Magnetic Fields

As mentioned in Chapter 1, we might expect surface features on other stars to be magnetic phenomena, similar to sunspots. Under this assumption, we might expect to see variations in the deduced magnetic parameters as the feature is carried around the star by rotation. Indeed, some evidence for temporal variations of the Zeeman broadening for late-type stars has been found by Marcy (1984), Saar (1987a; 1987b), and Saar et al. (1987). Additional evidence that a magnetic field may be associated with the feature on ξ Boo A comes from modulations of the Ca H and K-line emission. Several investigators (e.g. Noyes et al. 1984; Baliunas et al. 1985) have used such

[3] By using a range of periods the data are rebinned slightly for each period value, thus smearing the individual data points over a finite phase interval.

measurements to estimate the rotational period of ξ Boo A, but the study which is of greatest use to us here, was published by Saar et al. (1987). These latter investigators obtained H and K measurements for ξ Boo A over a time span of ~ 30 days, beginning about June 1986. Figure 3.14 shows their H and K measurements, transformed to the epoch used in this study. The data for Figure 3.14 were taken from a phase diagram which was generated using a 6.2 day period. Since the time span covered by the data is small (only ~ 5 rotational cycles), the maximum phase error should be ~ 0.10 - 0.15 compared to the phases from a 6.43 day period. This might cause some distortion of the curve, but it will not destroy the variation. Indeed, a clear variation is seen, which is in phase with the equivalent-width changes presented earlier. Therefore, there is a strong expectation that the magnetic parameters for ξ Boo A will vary with time.

The problem of detecting magnetic fields was approached from three directions. Firstly, the residual Fourier transforms of the line profiles were compared, following the basic ideas outlined in Gray (1984a). The general method is as follows. The Fourier transforms for several lines are calculated and the thermal component of the line broadening is divided out of each transform. What remains is a combination of rotation, macroturbulence, and Zeeman broadening. The mean residual transform for the least magnetically sensitive lines is then used as a first guess for a line lacking all magnetic sensitivity, and this is divided out of the lines with high magnetic sensitivity. This yields a first approximation for the component of the broadening due to the Zeeman effect alone. The next step is to

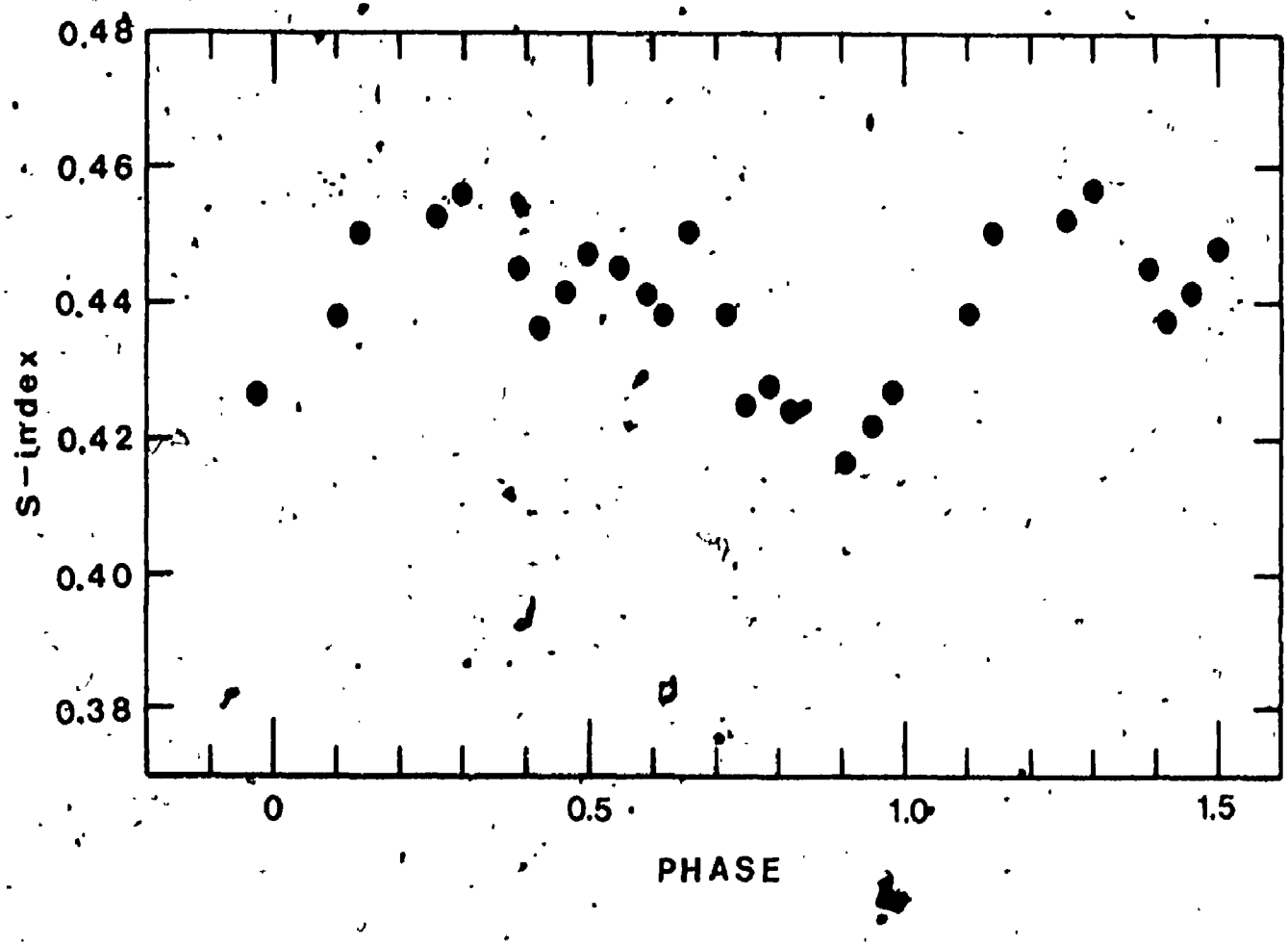

Figure 3.14 The Ca II H and K measurements of Saar et al. (1987) expressed in terms of the S-index. The measurements have been transformed to the epoch used in this study.

apply this as a correction to our first guess for the magnetically insensitive line above. The process is repeated until convergence is achieved. The exposures were analyzed individually and also grouped together by phase. In all cases no significant variations were found.

The second approach also made use of the Fourier transforms of the profiles, except that this time each line was considered separately. The transforms were calculated and the thermal broadening removed, as was done above. The process was repeated for the same line in each of the 1986 exposures, thus giving a time series of residual transforms. To improve the S/N, these were binned by phase, and means were calculated for each bin. To test for changes in the line broadening, a mean of all of the residual transforms was calculated and divided from each of the phase averaged residual transforms. An example is shown in Figure 3.15. Deviations about the line of Fourier amplitude equal to unity indicate changes in the line broadening. The noise dominated regime is clearly visible at the higher Fourier frequencies.

As a measure of the change in line broadening, the following integral was calculated for each residual transform (d(σ)),

$$\Delta LB = \int_{\sigma=0}^{0.05} (d(\sigma) - 1)\, d\sigma .$$

Values of ΔLB less than zero indicate that the line broadening is above the average, while values greater than zero indicate that the line broadening is below the average. ΔLB was calculated as a function of phase for the lines marked with a † in Table 3.1, and the resulting curves are plotted together in Figure 3.16. A small

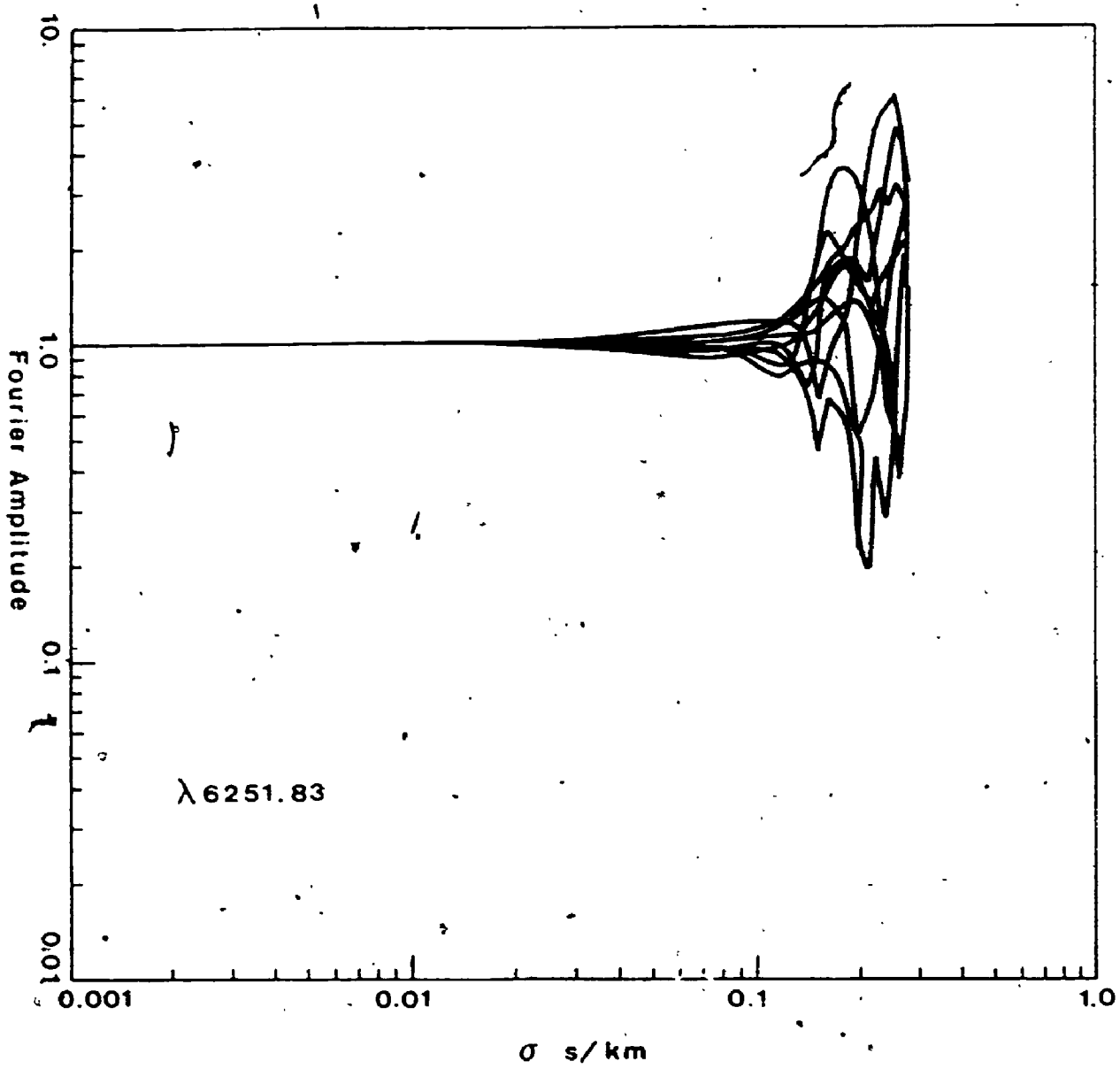

Figure 3.15 The residual transforms of λ6251.83 after division by the mean transform. Deviations from the line of unit Fourier amplitude indicate changes in the line broadening. The noise dominated regime is clearly visible at frequencies above ~ 0.1 s/km.

variation is apparent, which is in phase with the equivalent-width variations (refer to Figure 3.12). Now, if the observed changes in line broadening are due to variations in the Zeeman broadening, one would expect the amplitude of the individual ΔLB vs. phase curves to be proportional to the magnetic sensitivity of the line, i.e., the Landé-g value. Figure 3.17 shows the amplitude of each curve plotted against g_{eff}. There is no obvious correlation. Apparently the observed changes in line broadening do not result from magnetic fields, but they are consistent with an enhanced macrobroadening, as is used in Chapters 4 and 5.

The final approach for searching for magnetic effects makes use of the line bisectors themselves. Assuming that the observed bisector modulation stems from a magnetic feature, we would expect the amplitude of the bisector variations to be a function of the magnetic sensitivity of the spectral lines. The lines were therefore divided into two groups by their effective Landé-g value. This gives four lines in each group, with the low magnetic sensitivity lines having a mean $g_{eff} \cong 1.0$, and the high magnetic sensitivity lines having a mean $g_{eff} \cong 1.7$. Mean bisectors for both sets of lines were constructed for the four seasons, and the velocity spans were calculated. Phase averaged plots of the velocity spans from the high g_{eff} and low g_{eff} lines are shown in Figure 3.18. The amplitudes are sensibly the same. Again, there is no evidence for a magnetic field associated with the surface feature on ξ Boo A.

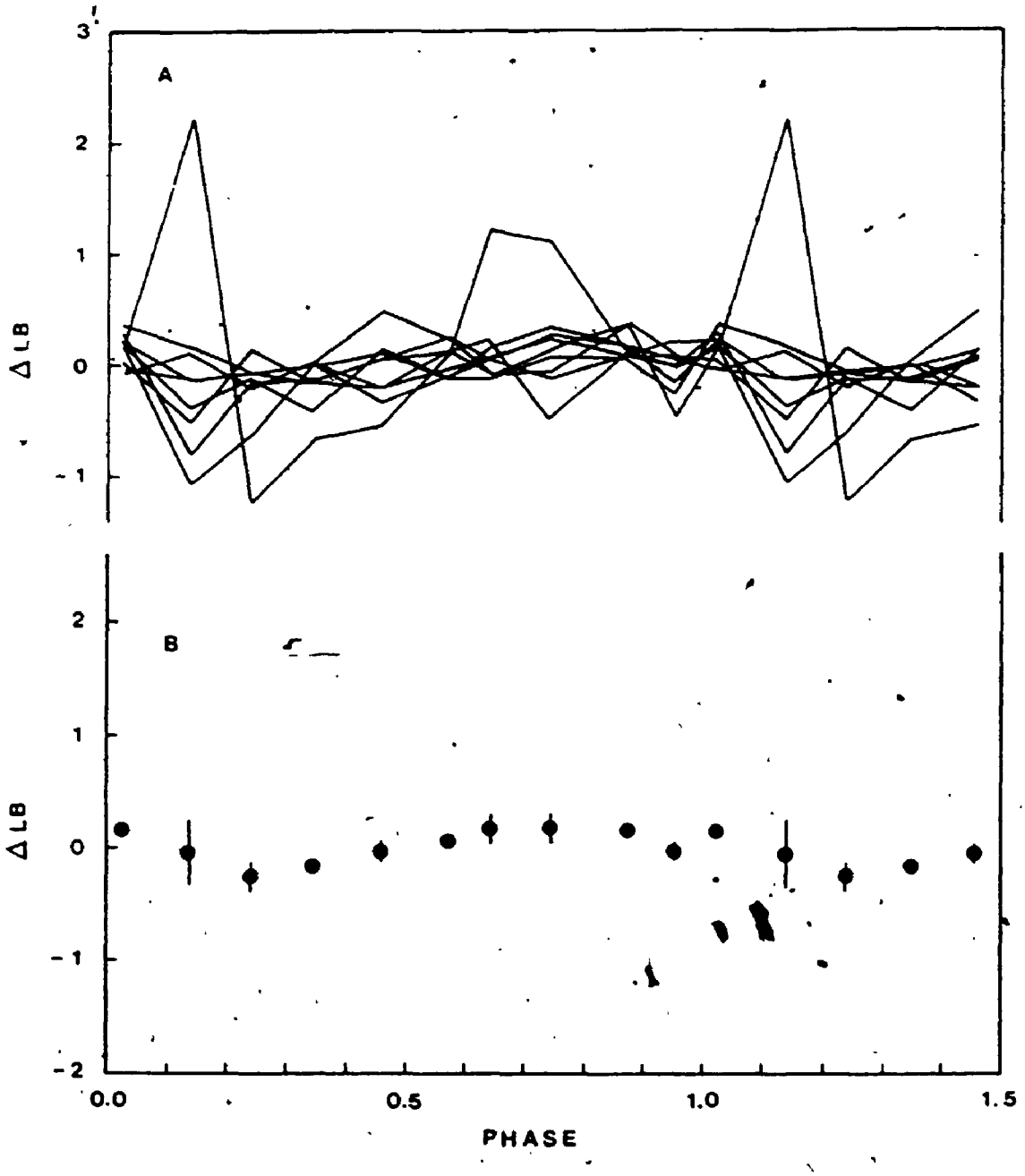

Figure 3.16 ΔLB is plotted here against phase. Along the top are the curves for several different spectral lines. The bottom curve is a weighted mean. Values below zero indicate that the line broadening is above the average, while values greater than zero indicate that the line broadening is below the average.

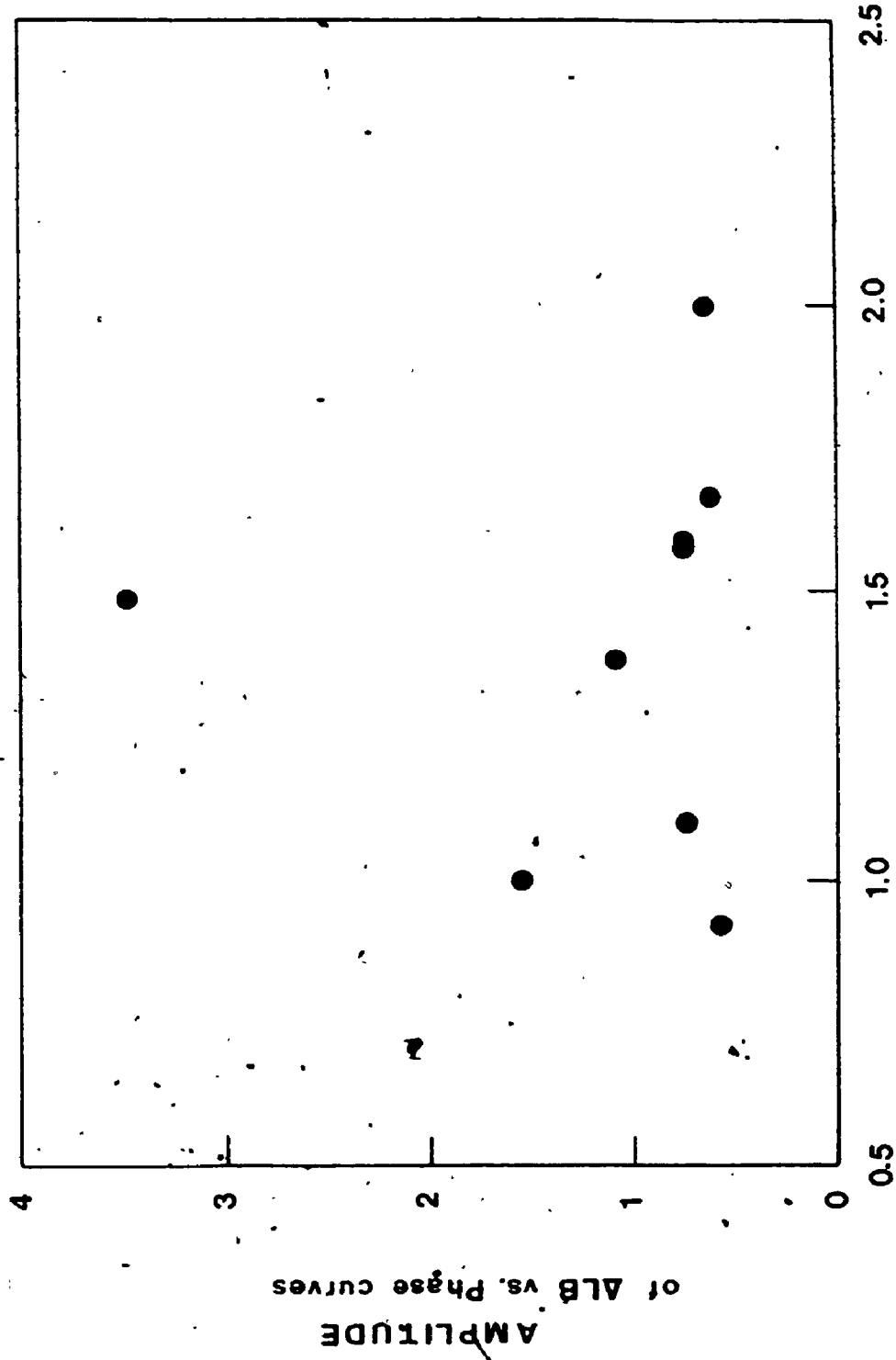

Figure 3.17 The amplitude of the individual ΔLB vs. Phase curves from Figure 3.16a is plotted here against Landé-g. There is no obvious correlation.

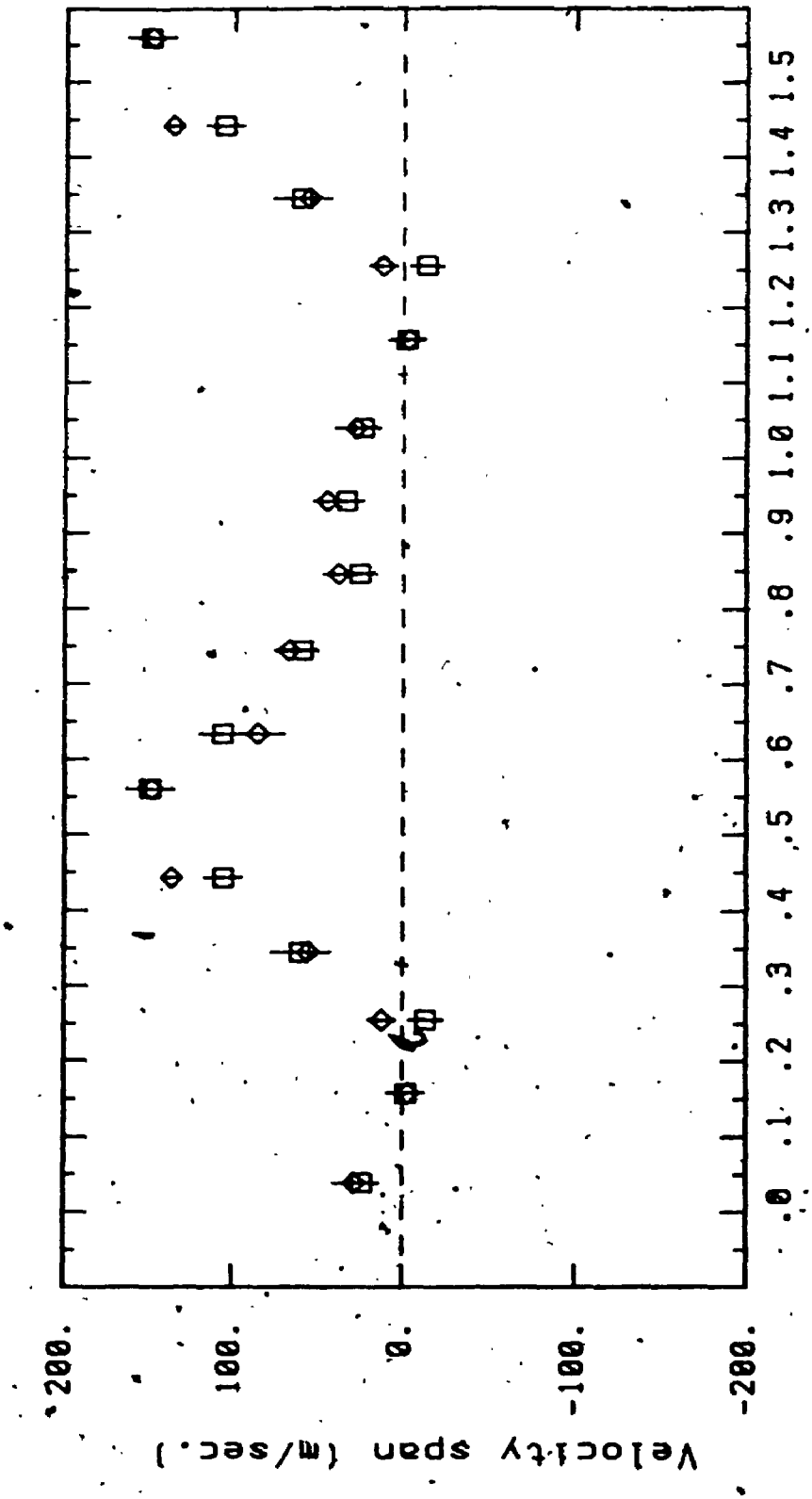

Figure 3.18 High g_{eff} lines (squares) are compared to low g_{eff} lines (diamonds) in this phase diagram. The amplitude for both sets of lines is sensibly the same.

CHAPTER 4

A Numerical Simulation

4.1 Introduction

When we examine the observed line bisectors in Figure 3.7, we see that they oscillate around a mean which resembles that found by Gray (1982) for late G dwarfs. In this earlier work (and others; see Chapter 1), the line asymmetry has been interpreted in terms of granular flows. Therefore, it is logical to postulate that the same process is operating in this case; and to assume that, basically, the entire stellar surface is covered by a solar-like granulation pattern. This results in a line asymmetry characteristic of the global granulation properties. The observed variations are then viewed as a perturbation on the basic granulation signature, caused by the presence of an active patch.

The characteristics attributed to the patch represent a mixture of assumptions and deductions. Naturally uniqueness under such a situation cannot be established, but at this time there seems no better path to follow. Numerical experiment is used extensively to establish the importance of each of the variables. The final model is self-consistent, and is found to be very successful at explaining both the observed line bisector and line strength variations for ξ Boo A (see Chapter 5). The model gives the size and position of the region responsible for the observed variations, as well as information on conditions within the region. No attempt is made to explain the

physical origin of the patch.

4.2 The Model

4.2.1 The Bisectors

Following Gray and Toner (1985), a simple two-stream granulation simulation is used as the basic model (see also Toner 1984). This model has hot material with an average velocity of rise, v_h, and cold material with an average velocity of fall, v_c. Placed around each stream velocity is a Gaussian velocity distribution with dispersion ζ. The relative strength of the two streams is specified by F_c/F_h (representing the relative contributions to the continuum flux). To incorporate rotation (and its interaction with the velocity distributions), integration over the apparent disk of the star must be performed.

A unit circle represents the apparent stellar disk. It is divided into many small areas of approximately equal radial and azimuthal dimension, as shown in Figure 4.1. Typically, the radial step size is set to 0.05, leading to 1252 small areas. The velocity distribution given in equation 4-1 below is placed at the center of each area. This distribution represents the simplified two-stream picture of the granular flow pattern, mentioned above.

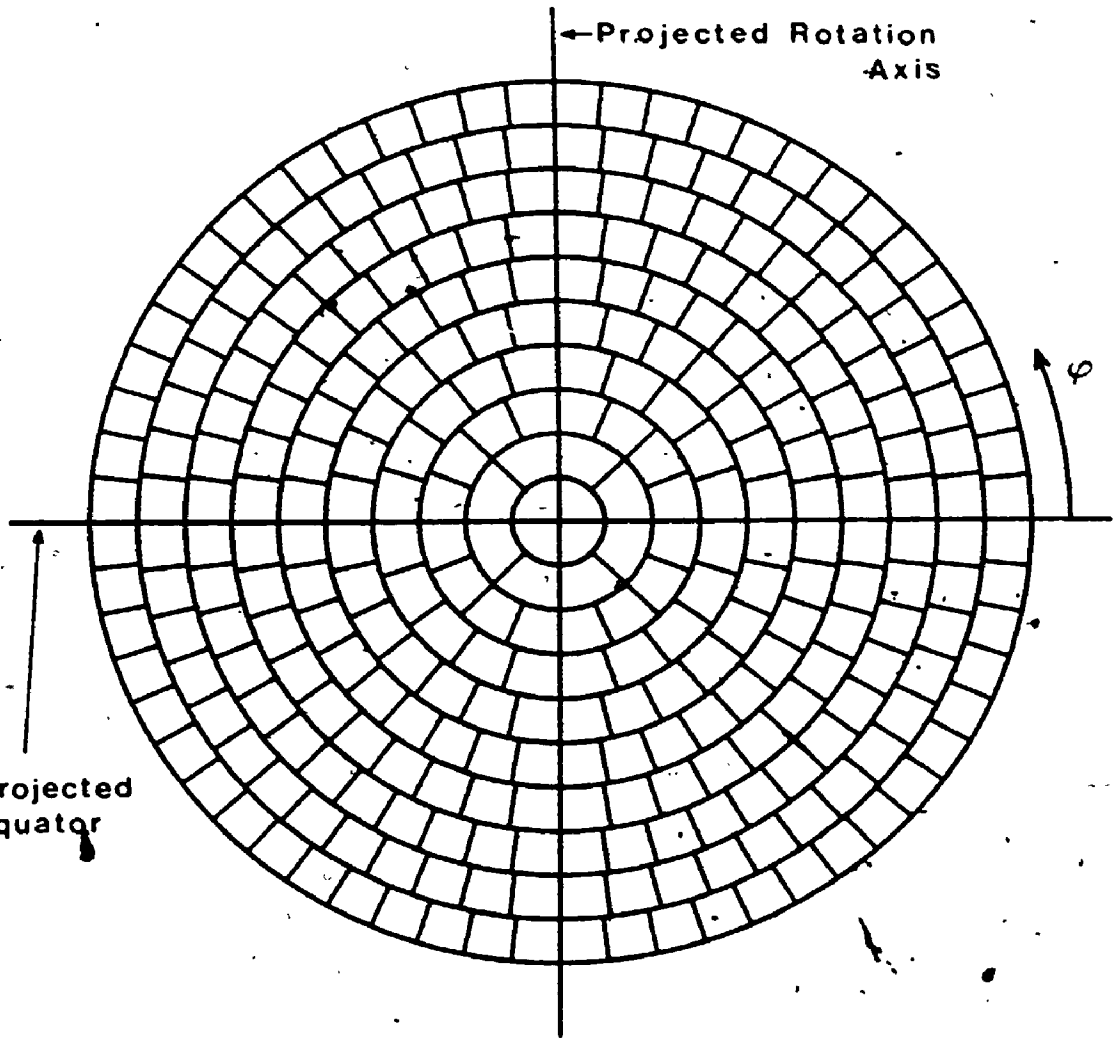

Figure 4.1 - The apparent disk of the star is divided into many small areas of approximately equal radial and azimuthal dimension. In this example a radial step size of 0.10 has been used, leading to 312 areas. The disk integration is obtained by adding together the velocity distributions at the center of each small-area.

$$\Theta(\Delta\lambda) = \frac{1.0}{\sqrt{\pi}\ \zeta\ \cos\theta}\, e^{-\left(\frac{\Delta\lambda - \varpi_h \cos\theta}{\zeta\ \cos\theta}\right)^2} + \frac{(F_c/F_h)}{\sqrt{\pi}\ \zeta\ \cos\theta}\, e^{-\left(\frac{\Delta\lambda - \varpi_c \cos\theta}{\zeta\ \cos\theta}\right)^2} \qquad 4\text{-}1$$

For each small area on the model star's disk, the Gaussians at ϖ_h and ϖ_c are projected onto the line of sight, as are ϖ_h and ϖ_c themselves (through cos θ, where θ is the angle between the normal to the small area and the line of sight). The distributions are shifted by the rotational Doppler shift appropriate to the small area's position on the disk (through $\Delta\lambda$, where $\Delta\lambda = \lambda - (r\ \varpi \sin i \cos\phi)$; and r is the fractional radius of the area's position, ϕ is the azimuthal angle with zero at the projected equator, and $\varpi \sin i$ is the projected rotation velocity). After weighting by the limb darkening, the contributions from the small areas are summed. A standard limb darkening law,

$$1 - \epsilon + \epsilon \cos\theta\ ,$$

is used, with $\epsilon = 0.6$. The disk integration is then convolved with a specific intensity profile computed at disk center in order to approximately allow for the smearing by the thermal profile.

The basic granulation model is now modified slightly by placing a patch onto the surface of the model star. Because of the low rotational values typical of most late-type dwarfs (~ <5.0 km s^{-1}; Smith 1979; Soderblom 1982; Gray 1984b), we cannot hope to obtain any

great spatial resolution. Therefore, it is assumed that there is only one patch, and that it is circular in shape. The center of the patch is located at the position defined by the patch latitude and the phase angle. Zero phase is defined to be when the patch transits, with the phase increasing in the direction of rotation.

If we consider the reference frame in which the patch is located at the center the disk, its projection will be a circle of radius

$$R_{patch} = \sqrt{A} \quad ,$$

where A is the fractional area covered by the patch. As we integrate over the apparent disk, we must test to see if the small area under consideration (see above) is within the boundary of the patch. If this condition is met, equation 4-1 must be modified to reflect the conditions within the patch. In Section 4.2.2 the results of a series of numerical experiments are presented, which establish the important characteristics of the patch.

In the observer's reference frame the coordinates of the small area are given by:

$$x_o = r \cos \phi$$

$$y_o = r \sin \phi$$

$$z_o = \cos \theta$$

These are now transformed to the patch's reference frame following three simple steps:

1) rotate around the x-axis by the star's inclination (i):

$$x_1 = x_o$$

$$y_1 = y \cos i + z \sin i$$

$$z_1 = z \cos i - y \sin i$$

2) rotate around the y_1-axis by the phase angle (ψ):

$$x_2 = x_1 \cos \psi + z_1 \sin \psi$$

$$y_2 = y_1$$

$$z_2 = z_1 \cos \psi - x_1 \sin \psi$$

and finally,

3) rotate back around the x_2-axis by the patch latitude (ℓ):

$$x_p = x_2$$

$$y_p = y_2 \cos (-\ell) + z_2 \sin (-\ell)$$

$$z_p = z_2 \cos (-\ell) - y_2 \sin (-\ell).$$

If $\sqrt{x_p^2 + y_p^2} \leq R_{patch}$, the small area is within the patch boundary.

When computing a phase series, calculations are performed at ten phases within the rotational cycle. For the experiments presented below (Section 4.2.2) the phases are chosen to be equally spaced. A typical calculation of a single phase series requires approximately one minute of CPU time on a VAX 8600, and ~ 45 - 50 minutes on an IBM compatible (with a numeric coprocessor). Most of the calculations are done on either a Compaq *Portable II*, or a *Hyperion* microcomputer.

The bisector is calculated for each of the modeled profiles, and the span is obtained. Since the modeled bisectors tend to show a small redward curvature near the line core (see Figure 4.2), the span is computed between $F/F_c = 0.60$ and 0.87 rather than the 0.55 and 0.87 values used with the observations. This puts the lower bisector point above most of the redward curvature. The resulting systematic

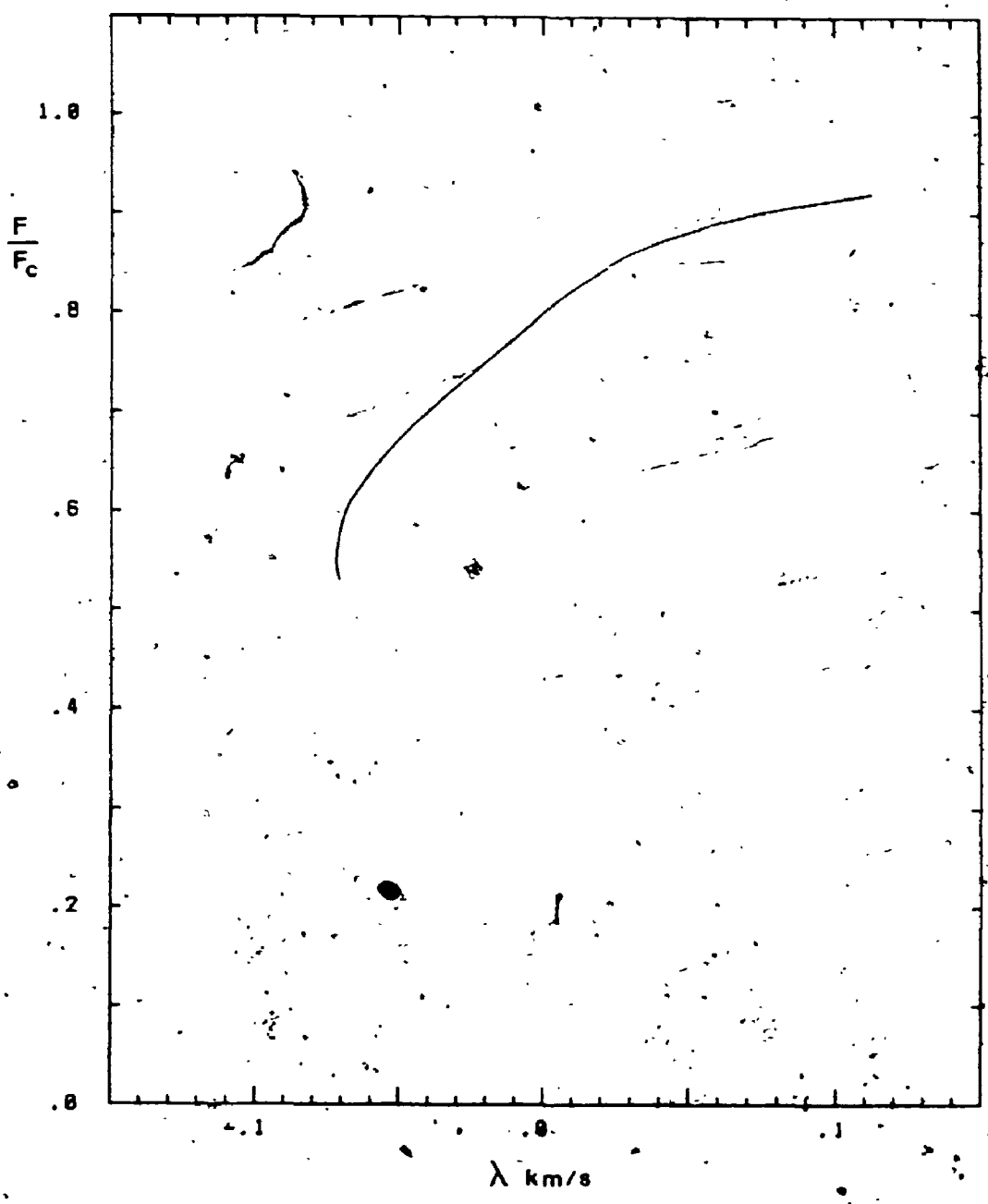

Figure 4.2 The synthesized bisectors tend to show a small redward curvature near the bottom as shown in this example. The velocity span is calculated between F/F_c = 0.60 and 0.87, thus putting the lower point above most of the redward curvature.

difference in velocity span is less than 10 m s^{-1}, and is negligible compared to the errors and uncertainties.

4.2.2 Characteristics Assigned to the Patch

The most logical approach to determining the characteristics to be assigned to the patch is to try to use our knowledge of surface features on the sun. However, this tack fails almost immediately. Solar surface features (e.g. sunspots and plage) are essentially magnetic phenomena, and we saw in the last chapter that the patch on ξ Boo A shows no evidence for being magnetic in nature. We have no recourse then but to look for guidance from other quarters.

In the literature there are numerous accounts of what are usually called starspots (see Chapter 1). While little is known concerning the conditions within these spots, there is one feature that is generally agreed upon — the spots are dark. If we assume the same to be true of the patch on ξ Boo A, can the darkness alone reproduce the observed bisector variations? To answer this, the following experiment was conducted.

A patch covering 10% of the visible disk is placed onto the surface of the model star. The brightness assigned to the patch is kept consistent with the typical photometric variations found for late-type dwarfs, ~ 0.01 - 0.02 magnitudes (Jerzykiewicz and Serkowski 1966). A relative brightness of 0.90 is used, leading to Δm_v of ~ 0.014 magnitudes. The values assigned to the remaining variables are listed in Table 4.1. Equation 4.1 is used within the patch area,

Table 4.1

The Basic Model Parameters

$\omega \sin i = 3.0$ km s^{-1}	$\omega_h = 4.0$ km s^{-1}
$\zeta = 5.0$ km s^{-1}	$\omega_c = -1.4$ km s^{-1}
$A = 0.10$	$F_c/F_h = 0.10$
$\ell = 55°$	$\zeta_p = 5.0$ km s^{-1}
$i = 40°$	$I/I_o = 0.85$

Unless otherwise stated in the text, the model parameters were set to the values listed in this table.

except that its contribution to the sum is reduced by the relative brightness assigned to the patch. Calculations are performed for ten equally spaced phases. The resulting velocity-span phase diagram is shown in Figure 4.3. We see that the computed bisector variations are a full order of magnitude smaller than the observed ones (compare with Figures 3.8 and 3.9). Therefore, simply reducing the brightness of the patch is completely inadequate.

Our original expectation in Chapter 1 was that granulation would be modified within an active (i.e. magnetic) region. So, even though there is no evidence for a magnetic field associated with the patch on ξ Boo A, let us now investigate the effect of changing the patch's granulation parameters. Figure 4.4 shows the modeled velocity spans when the granulation velocities, v_h and v_c, and the granulation contrast, F_c/F_h, are scaled relative to their values in the surrounding photosphere. We see that the variations produced by modifying the patch granulation are, once again, considerably smaller than the observed variations.

Where do we go from here? Recall that in section 3.4 we found that the observed line broadening varies along with the bisectors and equivalent widths. So, lacking any Zeeman broadening, we now try changing the macroturbulence within the patch, ζ_p, and see what the results are. Figure 4.5 shows the effect of using different values of ζ_p. We see that the macroturbulence within the patch has a very pronounced effect on both the shape and the amplitude of the computed velocity span curve — changing the dispersion, from reduced to enhanced, completely reverses the sense of the asymmetry variations.

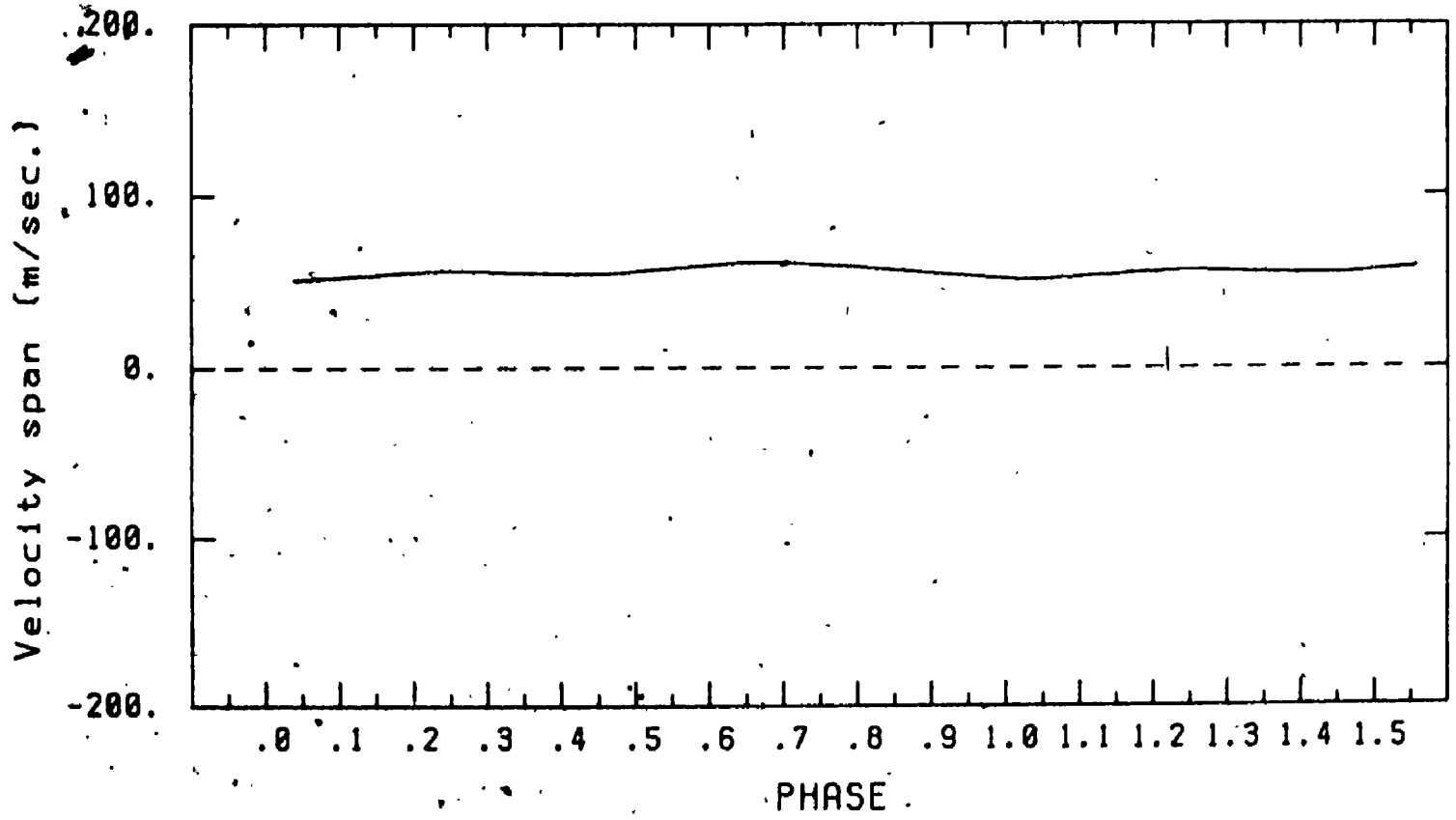

Figure 4.3 The synthesized velocity span phase diagram assuming only that the patch is darker than its surroundings. A patch size of 10% of the apparent disk, and a relative brightness of 0.90 were used for the calculation. We see that the amplitude of the curve is a full order of magnitude smaller than the amplitude of the observed one.

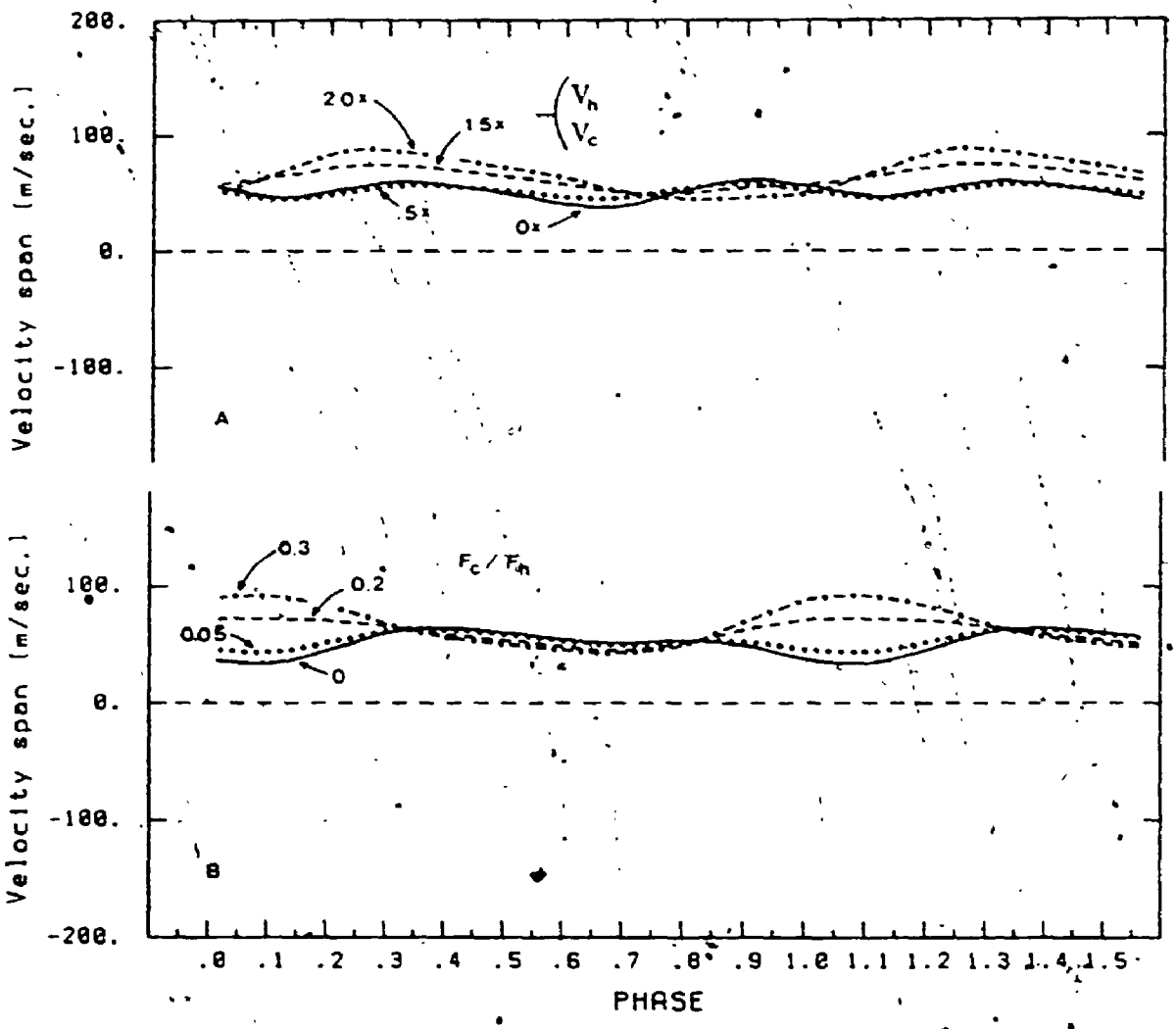

Figure 4.4 The effect of scaling the patch's granulation parameters relative to their photospheric values. In (a) v_h, v_c are scaled, and in (b) F_c/F_{ph} is scaled. We see that changing the granulation alone cannot explain the observations. (The parameter values are as labeled.)

Note that only an enhanced velocity dispersion reproduces the same type of asymmetry variations found in the observations (compare to Figures 3.8 and 3.9). Because the velocity dispersion produces such large effects, it will be called a "primary" variable.

Similar experiments reveal that the patch area, and the latitude of the patch, also have significant effects on the shape and amplitude of the velocity-span curve (see Figure 4.6). We can thus divide the model variables into two groups: 1) the primary variables ζ_p, A, and ℓ, and 2) the secondary variables v_b, v_c, and F_c/F_h. The complexity of the problem is reduced by ignoring the influence of the secondary variables, and concentrating only on fitting the primary variables. By searching parameter space, we can optimize these, and find the domain which best reproduces the observations.

It must be kept in mind however, that although it is true that the relative brightness of the patch has very little direct affect on the bisectors themselves, it is intimately tied to the patch area through the V I/Fe II equivalent-width ratio variations; and so fixing the patch area will automatically determine the patch brightness.

4.2.3 The Patch Brightness and Temperature

The V I/Fe II equivalent-width variations (see section 3.3) are used to estimate the temperature and brightness differences of the patch compared to the rest of the photosphere. V I is quite sensitive to even small temperature changes, with its strength increasing with decreasing temperature. Fe II is less temperature sensitive, but its

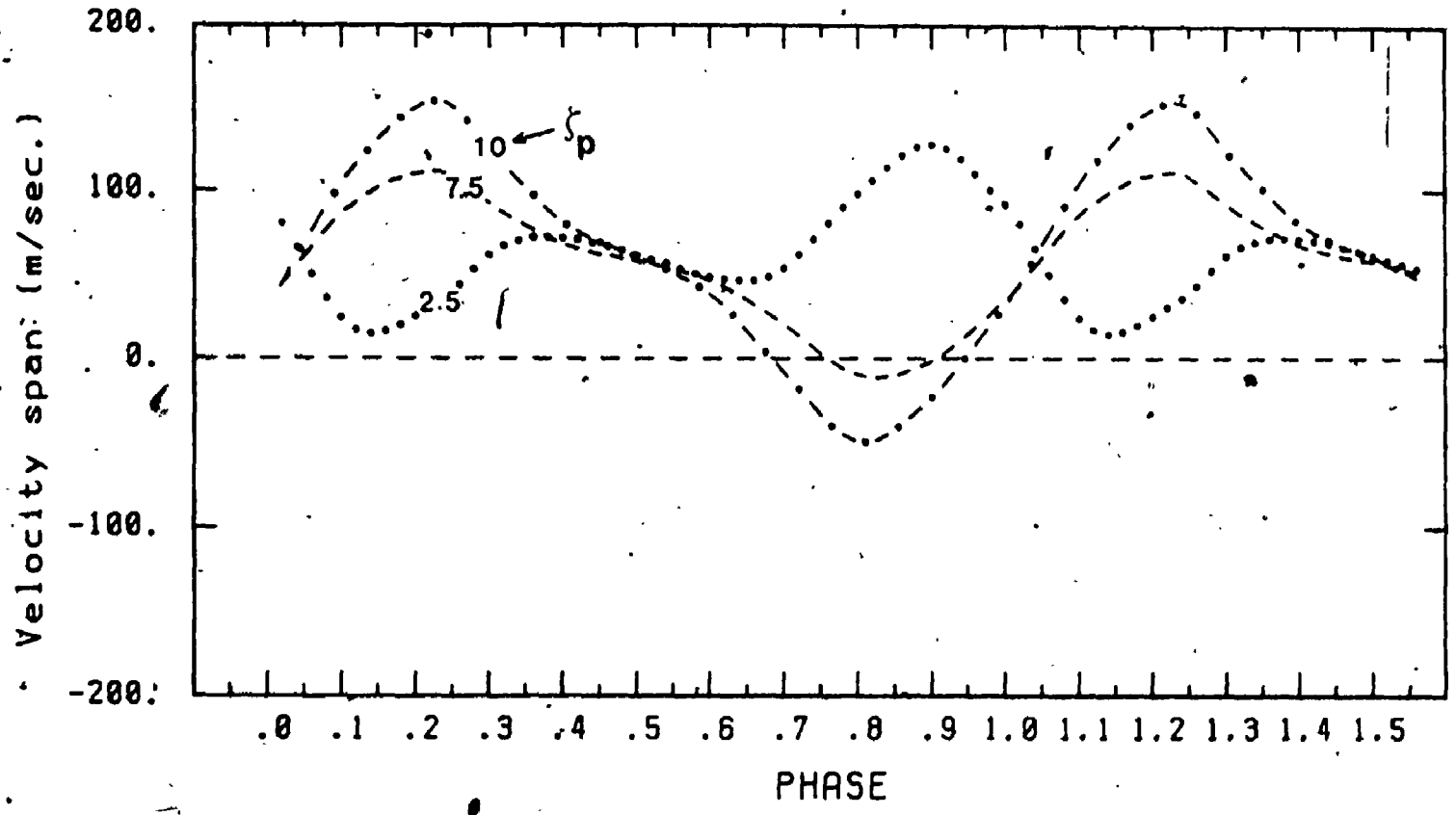

Figure 4.5 The effect of the patch's velocity dispersion on the numerical simulation is shown. Changing ζ_p completely changes the sense of the asymmetry variations. Only an <u>enhanced</u> velocity dispersion reproduces the same type of asymmetry variations found in the observations.

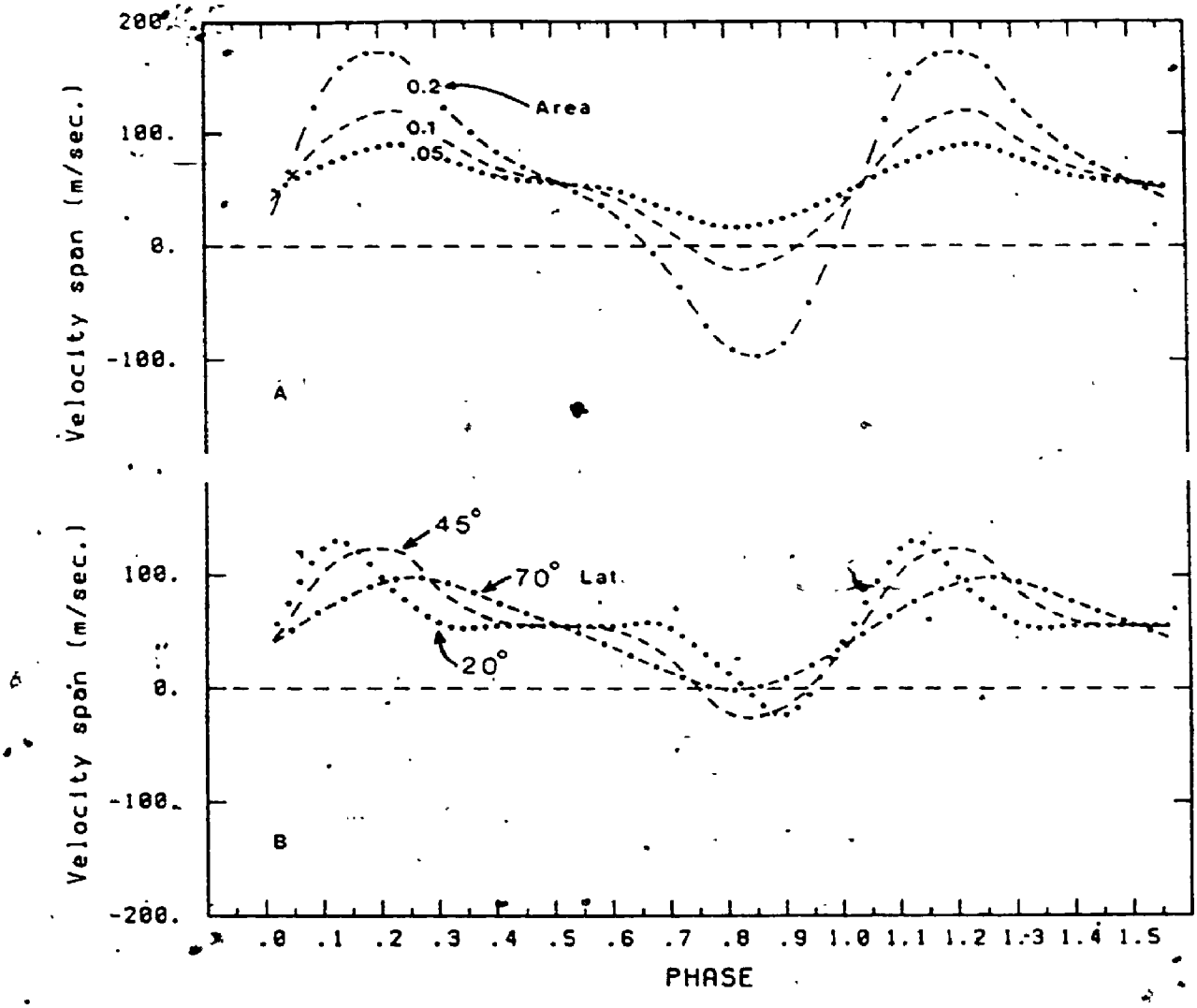

Figure 4.6 The effects of the remaining primary variables. The area of the patch controls the amplitude of the curve (A), and the patch latitude determines the extent of the flat portion of the curve (B).

strength decreases with decreasing temperature. Therefore, if we are dealing with a cool, dark patch, we would expect the ratio of the V I to Fe II equivalent widths to reach a maximum when the patch presents its greatest area. If the patch is warm and bright, the V I/Fe II ratio will reach a minimum at this point.

The necessary calculations for this step of the modeling were performed by D.F. Gray. His basic procedure is as follows. A series of model photospheres are computed for a grid of temperatures, and the flux within the computed line profiles is altered by replacing the specific intensity over the area of the patch with the specific intensity for the hotter or cooler model photosphere. The observed amplitude of the V I/Fe II equivalent-width ratio variation constrains the possible temperature (and hence brightness) of the patch, given its size. The relation found by Gray for ξ Boo A will be presented in the next chapter.

CHAPTER 5

Modeling the Patch on ξ Boo A

5.1 The Basic Solution

The first step in the modeling procedure is to determine the global granulation parameters: v_h, v_c, and F_c/F_h. This means that we must find the observational phase over which the patch is behind the star. We have seen from the experiments presented previously (see also Appendix 2), that as the patch passes around the far side of the star, the bisector remains nearly constant, and the velocity-span phase curve is almost flat. Referring back to Figures 3.7 and 3.9 we see that this occurs in the observations over the phase range - 0.8 to - 0.9. Therefore, the mean bisector over this phase interval is used to deduce the basic granulation parameters for ξ Boo A. Since the most complete phase coverage was obtained for 1986, modeling is restricted to observations obtained during this season.

The major line broadeners, i.e. the rotation ($v \sin i$) and the macroturbulent dispersion (ζ), are chosen to be consistent with the observed line broadening (Soderblom 1982, Gray 1984b). The values: $v \sin i$ = 3.0 km s^{-1} and ζ = 5.0 km s^{-1} are used. A grid of disk integrations with a range of v_h, v_c, and F_c/F_h is calculated, and the bisectors are computed. The observed mean bisector over the phase interval 0.8 to 0.9 is compared to this grid of synthesized bisectors, and the best match found. There is some degree of nonuniqueness in

this process (see for example Gray and Toner 1985), and the center of the domain of nonuniqueness is adopted as the combination most likely to be correct. The result, v_h = -1.4 km s^{-1}, v_c = 4.0 km s^{-1}, and F_c/F_h = 0.10, reproduces the observed bisector shape rather well (Figure 5.1).

We are now in a position to begin modeling the bisector variations. It is assumed that the rotation axis of ξ Boo A is perpendicular to the orbital plane. This sets the inclination to our line of sight at 40°. It is also assumed that the patch is darker than its surroundings.[1] The velocity span is used as the diagnostic to compare the model with the observations.

The phase relationship between the observed bisector variations and the modeled ones is determined by comparing the observed velocity-span curve with synthesized ones. The relation is found to be weakly dependent on the model parameters used to generate the synthesized curves, in the sense that different combinations of patch area, latitude, and velocity dispersion, are found to introduce small phase shifts between the calculated curves. For this reason, a small grid

[1]*Photometry of ξ Boo for 1986 and 1987, kindly provided by W. Lockwood (private communication), confirm that the patch is indeed dark. The photometry clearly shows the same 6.43 day period found for the line asymmetry and line strength variations. The brightness is found to vary inversely as the V I/Fe II equivalent width ratio, and specifically, minimum light occurs at the same phase as maximum V I/Fe II ratio.*

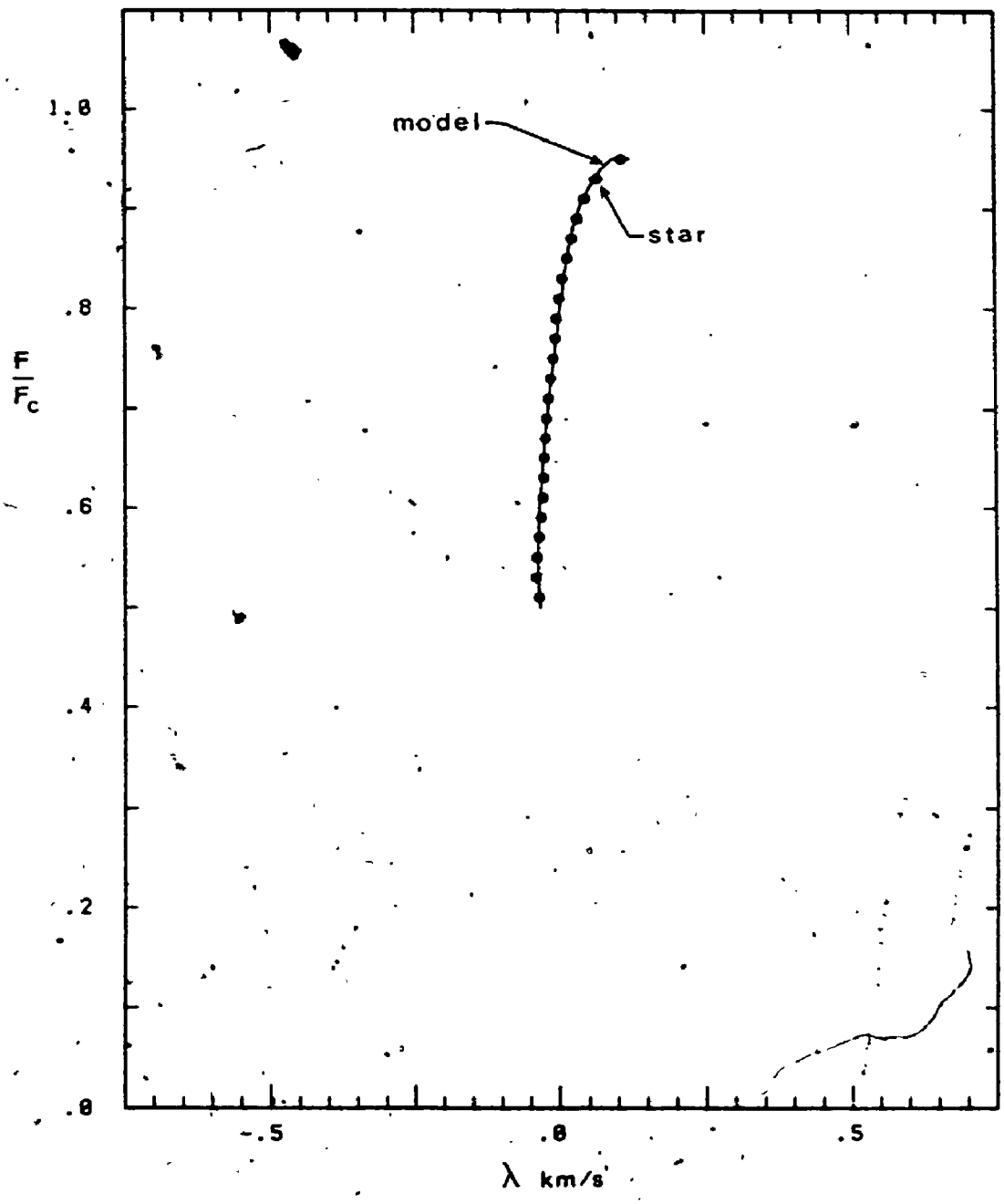

Figure 5.1 The synthesized line bisector (solid line) is compared to the mean observed bisector (circles) from the phase range 0.8 to 0.9. The granulation parameters are: $v_h = -1.4$; $v_c = 4.0$, and $F_c/F_h = 0.10$.

of synthetic velocity-span curves, which approximately reproduce the shape of the observed curve, is generated, and the mean phase relation is determined through comparison with this grid. Phase errors of ~ 0.01 may exist because of this effect, but considering the approximate nature of the calculations, this is not a significant source of error. The observed phases and the corresponding model phases are listed in Table 5.1.

The patch modeling now proceeds in a trial and error fashion. An initial set of patch parameters is chosen. The selection is guided by the experience gained during the model development and experimentation stage of the project. Only the primary variables, patch area, latitude, and velocity dispersion, are adjusted in the modeling process. Calculations are performed for the ten phases listed in Table 5.1. The bisectors are calculated, and their spans determined. The computed velocity-span phase curve is then compared to the observed one, and a reduced χ^2 measure of the goodness of fit is calculated. A value of χ^2 near unity means an excellent fit, while larger χ^2 values indicate poorer agreement. Contours of χ^2 are used to establish the domain of the optimum values of the parameters.

Initially, the patch is assumed to have no brightness difference compared to the surrounding photosphere. A trial patch size is chosen, and a series of calculations are performed for a range of latitude and velocity dispersion. Since the calculations are very computer intensive, a relatively coarse grid in the ζ - latitude plane is used initially. The grid spacing is 0.5 km s^{-1} in ζ, and 5° in latitude, which allows the approximate domain of best fit to be found.

Table 5.1

The Mean Relation Between the Observational Phase and the Model Phase

Observational Phase	Model Phase
0.03	0.69
0.14	0.80
0.24	0.90
0.34	0.00
0.46	0.12
0.57	0.23
0.66	0.32
0.75	0.41
0.87	0.53
0.95	0.61

Additional calculations are then performed in this region of the ζ - latitude plane using a finer grid spacing, and the χ^2 contours are found by interpolation.

Contours of best fit are found for a range of assumed fractional disk area. For the first cycle, a fairly coarse grid of patch areas is used (A=0.06[2], 0.10, 0.15, 0.20, 0.25). Of this sample, only the A = 0.10 patch size yields χ^2 values near unity. This rough estimate for the patch area is used in the next leg of the modeling process.

As explained in section 4.2.3, the observed variation of the V I/Fe II equivalent-width ratio is used to constrain the brightness of the patch, given its size. Figure 5.2 shows the possible brightness contrast for the patch as a function of patch size, assuming the 7% V I/Fe II equivalent-width ratio variation found in section 3.3. A brightness contrast of ~ 0.85 is indicated, given the patch size of ~ 0.10 found above.

A second series of calculations is now performed using a contrast of 0.85, and a finer grid of patch size, centered around 0.10. The contours of χ^2 are shown in Figure 5.3. χ^2 values near unity are found for patch sizes of 0.08 through 0.14[3]. The domain of best fit is seen to be largest for a fractional patch area of 0.10, and it

[2]*For this patch area the stellar disk is divided into a finer grid.*

[3]*The lower limit of 0.08 was set for practical reasons. When smaller patch sizes are used, the stellar disk must be divided more finely, thus leading to very significant increases in calculation times.*

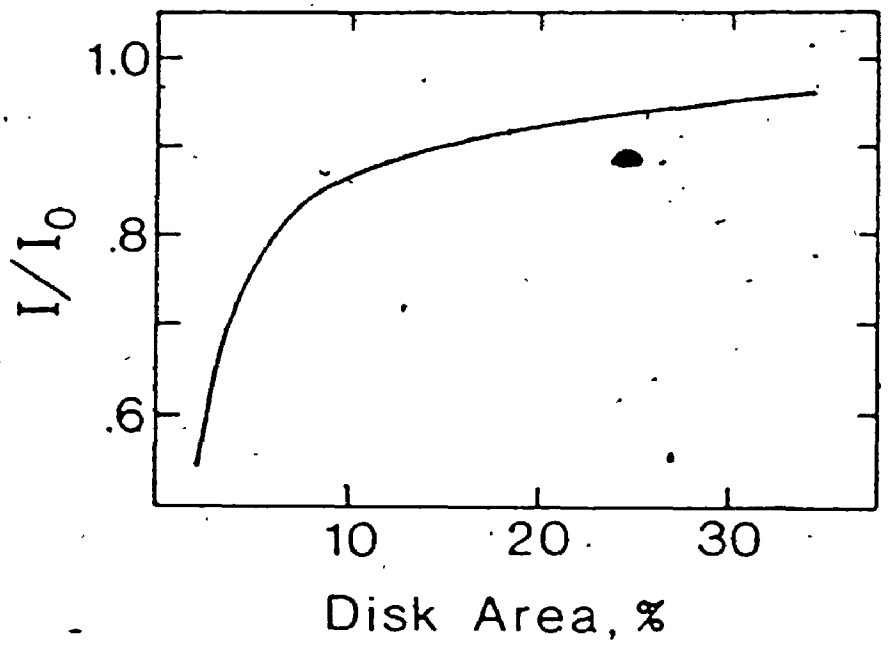

Figure 5.2 The relative brightness of the patch, I/I_o, is related to the patch area, assuming a 7% change in the V I/Fe II equivalent widths.

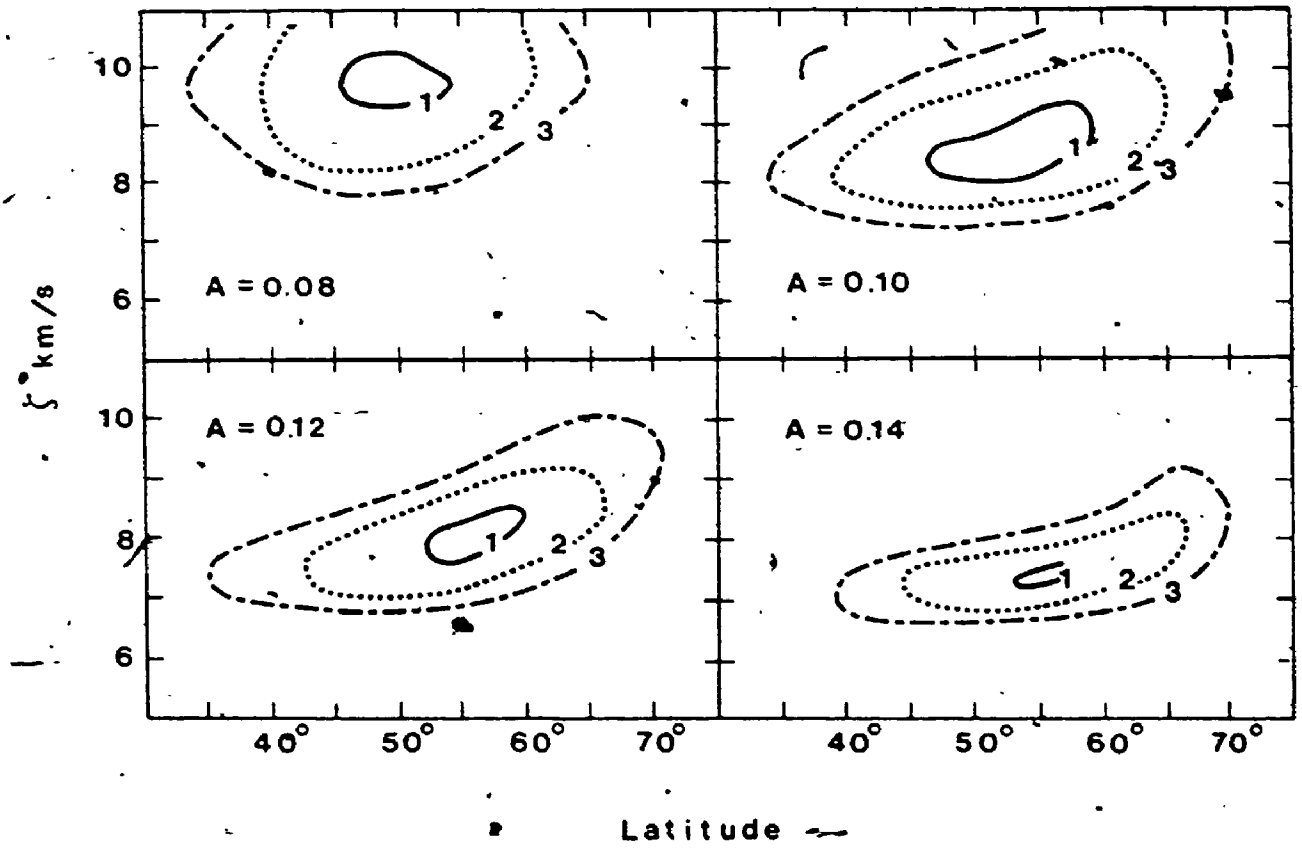

Figure 5.3 . The reduced χ^2 contours are shown for the optimum values in the velocity dispersion (ζ) - latitude plane for several values of fractional disk area (A). Contours equalling one, two and three are shown. For these contours, the patch is 15% fainter (3.7% cooler, ~ 200 K) than the rest of the photosphere.

decreases in extent when going to other patch sizes. The conclusion drawn from this is that the patch on ξ Boo A covers an area of 10% ±5% of the visible disk (2.5% of the total surface area). Since this patch size is the same as the rough estimate found above, convergence has been obtained after just one iteration, and no further iterations are needed. The remaining parameters are estimated from Figure 5.3 to be: velocity dispersion, ζ_p = 8.5 ±1.5 km s^{-1}, and latitude = 55° ±10°. The 0.85 contrast value leads to a temperature for the patch which is - 3.7% (~ 200 K) cooler than the surrounding photosphere.

The final model is compared to the observations in Figure 5.4. Pictures of the model star showing the position of the patch are presented along the top. Below this are phase diagrams of the bisectors, and the velocity spans. The agreement is excellent.

Since the integrated temperature (and brightness) of the star follow the "effective" patch area, the V I/Fe II equivalent-width ratio variations are compared to the modeled areal variations in Figure 5.5. Corrections for projection effects and limb darkening have been included when calculating the patch area. We again find excellent agreement.

Another confirmation of the goodness of fit of the model is seen in the Fourier domain. The modeled velocity-span phase curve is used to generate a synthetic time series of velocity spans. The times of the 1986 observations are first converted to phases, and the velocity span appropriate to each phase is read from the synthesized curve. These values are placed at the observed times, and the resulting time series is then Fourier analyzed. Figure 5.6 shows the amplitude

Figure 5.4 The final model is compared with the observations. Along the top are pictures of the model star for the phases indicated. In the center the observed bisectors (dashes) are compared to the simulated ones (solid lines). At the bottom, the corresponding velocity spans are shown (observations are diamonds with error bars).

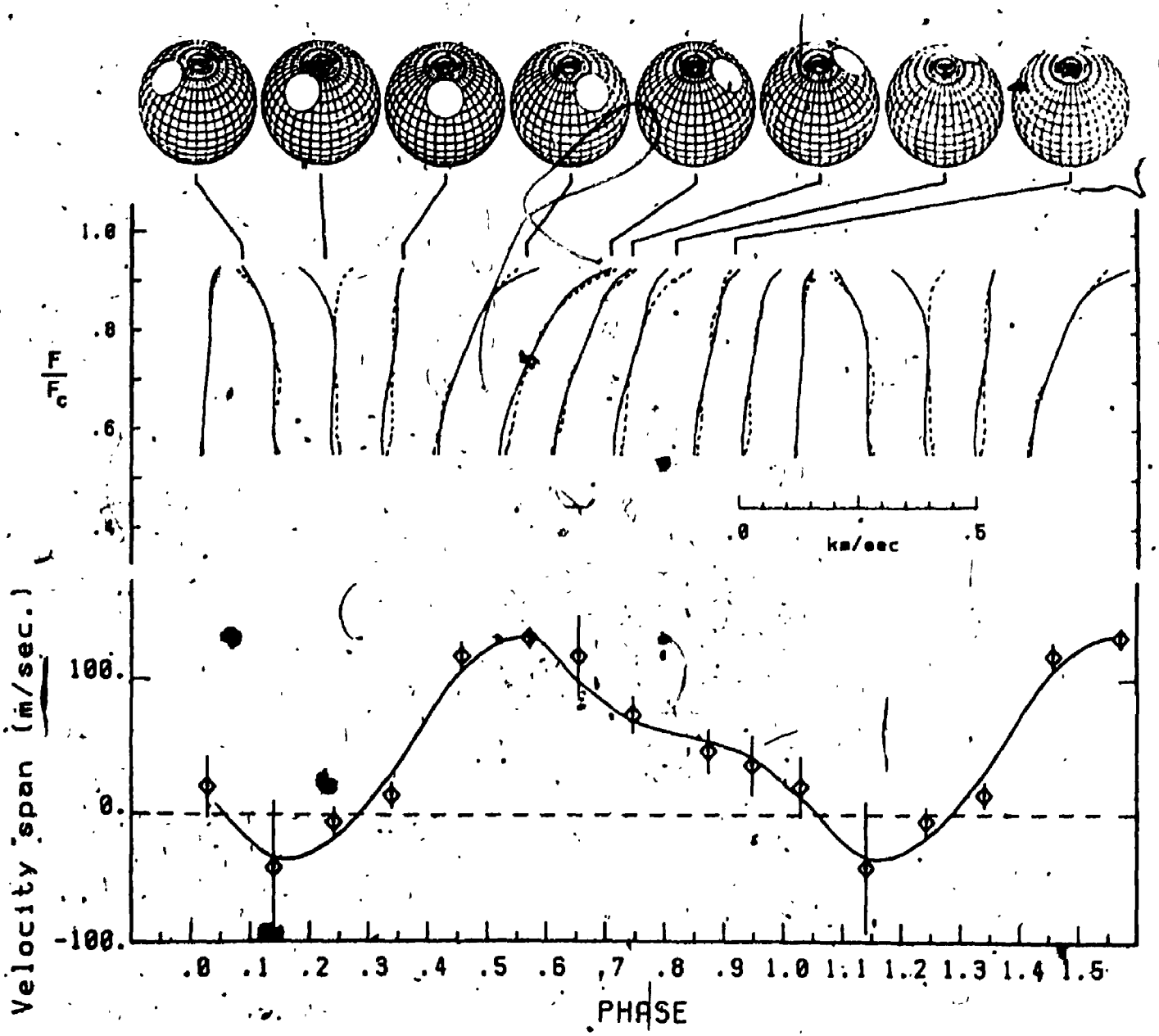
1.0
.8
.6
F/Fc
.0
km/sec
.5
Velocity span (m/sec.)
100.
0.
-100.
.0 .1 .2 .3 .4 .5 .6 .7 .8 .9 1.0 1.1 1.2 1.3 1.4 1.5
PHASE

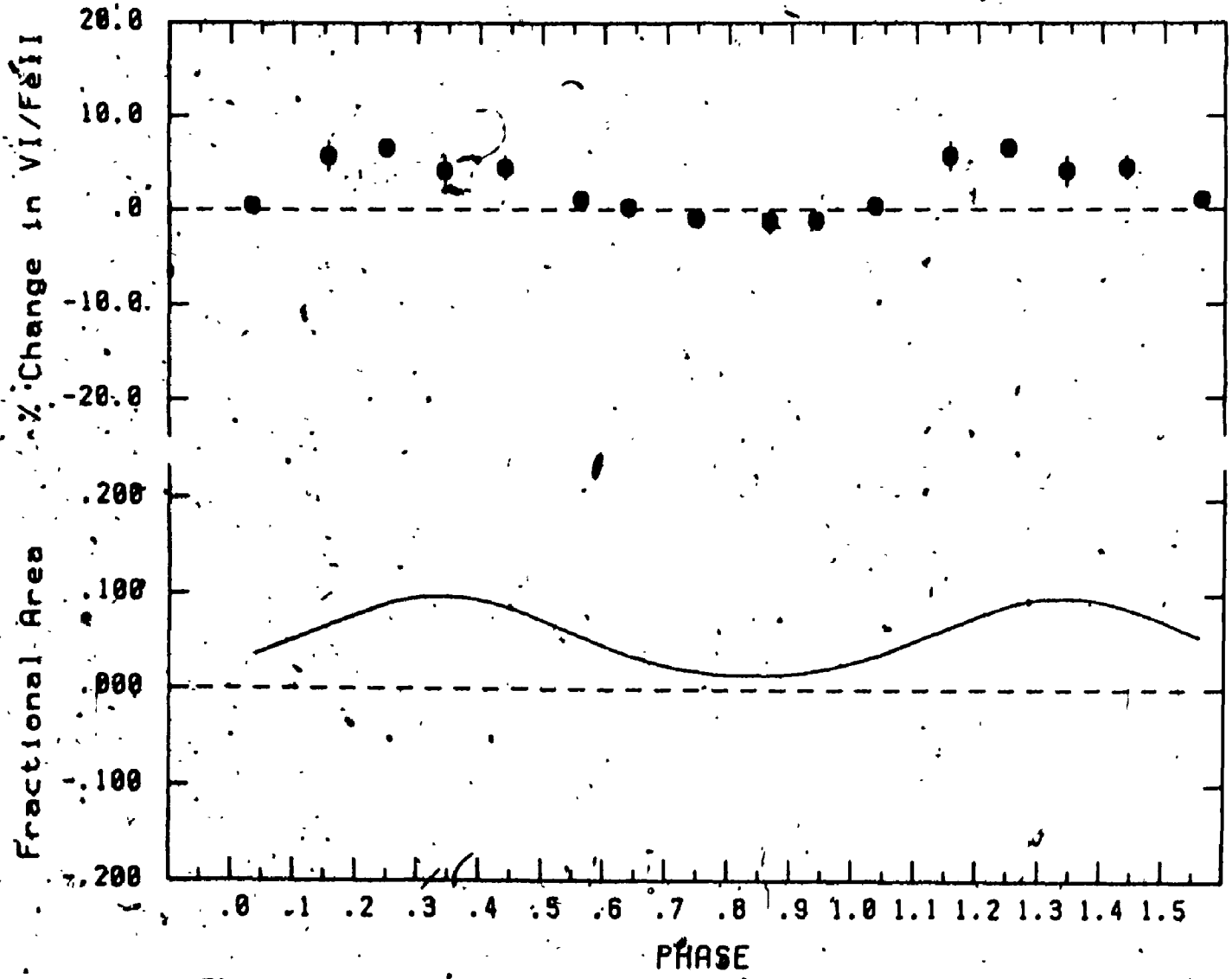

Figure 5.5 The V I/Fe II equivalent-width variations are shown along the top, and the "effective" patch area is shown along the bottom.

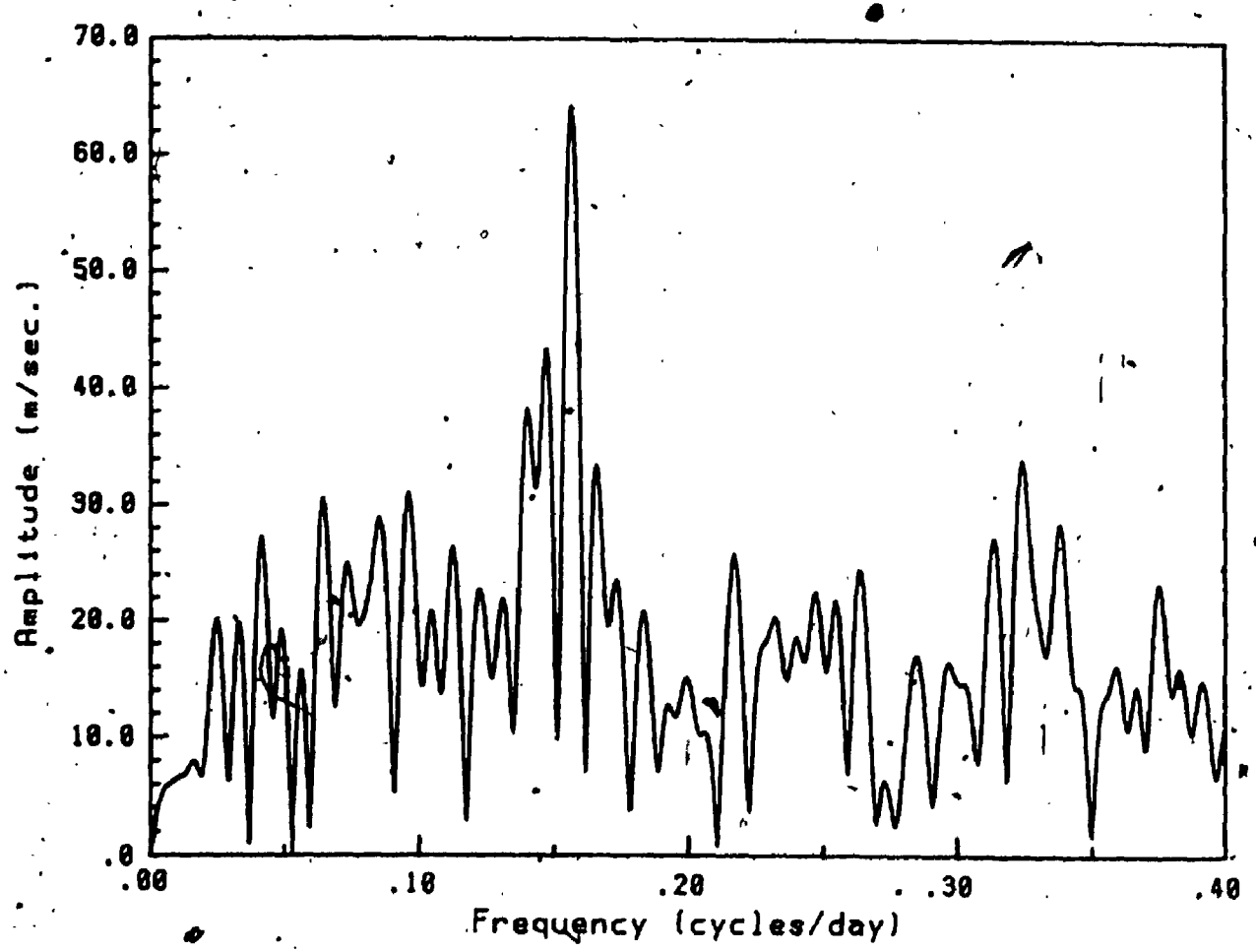

Figure 5.6 The Fourier spectrum of the synthesized time series. All of the major peaks seen in the observations (Figure 3.5a) are reproduced here. The calculation of the time series is explained in the text.

spectrum, which should be compared to Figure 3.5a. All of the major peaks seen in Figure 3.5a are reproduced in Figure 5.6, thus confirming that the secondary peaks are harmonics caused by the nonsinusoidal shape of the curve, and not real periodicities; and also showing again how well the model reproduces the observations.

5.2 Uniqueness of the Solution

5.2.1 The Secondary Variables

It was just shown that the model can reproduce observed bisector variations remarkably well. However, assumptions were made in the interest of producing a more tractable problem, and these should be investigated in greater detail. For example, can changes in the secondary variables, σ_h, σ_c, and F_c/F_h, be made? In section 4.2, it was shown that changing these variables alone within the patch cannot reproduce the amplitude or shape of the observed velocity-span curve. Therefore, they were arbitrarily fixed at the values used for the surrounding photosphere. This simplified the modeling process considerably by reducing the number of free parameters. Now we allow the secondary parameters to vary.

Numerical experiments are performed with the patch's area, latitude, contrast and velocity dispersion, and the model star's inclination, held fixed, while σ_h, σ_c, and F_c/F_h within the patch are

allowed to vary. Table 5.2 lists the basic model parameters used[4].

First, the effect of scaling the granulation velocities within the patch is investigated. Values ranging from zero (no granulation), to twice the undisturbed photospheric value are tried. The resulting curves are shown in Figure 5.7, where they are displayed in two ways. In the upper panel the velocity spans are plotted against phase, and in the lower panel the same curves are aligned such that their shape may be easily compared. We see that the largest effect of scaling v_h and v_c is a modification of the relative amplitude between the maximum and minimum in each curve. The center of the flattest portion of each curve is now used as a reference point, and the amplitudes of the maximum and minimum are measured relative to this point. These amplitudes are ratioed, and plotted in Figure 5.8 against the factor by which v_h and v_c have been scaled. We see that the relation is approximately linear. As the granulation velocities are scaled up, the amplitude of the maximum decreases relative to the amplitude of the minimum. This same ratio, measured from the observed curve, is 1.0 ±0.36. Referring to Figure 5.8, this suggests an approximately 25% reduction of the granulation velocities within the patch.

Now, the influence of F_c/F_h is investigated. Phase curves, with F_c/F_h scaled by zero (only a hot column) through three (a relatively large cold stream contribution), are computed, and shown in Figure 5.9. Again we see a change in the relative amplitudes of the maxima

[4] *Note that the basic parameter values used in this experiment are those of the final model found in section 5.1.*

Table 5.2

The Basic Model Parameters

for Investigating the Question of Uniqueness

The Fixed Parameters:	The Variable Parameters*:
$v \sin i = 3.0$ km s^{-1}	$v_h = 4.0$ km s^{-1}
$A = 0.10$	$v_c = -1.4$ km s^{-1}
$\ell = 55°$	$F_c/F_h = 0.10$
$I/I_o = 0.85$	
$\zeta = 8.5$ km s^{-1}	
$i = 40°$	

*These are the unscaled values of the variable parameters.

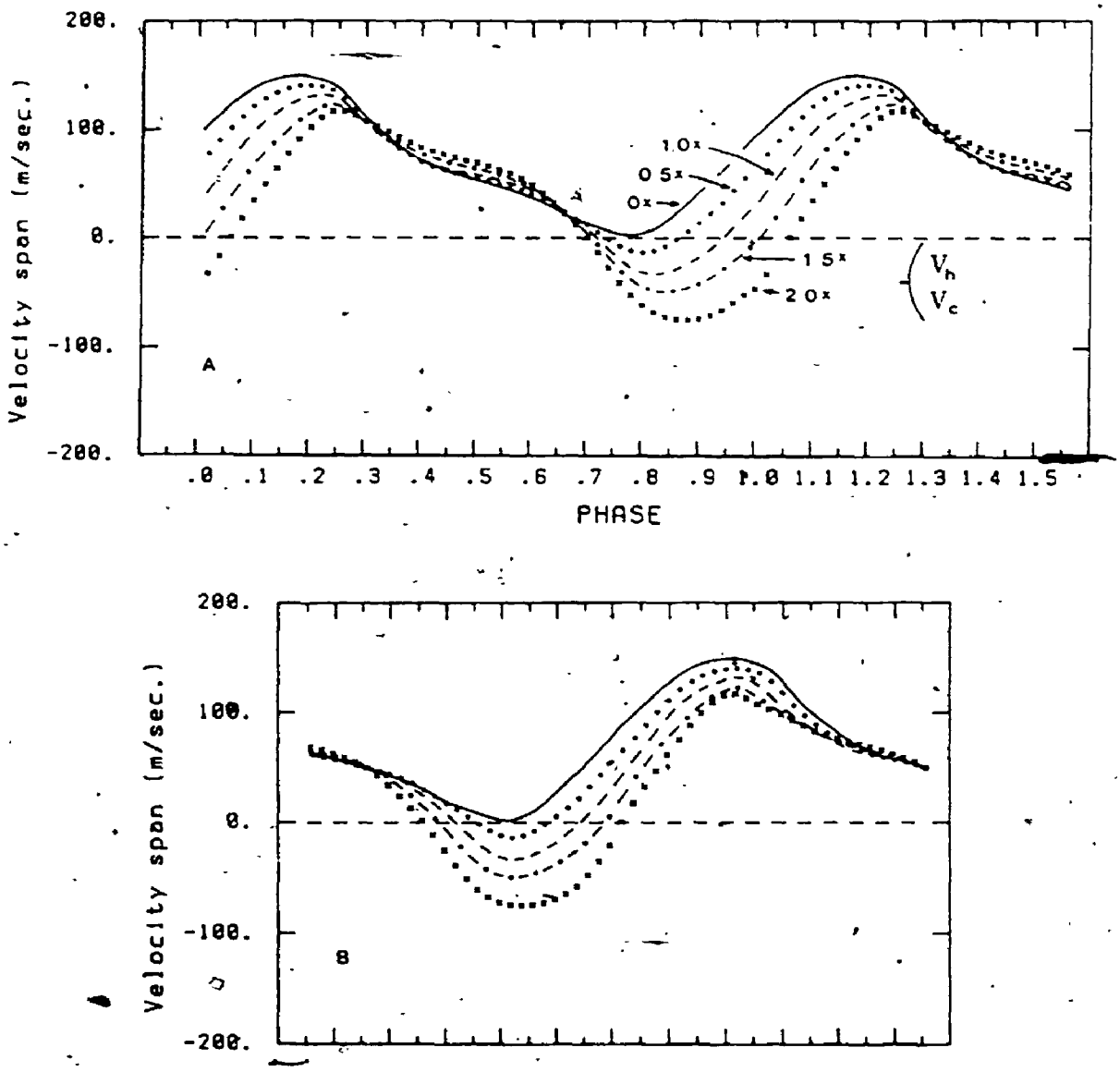

Figure 5.7.—The granulation velocities in the final model are scaled relative to their photospheric values (A). The scale factors are given in the figure. In (B) the curves have been shifted horizontally so that their shape may be compared.

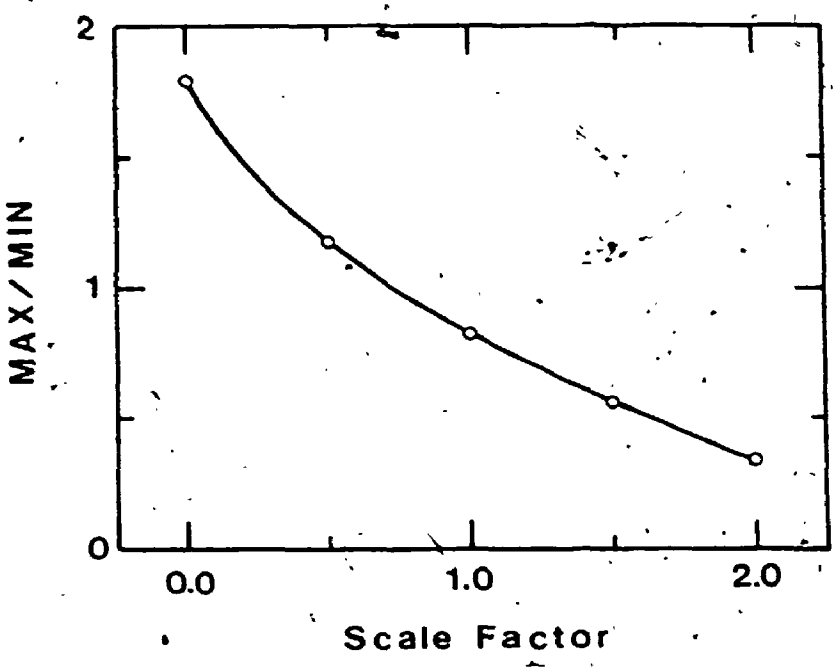

Figure 5.8 The ratio of curve maximum to minimum is plotted against granulation velocity scale factor. The maxima and minima are calculated relative to the flattest portion of the curves.

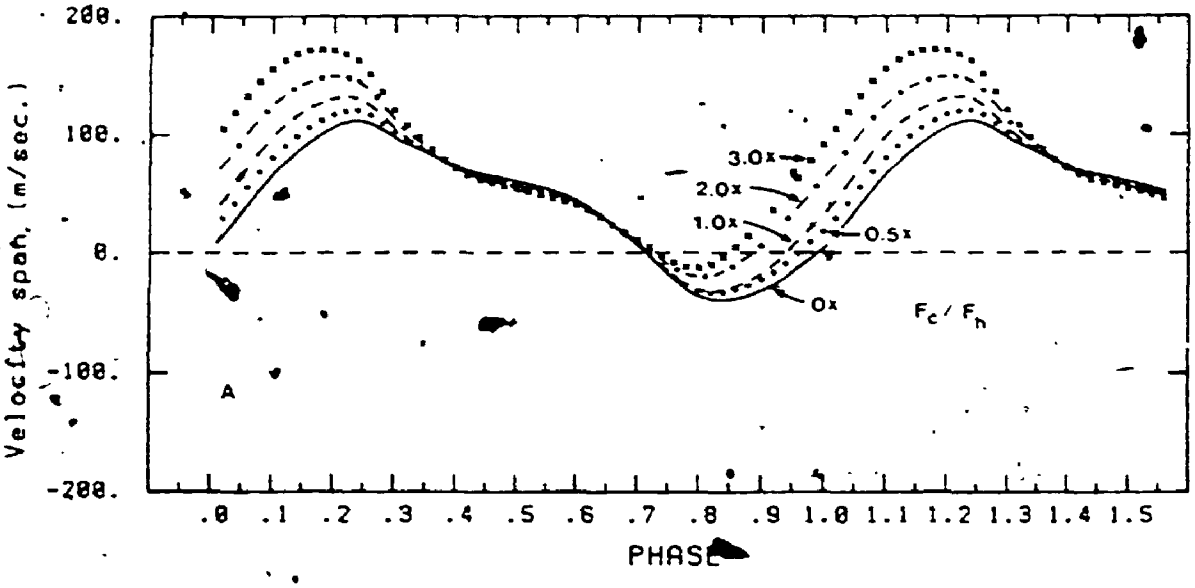

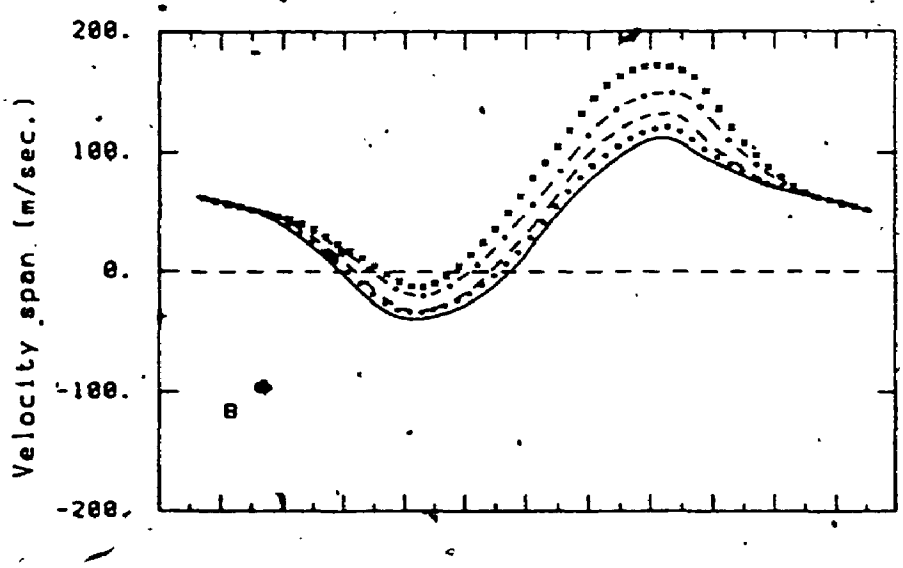

Figure 5.9 The granulation contrast in the final model is scaled relative to its photospheric value (A). The scale factors are given in the figure. In (B) the curves have been shifted horizontally so that their shape may be compared.

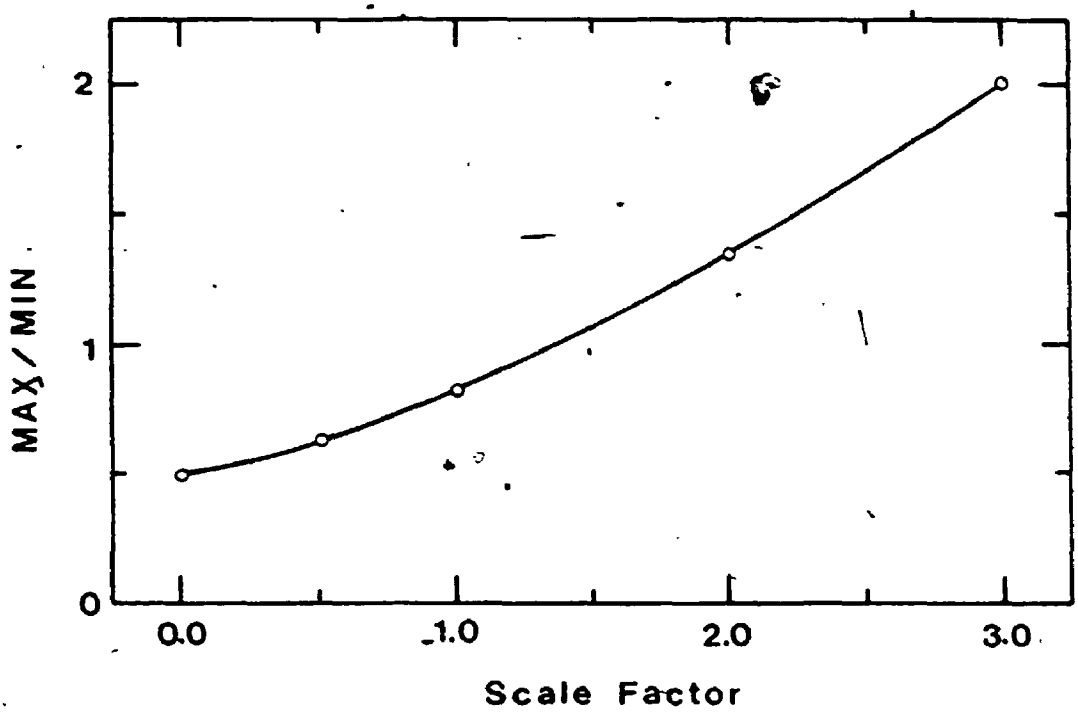

Figure 5.10 The ratio of curve maximum to minimum is plotted against granulation contrast scale factor. The maxima and minima are calculated relative to the flattest portion of the curves.

and minima. The ratio of the maximum to the minimum is shown plotted against scale factor in Figure 5.10. In this case, comparison with the observations indicates an approximately 25% increase for F_c/F_h.

Neither of these effects are large compared to the experimental errors. So, although ~ 25% changes in the secondary variables cannot be ruled out, there is no compelling evidence in favour of including such modifications in the modeling process.

5.2.2 The Inclination

It was assumed in the modeling that the rotation axis of ξ Boo A is perpendicular to the orbital plane; thus leading to an inclination of 40° to our line of sight. Is this a reasonable assumption? If we use the measured period of 6.43 days, combined with a $v \sin i$ of 3.0 km s^{-1} and a stellar radius of 1.01 $R_\odot$ (Gray 1967), we arrive at an inclination of only ~ 25°. Can the choice of 40° be justified in light of this calculation? To answer this, let us examine the quantities involved. Both the measured $v \sin i$ and the stellar radius are rather uncertain. If the uncertainties are taken into consideration, the best estimate for the inclination turns out to be 30° ±15°. This is a fairly large range, but it does include the 40° inclination actually used.

To test how different inclinations modify the solution, calculations are performed using a range of inclination. Three values

are considered, 20°, 30°, and 50°. Because of the large amount of computation involved, only a fractional disk area of 10% is considered, and only the $\chi^2 = 1$ contours are found. The results of these calculations are shown in Figure 5.11. (The $\chi^2 = 1$ contour for an inclination of 40° has been included for comparison.) We see that as the inclination is decreased (i.e. as the star is viewed more nearly pole-on), the domain of best fit moves to lower latitudes and decreases in extent. For an inclination of 20°, the domain of best fit has become quite small, and so extrapolating to lower inclinations, it is estimated that no solutions will be possible for inclinations less than ~ 15°. This is simply because the patch's projected area and its effective radial velocity will no longer change sufficiently to produce the observed variations. At this point, the patch cannot be below ~ 40° latitude. Higher inclinations cause the domain of best fit to move towards the pole. This is because there is no flat portion in the observed velocity-span phase diagram, indicating that the patch can never completely disappear behind the star.

It should be noted at this point that the minimum χ^2 value ($\chi^2 = 0.75$) is found when using an inclination of 30°. This minimum occurs at a latitude of 46° and a velocity dispersion of 8.2 km s^{-1}. This is only 6% smaller than the next smallest minimum ($\chi^2 = 0.81$, at $i = 40°$, $\ell = 53°$, $\zeta = 8.5$ km s^{-1}, and $A = 0.10$), but it could be taken to indicate that a lower inclination might be preferred. However, we see from Figure 5.11, that decreasing the inclination to 30° does not change the results significantly.

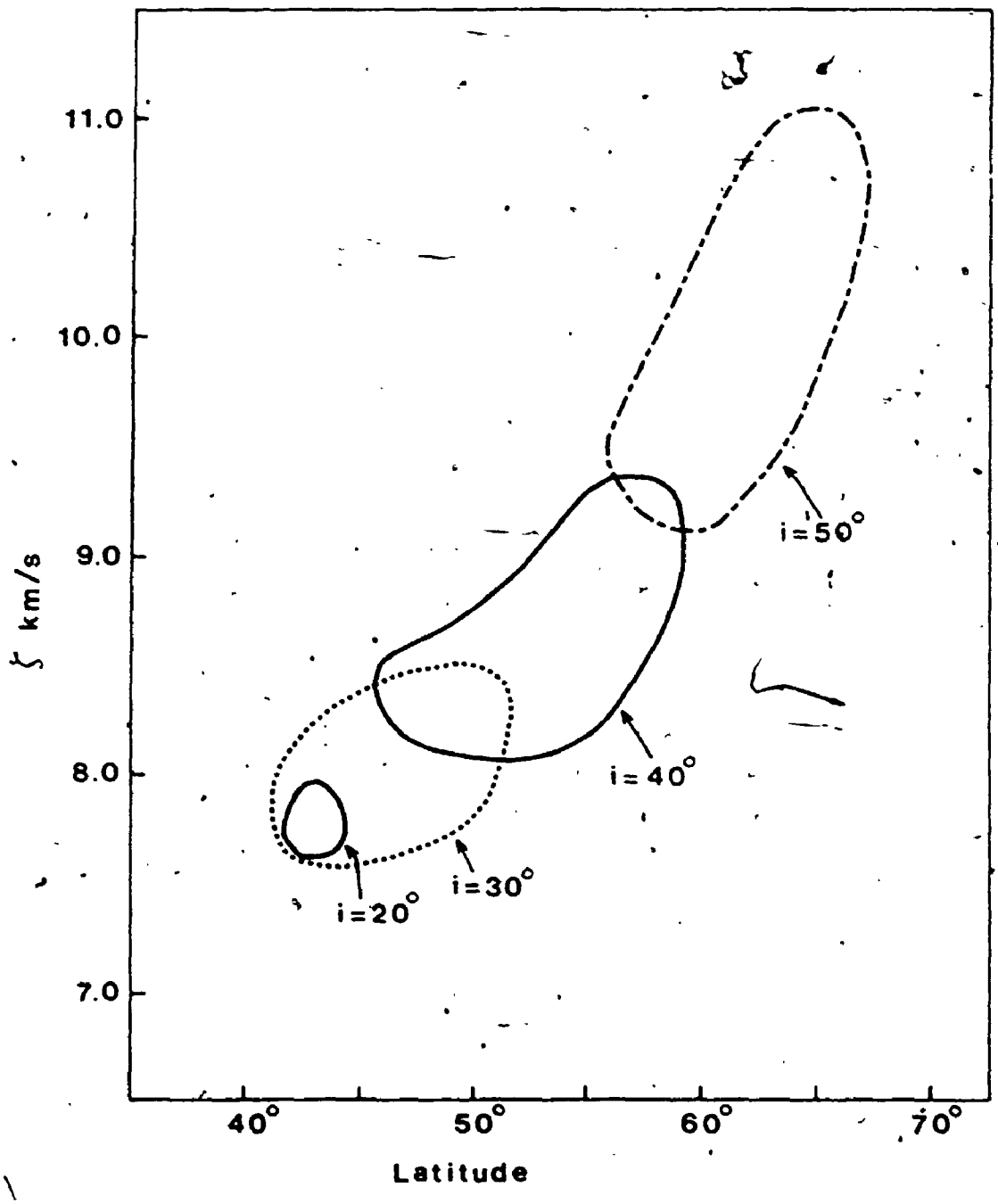

Figure 5.11 The inclination (i) sensitivity is illustrated. The $\chi^2 - 1$ contours for four inclinations are shown. As the model star is viewed more nearly pole-on, the region of best-fit moves towards the equator and decreases in extent. Extrapolating to lower inclinations, no solutions will be possible for inclinations less than ~ 15°.

5.2.3 The Rotation

The study of the rotation sensitivity of the solution is complicated by the fact that changes in the rotation require changes in both the macroturbulent dispersion and the global granulation. The macroturbulence changes in response to the rotation because the total observed line broadening must be conserved. An increase in the assumed rotation requires a corresponding decrease in the macroturbulent dispersion. The granulation changes with rotation because of a redistribution of the velocity distributions. Increasing the rotation requires a decrease in the granulation.

For ξ Boo A, increasing $v \sin i$ from 3.0 to 3.5 km s^{-1} requires a decrease in the macroturbulence from 5.0 to 4.5 km s^{-1}. The new granulation parameters for this combination of macrobroadeners are found to be, v_h = -0.9 km s^{-1}, v_c = 3.5 km s^{-1}, and F_c/F_h = 0.10. Using a patch area of 0.10, a patch contrast of 0.85, and an inclination of 40°, the χ^2 = 1.0 contour is found, following the procedure outlined in section 5.1. This contour is shown in Figure 5.12, compared to the corresponding contour from Figure 5.3. The differences are small, and within the quoted errors. One concludes that small changes in the assumed rotation do not seriously modify the solution.

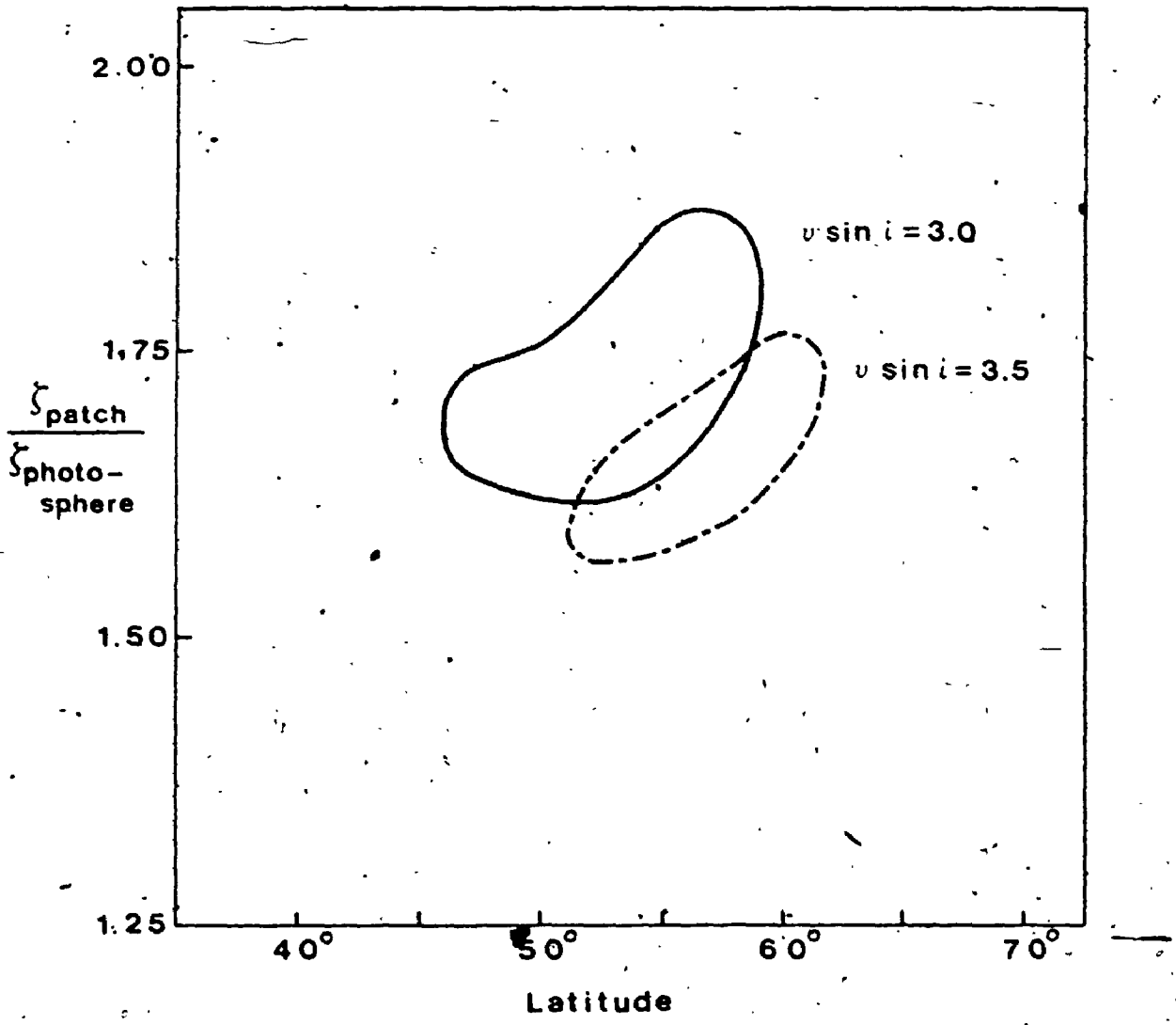

Figure 5.12 The $\chi^2 - 1$ contour assuming a $v \sin i$ of 3.5 km s^{-1} is compared to the corresponding contour with $v \sin i$ = 3.0 km s^{-1}. There is only a small difference between these two contours, well within the quoted errors. The other parameters used for the calculation are given in the text.

Chapter 6

Summary and Conclusions

Variations in the spectral lines of ξ Boo A have been documented for the 1984 through 1987 observing seasons. The line asymmetry and the V I/Fe II equivalent-width ratio are found to vary in phase, with a period of 6.43 days. This period matches the known rotational period of the star, and it has remained constant to within ~ 0.2% over the four years of the study. The constancy of the period is taken as evidence that there is no differential rotation. The amplitude of the variations may have been smaller in the 1984 and 1985 seasons, but the evidence for this is slim. A search for changes in the Zeeman broadening produced negative results.

The observations have been explained in terms of a surface feature, carried around the star by rotation. The most distinguishing characteristic of the feature is a velocity dispersion which is enhanced by a factor of 1.5 - 2.0 relative to the "immaculate" photosphere. The feature covers approximately 10% of the visible disk (2.5% of the total surface), and is ~ 3.7% cooler (15% fainter) than the surrounding photosphere. Other important aspects of the deduced feature are that it lies at relatively high latitudes (~ 55° ±10°), and that it has remained essentially unchanged for at least four years. Combining all of this with the apparent lack of any Zeeman broadening associated with the feature, one is led to the conclusion that it is quite different from a classical sunspot. Therefore, the

name "Starpatch" is suggested for this type of feature in order to distinguish it from the traditional (magnetic) sunspot.

We cannot, however, rule out the existence of magnetic fields entirely. Fields may reside in small, very dark regions scattered about within the patch boundary. Being so dark, these regions would not contribute significantly to the integrated light, and hence the signature of the magnetic field would be correspondingly diminished. Under this scenario, the observed contrast is an average over the entire patch area, including bright and dark regions. However, such a conglomeration of dark, magnetic regions, contributing little to the observed light from the star, would not modify the deduced macrobroadening for the patch; but we saw in section 3.4 that the line broadening does indeed change, and in Chapter 4 it was shown that only an enhanced macroturbulence within the patch can reproduce the observed line bisector behavior. Turning this around, the existence of enhanced macro-velocities can be used as an argument against the presence of magnetic fields; for we see that on the sun, magnetic fields are quite effective at inhibiting convection. Therefore, although magnetic fields cannot be completely ruled out; their presence in the patch seems unlikely.

Apparently, the patch on ξ Boo A has a bright region in the chromosphere above it, as inferred from the Ca II H and K measurements of Saar et al. (1987). This might be used as a counter-argument in favor of magnetic fields. However, the enhanced velocity dispersion within the patch might easily give rise to a bright chromosphere through acoustic-wave dissipation.

When we compare the deduced characteristics of the starpatch on ξ Boo A with our knowledge of starspots, we find a number of similarities. Both the starpatch and starspots cover large fractions of the stellar surface, both are found at high latitudes, and both have long lifetimes. These are the same features which make starspots and starpatches stand apart from the traditional sunspot. One speculates that, maybe, starspots are just extreme cases of the starpatch phenomenon, and that perhaps, they have been misnamed. Unfortunately, there are no measurements of velocity dispersions within starspots, nor have starspot magnetic fields been measured, so such speculation may be premature. Future studies must be designed to settle this question.

Continued monitoring of a number of late-type stars is needed to determine how common the starpatch phenomenon really is. The existence of starpatches also complicates the study of stellar granulation, because a single exposure can no longer be relied upon to give an accurate measure of the granulation characteristics. Future investigations of stellar granulation must take this into consideration. A series of observations will be needed to first establish if the star has one or more patches, and if there is some phase when the patches are hidden from view. Granulation characteristics within starpatches will be of enormous interest in their own right.

APPENDIX A

Journal of Observations and Basic Results

The following table lists the observations and the basic results of the data analysis. Only those exposures having a S/N greater than ~ 100 have been included. The date of the observation is given in column 1, while column 2 gives the Julian Date for the midpoint of the exposure, and column 3 is the approximate signal-to-noise (calculated using equation 2-7b). The remaining two columns give the velocity span of the mean line bisector and the V I/Fe II equivalent-width ratio, respectively. The λ6150 region exposures are indicated by an asterisk next to the entry in the table.

TABLE A-1

Journal of Observations and Basic Results

Date of Observation	J.D. - 2440000	S/N Ratio	Velocity Span ($m\ s^{-1}$)	V I/Fe II
1984 June 26-27	2445878.647	320	60 ± 38	—
1984 June 30	2445882.607	350	-32 ± 28	—
1984 July 11-12	2445893.681	230	11 ± 38	—
1984 July 13-14	2445895.615	400	84 ± 23	—
1984 July 18-19	2445900.610	310	38 ± 30	—
1985 Apr 15-16	2446171.734	290	-7 ± 32	0.636
1985 Apr 16-17	2446172.839	140	116 ± 53	0.699
1985 Apr 28-29	2446184.714	200	106 ± 47	0.590
1985 Apr 28-29	2446184.801	210	72 ± 50	0.606
1985 Apr 29-30	2446185.738	250	72 ± 39	0.644
1985 Apr 29-30	2446185.801	280	48 ± 35	0.672
1985 May 09-10	2446195.680	200	49 ± 43	0.592
1985 May 09-10	2446195.765	210	76 ± 51	0.569
1985 May 10-11	2446196.768	210	-34 ± 51	0.574
1985 May 12-13	2446198.639	150	238 ± 65	0.590
1985 May 21-22	2446207.649	250	7 ± 35	0.637
1985 May 23-24	2446209.592	410	12 ± 26	0.581
1985 May 23-24	2446209.677	370	40 ± 25	0.590
1985 May 24-25	2446210.675	170	124 ± 52	0.474
1985 June 03-04	2446220.599	240	60 ± 39	0.545
1985 June 05-06	2446222.688	280	-59 ± 37	0.560

TABLE A-1

(continued)

Date of Observation	J.D.	~ S/N Ratio	Velocity Span ($m\ s^{-1}$)	V I/Fe II
1985 June 06-07	2446223.618	300	54 ± 29	0.588
1985 June 06-07	2446223.715	290	9 ± 31	0.615
1985 June 09-10	2446226.646	250	112 ± 52	0.685
1985 June 14-15	2446231.665	250	74 ± 45	0.636
1985 June 18-19	2446235.663	220	184 ± 43	0.597
1985 June 26-27	2446243.610	520	89 ± 16	0.643
1985 June 26-27	2446243.675	470	145 ± 18	0.582
1985 July 10-11	2446257.597	300	114 ± 27	0.614
1985 July 12-13	2446259.673	330	52 ± 26	0.718
1985 July 17-18	2446264.612	240	65 ± 49	0.490
1985 July 17-18	2446264.655	140	-40 ± 82	0.589
1985 July 20-21	2446267.624	370	26 ± 31	0.574
1986 Apr 02-03	2446523.684	330	30 ± 29	0.603
1986 Apr 02-03	2446523.782	280	-48 ± 32	0.576
1986 Apr 02-03	2446523.878	250	-1 ± 35	0.591
1986 Apr 12-13	2446533.675	340	137 ± 25	0.580
1986 Apr 12-13	2446533.772	360	109 ± 25	0.636
1986 Apr 12-13	2446533.899	190	159 ± 44	0.618
1986 Apr 13-14	2446534.676	470	42 ± 19	0.592
1986 Apr 13-14	2446534.765	430	35 ± 20	0.573
1986 Apr 13-14	2446534.884	260	102 ± 37	0.593

TABLE A-1

(continued)

Date of Observation	J.D.	S/N Ratio	Velocity Span ($m\ s^{-1}$)	V I/Fe II
1986 Apr 22-23	2446543.757	330	-46 ± 29	0.650
1986 Apr 23-24	2446544.736	430	-28 ± 20	0.657
1986 Apr 23-24	2446544.831	470	-18 ± 18	0.664
1986 Apr 24-25	2446545.634	440	114 ± 20	0.618
1986 Apr 24-25	2446545.750	360	99 ± 23	0.621
1986 Apr 24-25	2446545.864	260	113 ± 31	0.643
1986 Apr 25-26	2446546.611	380	136 ± 20	0.611
1986 Apr 25-26	2446546.709	390	162 ± 20	0.583
1986 Apr 25-26	2446546.804	340	151 ± 23	0.581
1986 Apr 25-26	2446546.884	160	113 ± 55	0.602
1986 Apr 26-27	2446547.631	370	113 ± 22	0.549
1986 Apr 26-27	2446547.737	420	75 ± 20	0.569
1986 Apr 26-27	2446547.851	480	101 ± 17	0.616
1986 Apr 27-28	2446548.632	310	62 ± 25	0.604
1986 Apr 27-28	2446548.749	490	42 ± 16	0.586
1986 Apr 27-28	2446548.859	320	78 ± 23	0.603
1986 Apr 29-30	2446550.635	310	22 ± 25	0.649
1986 Apr 29-30	2446550.735	350	0 ± 25	0.648
1986 Apr 29-30	2446550.848	480	-4 ± 18	0.611
1986 June 17-18	2446599.607	450	85 ± 18	0.572
1986 June 17-18	2446599.707	650	55 ± 12	0.546

TABLE A-1

(continued)

Date of Observation	J.D. -	S/N Ratio	Velocity Span ($m\ s^{-1}$)	V I/Fe II
1986 June 18-19	2446600.591	420	-38 ± 22	0.563
1986 June 18-19	2446600.663	170	-91 ± 42	0.596
1986 June 28-29	2446610.641	480	139 ± 18	0.554
1986 June 29-30	2446611.639	200	120 ± 42	0.620
1986 June 30	2446612.623	360	-11 ± 21	0.533
1986 July 02-03	2446614.665	270	-37 ± 36	0.611
1986 July 03-04	2446615.642	560	31 ± 13	0.606
1986 July 04-05	2446616.643	260	122 ± 28	0.577
1986 July 05-06	2446617.646	590	125 ± 14	0.589
1986 July 06-07	2446618.641	560	7 ± 18	0.586
1986 July 07-08	2446619.672	450	2 ± 19	0.569
1986 July 09-10	2446621.611	430	-18 ± 18	0.651
1986 July 16-17	2446628.588	250	32 ± 36	0.628
1986 July 17-18	2446629.619	500	108 ± 16	0.601
1986 July 19-20	2446631.593	100	54 ± 83	0.569
1986 July 20-21	2446632.623	440	31 ± 17	0.582
1986 July 22-23	2446634.615	510	40 ± 17	0.577
1986 July 23-24	2446635.621	490	122 ± 21	0.559
1986 Aug 01-02	2446644.592	220	108 ± 34	0.610
1986 Aug 02-03	2446645.615	490	49 ± 15	0.580
1986 Aug 03-04	2446646.594	310	26 ± 32	0.580

TABLE A-1

(continued)

Date of Observation	J.D.	S/N Ratio	Velocity Span ($m\ s^{-1}$)	V I/Fe II
1986 Aug 04-05	2446647.600	460	27 ± 26	0.613
1986 Aug 11-12	2446654.625	370	139 ± 24	0.601
1986 Aug 12-13	2446655.602	330	18 ± 31	0.634
1986 Aug 13-14	2446656.603	220	4 ± 39	0.556
1986 Aug 17-18	2446660.605	190	11 ± 61	0.624
1986 Aug 18-19	2446661.603	180	124 ± 48	0.626
1986 Aug 19-20	2446662.601	260	78 ± 39	0.638
1986 Aug 21-22	2446664.597	290	91 ± 28	0.611
1986 Aug 22-23	2446665.594	120	30 ± 87	0.573
1987 Apr 26-27	2446912.722	260	120 ± 33	0.591
1987 May 08-09	2446924.697	230	72 ± 40	0.591
1987 May 13-14	2446929.690	250	60 ± 34	0.608
1987 June 07-08	2446954.668	430	28 ± 17	0.604
1987 June 24-26	2446971.628	690	14 ± 13	0.503
1987 June 24-25	2446971.698	430	14 ± 22	0.546
1987 June 25-26	2446972.616	300	25 ± 30	0.554
1987 June 26-27	2446973.644	550	44 ± 15	0.572
1987 June 28-29	2446975.663	480	-1 ± 16	0.594
1987 July 04-05	2446981.610	420	-1 ± 19	0.594
1987 July 04-05	2446981.682	440	-35 ± 18	0.594
1987 July 08-09	2446985.608	730	-17 ± 13	0.570

TABLE A-1

(concluded)

Date of Observation	J.D.	~ S/N Ratio	Velocity Span ($m\ s^{-1}$)	V I/Fe II
1987 July 11-12	2446988.629	770	25 ± 12	0.598
1987 July 16-17	2446993.600	580	25 ± 16	0.614
1987 July 17-18	2446994.595	630	-2 ± 13	0.612
1987 July 17-18	2446994.679	570	50 ± 17	—
1987 July 18-19	2446995.601	370	80 ± 24	0.559
1987 July 18-19	2446995.697	390	72 ± 26	—
1987 July 21-22	2446998.602	510	76 ± 22	—
1987 July 21-22	2446998.673	590	10 ± 17	0.583
1987 July 22-23	2446999.595	630	100 ± 20	—
1987 July 22-23	2446999.667	210	36 ± 47	0.580
1987 July 23-24	2447000.636	190	-36 ± 62	—
1987 July 26-27	2447003.607	410	40 ± 25	—
1987 Aug 03-04	2447011.583	710	66 ± 12	0.571
1987 Aug 05-06	2447013.611	360	-23 ± 27	0.640
1987 Aug 10-11	2447018.594	640	98 ± 17	0.554
1987 Aug 15-16	2447023.597	350	53 ± 31	0.556

APPENDIX B

Explaining the Synthesized Bisector Variations

The patch represents a region of excess line broadening. Rotation carries the patch around the star, and rotational Doppler shifts move the patch's effects across the observed line profile. Because of the low rotational velocities encountered for late-type stars, the patch's influence is confined to a limited fraction of the observed profile. Exactly what this does to the profile can be understood with the aid of a couple of illustrative examples.

An appropriate test case has a patch with the velocity dispersion enhanced relative to the surrounding photosphere, but has no granulation to confuse the interpretation of the line asymmetry. The geometry of the test case is kept simple, with the patch on the equator of the model star, and the inclination of the rotation axis set at 90°. Figure B.1 shows a series of pictures of the model star, along with the calculated bisectors and the velocity spans. We see that the asymmetry changes are anti-symmetric about phase zero (i.e. when the patch transits), and that as the patch passes out of view behind the star, the profile becomes symmetric, and remains so until the patch reappears at the opposite limb.

In Figure B.2 the calculated profiles for three representative phases, going from disk center to the receding limb, are shown. Included in the figure are the velocity distributions at patch center (calculated using equation 4-1), and the resulting bisectors. We see

that when the patch is at the center of the disk it acts to symmetrically broaden the line profile; thus, the bisector is vertical. As the patch moves away from disk center, the additional broadening it provides is shifted by the rotational Doppler shift appropriate to the patch's position on the disk. This removes some of the broadening from the opposite wing, causing that wing to move towards the continuum. At the same time, projection affects narrow the velocity distribution within the patch, and reduce the effective area of the patch. The maximum asymmetry occurs when the combination of rotation and effective patch area is a maximum. When the patch reaches the limb, its area, and the width of the velocity distribution, are reduced to the point that it no longer broadens the profile. The red wing now moves up to its normal, undisturbed state. When the patch reappears at the approaching limb, the process is repeated in reverse, thus leading to the anti-symmetric nature of the variation.

Figure B.3 shows what happens when granulation is included. This picture looks much more complicated than the one above, but in reality it is not. What we are seeing is simply the patch induced variation found earlier, superimposed onto the basic granulation induced asymmetry. This becomes obvious when we examine the velocity span curve in the bottom panel of the figure. We see here exactly the same shape found above, but a vertical shift has been introduced. This shift is due to the global granulation. The explanation for the asymmetry changes follows exactly as above.

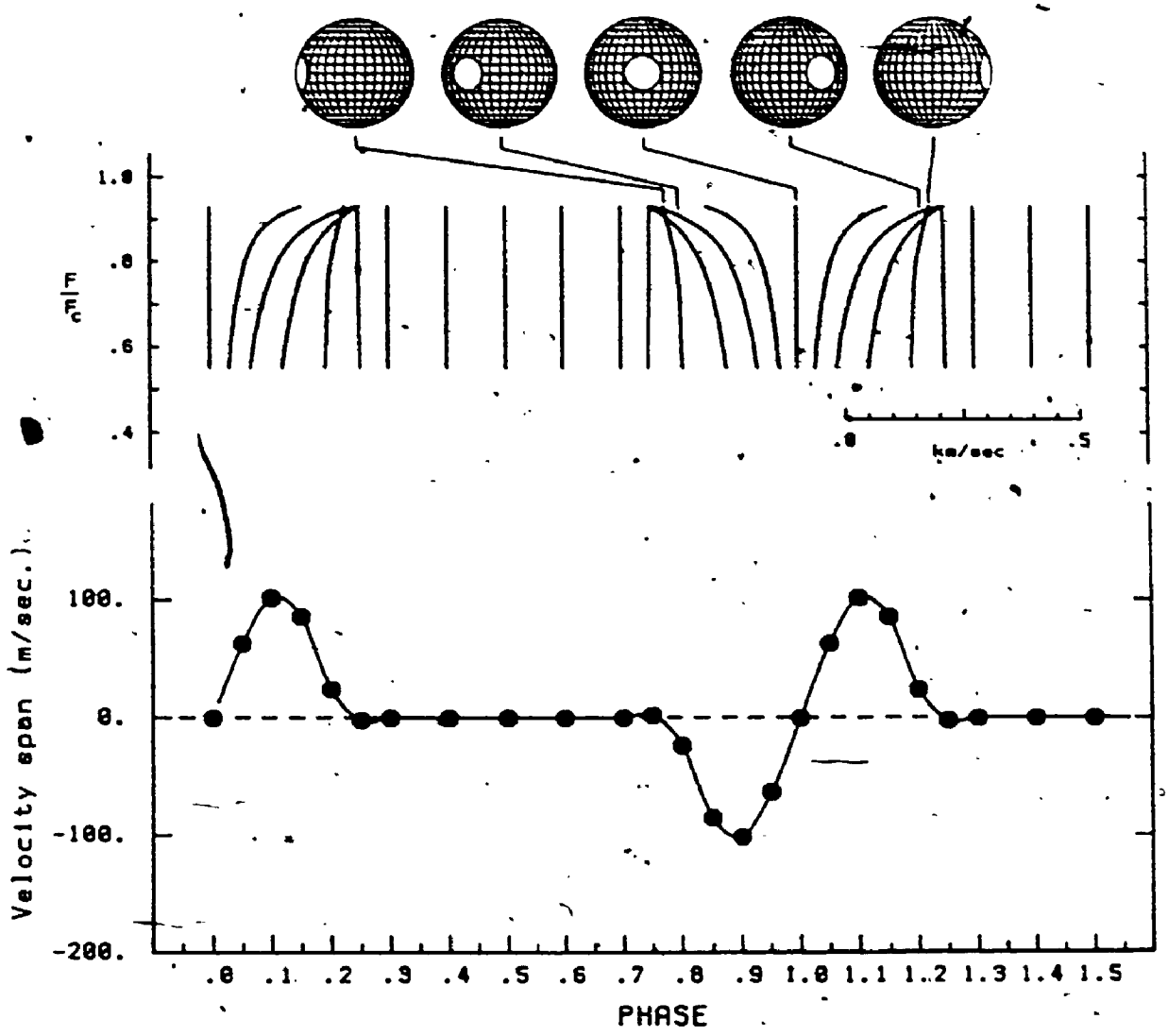

Figure B.1 A simple test case with an enhanced velocity dispersion (8.5 km s^{-1}, compared to 5.0 km s^{-1} in the surrounding photosphere), and no granulation. Along the top are pictures of the model star for the phases indicated. Center are the bisectors, and at the bottom are the velocity spans. Note that the asymmetry changes are anti-symmetric about phase zero.

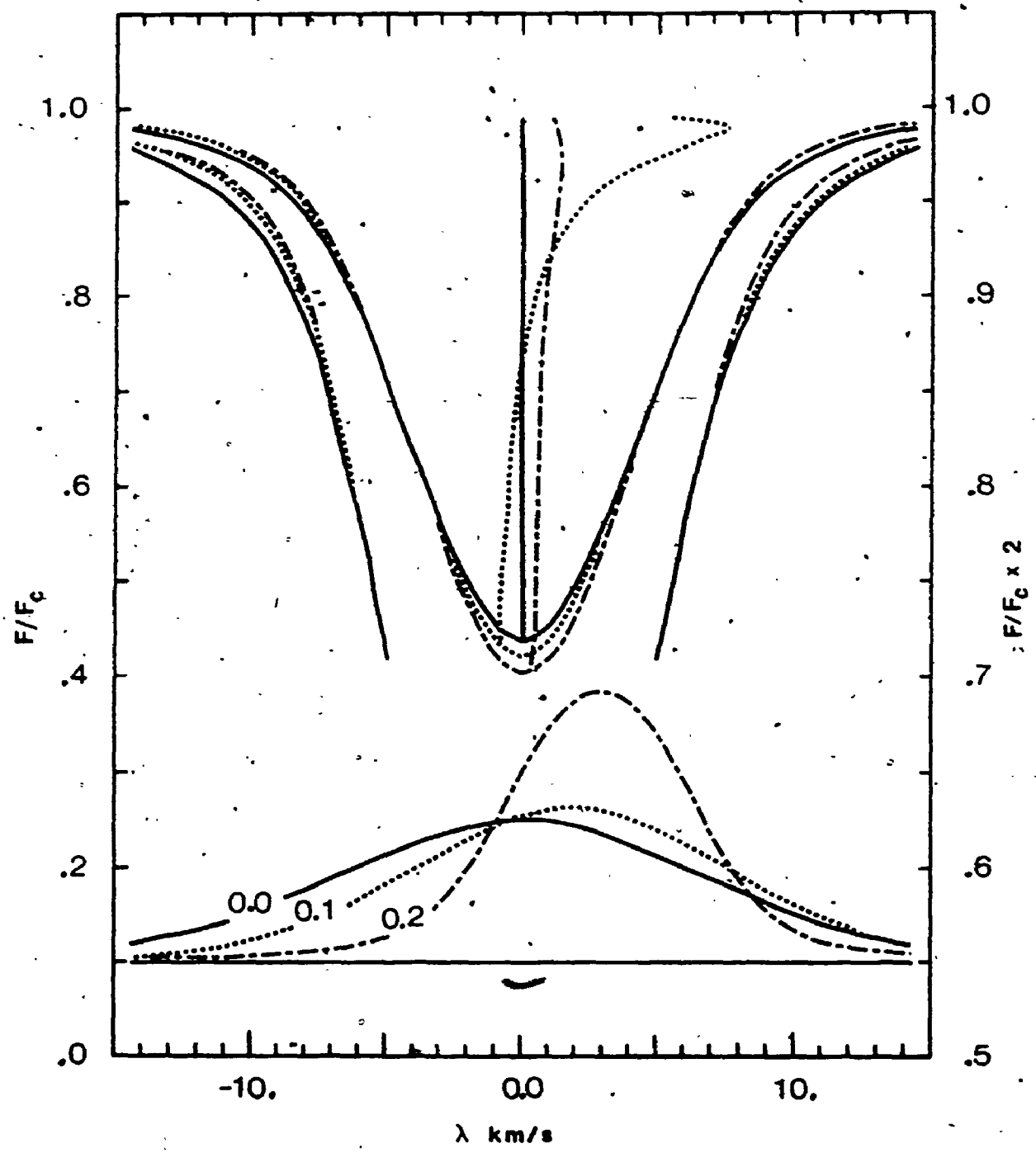

Figure B.2 The profiles and bisectors for three representative phases (0.0, 0.1, and 0.2), going from disk center to the receeding limb, are shown. The line wings have also been plotted on an expanded scale so that the changes can be seen more clearly. Below these are the velocity distributions at patch center.

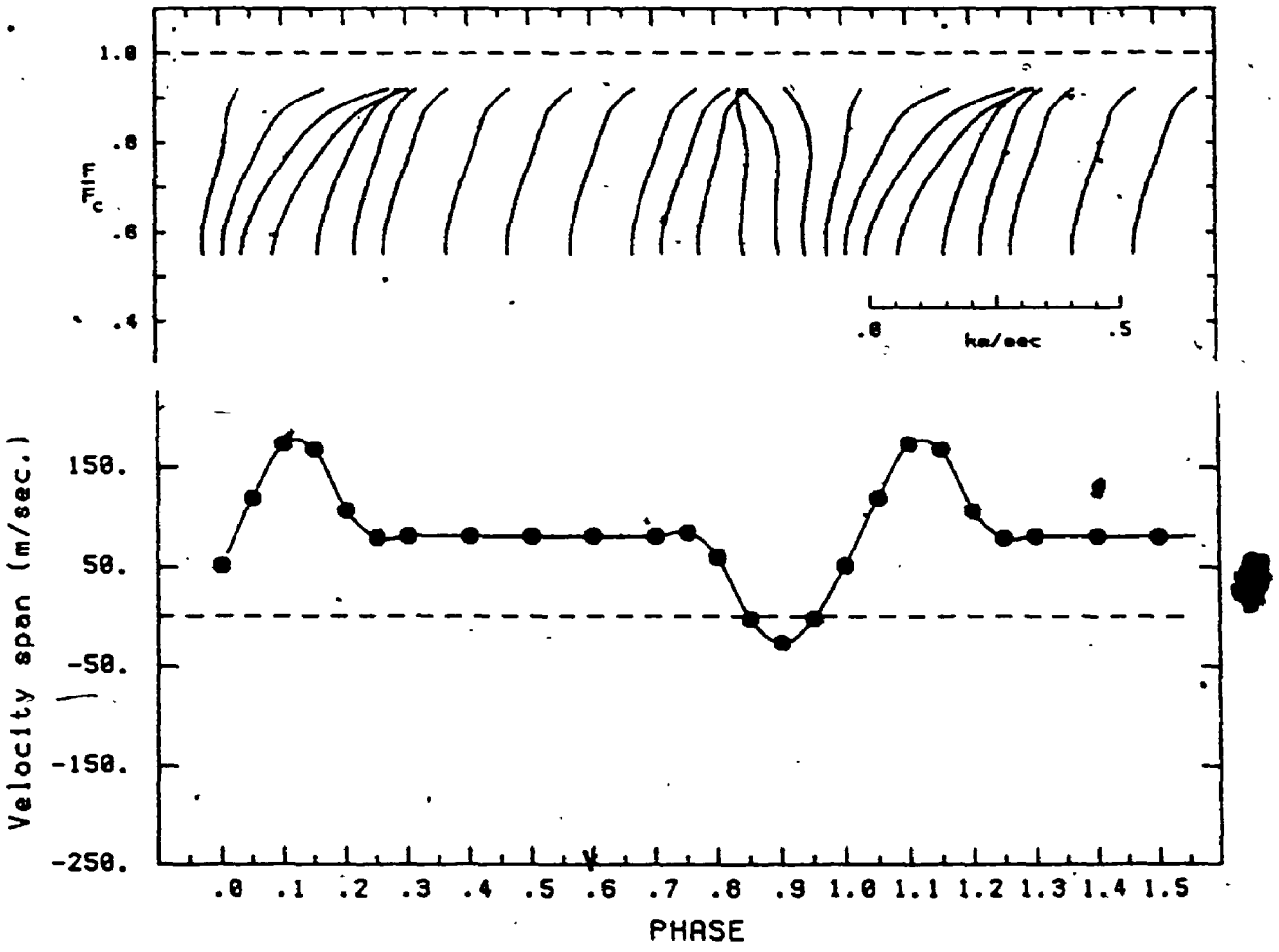

Figure B.3 Granulation is now introduced (ω_h = -1.5, ω_c = 4.5, and F_c/F_h = 0.10). The bisector shape changes (top) look much more complicated, but the velocity spans (bottom) have simply been shifted vertically.

REFERENCES

Babcock, H.W., and Babcock, H.D., 1955, Ap. J., 121, 349.

Baliunas, S.L., and Vaughan, A.H., 1985, Ann. Rev. Astron. Ap., 23, 379.

Baliunas, S.L., Hartmann, L.W., Vaughan, A.H., Liller, W., and Dupree, A.K., 1981, Ap. J., 246, 473.

Baliunas, S.L., Vaughan, A.H., Hartmann, L., Middelkoop, F., Mihalas, D., Noyes, R.W., Preston, G.W., Frazer, J., and Lanning, H., 1983, Ap. J., 275, 752.

Baliunas, S.L., Horne, J.H., Porter, A., Duncan, D.K, Frazer, J., Lanning, H., Misch, A., Mueller, J., Noyes, R.W., Soyumer, D., Vaughan, A.H., and Woodard, L., 1985, Ap. J., 294, 310.

Beckers, J.M., 1969, Air Force Cambridge Research Laboratories, AFCRL-69-0115, Phys. Sciences Research Papers, No. 371.

Beckers, J.M., Bridges, C.A., and Gilliam, L.B., 1976, *A High Resolution Spectral Atlas of the Solar Irradiance from 380 to 700 Nanometers*, Air Force Geophysics Laboratory, Hanscom AFB, MA.

Boesgaard, A.M., 1974, Ap. J., 188, 567.

Bonsa, E.F., Edwards, G., and Mayer, M., 1984, Ap. J., 284, 211.

Brant, P.N., and Schröter, E.H., 1983, in *Small-Scale Dynamical Processes in Quiet Stellar Atmospheres*, Keil, S.L. ed., p. 371.

Brault, J.W. and White, O.R., 1971, Astr. Ap., 13, 169.

Brown, D.N., and Landstreet, J.D., 1981, Ap. J., 246, 899.

Cavallini, F., Ceppatelli, G., and Righini, A., 1983, in *Small-Scale Dynamical Processes in Quiet Stellar Atmospheres*, Keil, S.L. ed., p. 344.

Dravins, D., 1982, Ann. Rev. Astron. Ap., 20, 61.

Dravins, D., 1987a, Astr. Ap., 172, 200.

Dravins, D., 1987b, Astr. Ap., 172, 211.

Dravins, D., Lindegren, L., and Nordlund, A., 1981, Astr. Ap., 96, 345.

Eaton, J.A., and Hall, D.S., 1979, Ap. J., 227, 907.

Evans, D.S., 1959, M.N., 119, 526.

Evans, D.S., 1971, M.N., 154, 329.

Fekel, F.C., 1980, Bull. A.A.S., 12, 500.

Fekel, F.C., 1983, Ap. J., 268, 274.

Frazier, E.N., 1970, Solar Phys., 14, 89.

Freidemann, C., and Gurtler, J., 1975, Astron. Nachr., 296, 125.

Giampapa, M.S., Golub, L., and Worden, S.P., 1983, Ap. J. Lett., 268, L121.

Gondoin, Ph., Giampapa, M.S., and Bookbinder, J. A., 1985, Ap. J., 297, 710.

Gondoin, P., 1986, Astron. Ap., 160, 73.

Gray, D.F., 1967, Ap. J., 149, 317.

Gray, D.F., 1976, in *The Observation and Analysis of Stellar Photospheres*, Wiley and Sons, New York, p. 276.

Gray, D.F., 1980, Ap. J., 235, 508.

Gray, D.F., 1981, Ap. J., 251, 583.

Gray, D.F., 1982, Ap. J., 255, 200.

Gray, D.F., 1983, Pub. A.S.P., 95, 252.

Gray, D.F., 1984a, Ap. J., 277, 640.

Gray, D.F., 1984b, Ap. J., 281, 719.

Gray, D.F., 1986a, Pub. A.S.P., 98, 319.

Gray, D.F., and Toner, C.G., 1985, Pub. A.S.P., 97, 543.

Gray, D.F., and Toner, C.G., 1986, Pub. A.S.P., 98, 499.

Hill, G., 1982, Pub. D.A.O., Vol. XVI, No. 6.

Jerzykiewicz, M., Serkowski, K , 1966, Lowell Obs. Bull., 6, 1295.

Kaisig, M. and Schröter, E.H., 1983, Ast. Ap., 117, 305.

Kaisig, M., Durrant, C.J., and Schröter, E.H., 1983, in *Small-Scale Dynamical Processes in Quiet Stellar Atmospheres*, Keil, S.L. ed., p. 360.

Kron, G.E., 1947, Pub. A.S.P., 59, 261.

Kron, G.E., 1950, Astron. J., 55, 69.

Kron, G.E., 1952, Ap. J., 115, 301.

Livingston, W.C., 1982, Nature, 297, 208.

Livingston, W.C., 1983a, in *Solar and Magnetic Fields: Origins and Coronal Effects*, IAU Symp. No. 102, Stenflo, J.O. ed., 149.

Livingston, W.C., 1983b, in *Small-Scale Dynamical Processes in Quiet Stellar Atmospheres*, Keil, S.L. ed., p. 330.

Lockwood, G.W., Thompson, D.T., Radick, R.R., Osborn, W.H., Baggett, W.E., Duncan, D.K., and Hartmann, L.W., 1984, Pub. A.S.P., 96, 714.

Macris, C.J., 1979, Astr. Ap., 78, 186.

Macris, C.J., and Rösch, J., 1983, C.R. Seances Acad. Sci., Ser. II, Tome 296, No. 4, p. 265.265.

Macris, C.J., Muller, R., Rösch, J., and Roudier, T., 1983, in *Small-Scale Dynamical Processes in Quiet Stellar Atmospheres*, Keil, S.L. ed., p. 265.

Marcy, G.W., 1984, Ap. J., 281, 286.

Matthews, J.M., and Wehlau, W.H., 1985, Pub. A.S.P., 97, 841.

Moore, C.E., 1959, *NBS Bulletin 36, A Multiplet Table of Astrophysical Interest.*

Moore, C.E., Minnaert, E.A., and Houtgast, J., 1966, *The Solar Spectrum 2935 Å to 8770 Å*, U.S. Government Printing Office, Washington, D.C.

Noyes, R.W., Hartmann, L.W., Baliunas, S.L., Duncan, D.K., and Vaughan, A.H., 1984, Ap. J., 279, 763.

Oskanyan, V.S., Evans, D.S., Lacy, C., and McMillan, R.S., 1977, Ap. J., 214, 430.

Poe, C.H., and Eaton, J.A., 1985, Ap. J., 289, 644.

Radick, R.R., Hartmann, L., Mihalas, D., Worden, S.P., Africano, J.L., Klimke, A., and Tyson, E.T., 1982, Pub. A.S.P., 94, 934.

Radick, R.R., Wilkerson, M.S., Worden, S.P., Africano, J.L., Klimke, A., Ruden, S., Rogers, W., Armandroff, T.E., and Giampapa, M.S., 1983a, Pub. A.S.P., 95, 300.

Radick, R.R., Lockwood, G.W., Thompson, D.T., Warnock III, A., Hartmann, L.W., Mihalas, D., Worden, S.P., Henry, G.W., and Sherlin, J.M., 1983b, Pub. A.S.P., 95, 621.

Ramsey, L.W., and Nations, H.L., 1980, Ap. J. Lett., 239, L121.

Richardson, E.H., 1968, R.A.S.C., 62, 313.

Richardson, E.H., 1972, Cont. D.A.O., No. 202.

Richardson, R.S., and Schwarzchild, M., 1950, Ap. J., 111, 351.

Robinson, R.D., 1980, Ap. J., 239, 961.

Robinson, R.D., Worden, S.P., and Harvey, J.W., 1980, Ap. J. Lett., 236, L155.

Rodonò, M., Cutispoto, G., Pazzani, V., Catalano, S., Byrne, P.B., Doyle, J.G., Butler, C.J., Andrews, A.D., Bianco, C., Marilli, E., Linsky, J.L., Scaltriti, F., Busso, M., Cellino, A., Hopkins, J.L., Okazaki, A., Hayashi, S.S., Zeilik, M., Helston, R., Henson, G., Smith, P., and Simon, T., 1986, Astron. Ap., 165, 135.

Saar, S.H., 1987a, Ph.D. Thesis, University of Colorado, Boulder.

Saar, S.H., 1987b, in *The Fifth Cambridge Workshop on Cool Stars, Stellar Systems, and The Sun*, Linsky, J.L. and Stencel, R.E eds., in press.

Saar, S.H., Linsky, J.L., and Beckers, J.M., 1986, Ap.J., 302, 777.

Saar, S.H., Huovelin, J., Giampapa, M.S., Linsky, J.L., and Jordan, C., 1987, in *The Midnight Workshop on Activity in Cool Star Envelopes*, (Reidel:Dordrecht-Holland), in press.

Scargle, J.D., 1982, Ap. J., 263, 835.

Schröter, E.H., 1962, Z. Astrophys., 56, 183.

Skumanich, A., Smythe, C., and Frazier, E.N., 1970, Ap. J., 200, 747.

Smith, M.A., 1979, Pub. A.S.P., 91, 737.

Soderblom, D.R., 1982, Ap. J., 263, 239.

Strand, K.Aa., 1938, Lieden Ann., 18, 97, 137.

Toner, C.G., 1984, M.Sc. Thesis, University of Western Ontario

Torres, C.A.O., and Ferraz-Mello, S., 1973, Astron. Ap., 27, 231.

Vaughan, A.H., 1980, Pub. A.S.P., 92, 392.

Vaughan, A.H., 1984, Science, 255, 793.

Vaughan, A.H. and Preston,, G.W., 1980, Pub. A.S.P., 92, 385.

Vaughan, A.H., Baliunas, S.L., Middelkoop, F., Hartmann, L.W., Mihalas, D., Noyes, R.W., and Preston, G.W., 1981, Ap. J., 250, 276.

Vogt, S.S., 1979, Pub. A.S.P., 91, 616.

Vogt, S.S., 1980, Ap. J., 240, 567.

Vogt, S.S., 1981a, Ap. J., 247, 975.

Vogt, S.S., 1981b, Ap. J., 250, 327.

Vogt, S.S. and Penrod, G.D., 1983, Pub. A.S.P., 95, 565.

Vogt, S.S., Tull, R.G., and Kelton, P., 1978, Applied Optics, 17, 574.

Vogt, S.S., Penrod, G.D., and Hatzes, A.P., 1987, Ap. J., 321, 496.

White, O.R., and Livingston, W.C., 1981, Ap. J., 249, 798.

Wielen, R., 1962, Astr. J., 67, 599.

Wilson, O.C., 1978, Ap. J., 226, 379.